Microchannel enhanced neuron-computer interface: design, fabrication, biophysics of signal generation, signal strength optimization, and its applications to ion-channel screening and basic neuroscience research.

Ling Wang

Supervised by Dr. Enric Claverol Tinturé

The Institute for Bioengineering of Catalonia

Biomedical Engineering Program, Departament d'Enginyeria de Sistemes, Automàtica i Informàtica Industrial (ESAII)

Universitat Politècnica de Catalunya

A thesis submitted for the degree of

Doctor of Philosophy

09/2011

I dedicate this thesis to my precious wife Luo Xiao, who is always my pillar, my joy and my guiding light... This thesis is also dedicated to my parents, Wang Dong Cai and Wu Man Ling, who have been constant sources of support – emotional, moral and financial, during all these years.

Acknowledgements

It is with immense gratitude that I acknowledge the support and help of my supervisor Dr. Enric Claverol Tinturé, whose kindness and academic experience have been invaluable to me. I am extremely grateful to Prof. Ramón Alcubilla González (Department of Electronic Engineering, UPC) for allowing me to access his clean-room facility, to Prof. José Antonio del Río (Department of Cell Biology, UB) for sharing his knowledge in neuroscience, to Prof. Raimon Jané (ESAII, UPC) for inspiring me in signal processing, to Dr. Dobryna Zalvidea (IBEC) for sharing his knowledge in optics and microscopy, and to Francisco Miguel García Molina (Department of Electronic Engineering, UPC), Gema López Rodríguez (Department of Electronic Engineering, UPC), Marina Cazorla Blázquez (Nanotechnology Platform, PCB), Raúl Pérez Rodríguez (Nanotechnology Platform, PCB) and other clean-room staffs for sharing their precious experience and knowledge in the microfabrication. I wish to thank our technician, Jennifer Olmos-Buitrago who helped us with animal dissection, cell culture and immunohistology. The collaboration of Mr. Juan C. Diaz in pharmacological experiments has been extremely helpful. The assistance of Dr. Isabel Oliveira, Laura Gómez and other staffs of the Institute for Bioengineering of Catalonia has also been most helpful. The discussion and encouragement of many friends has been indispensable, and I would like particularly to acknowledge the contribution of Michael Riss, Oscar Seira, Dr. Oscar Castaño, Ricardo Morales, and Vito Di Virgilio.

It also gives me great pleasure in acknowledging the financial support from the AGAUR/Generalitat de Catalunya and EU project NMP4-CT-2006-031971.

Abstract

In this dissertation, we demonstrate the use of microchannels as a low-cost neuron-electrode interface to support low-complexity, long-term-stable, high signal-to-noise ratio (SNR) extracellular recording of neural activity, with high-throughput potential. The biophysics of the signal generation of microchannel devices was studied by experiments and numerical simulations. Based on the results, we demonstrate and rationalize how channels with a length of ≤ 200 μm and channel cross section of ≤ 12 μm^2 yield spike sizes in the millivolt range. Despite the low degree of complexity involved in their fabrication and use, microchannel devices provide a single-unit mean SNR of 101 ± 76, which compares favourably with the SNR obtained from recent developments employing CNT-coated electrodes and Si-NWFETs. We further demonstrate that the microchannel can be used as a promising technique for high-throughput automatic ion channel screening at subcellular level. Finally, a microwell-microchannel enhanced multi-electrode array allowing high-SNR, multi-site recording from the low-density hippocampal neural network in vitro was designed, fabricated and tested.

Contents

List of Figures

LIST OF FIGURES

List of Tables

LIST OF TABLES

Nomenclature

Roman Symbols

$[L]$ The free ligand concentration, i.e. the concentration of the blockade, page 54

$\bar{g}_i$ Maximal conductance density of the voltage-dependent ion channels, i can be any kind of ion channels, page 32

$\bar{I}_{ex}$ the magnitude of the microchannel-confined extracellular current averaged along the channel, page 10

A_c The cross-section area, page 33

A_0 The geometrical cross-section area of a microchannel, page 68

$A_{\mu Chan}$ the cross-sectional area of the μChannel, page 31

A_E The effective cross-section area of a clogged microchannel, page 68

B Bandwidth in Hertz, page 17

$C(x,t)$ The concentration distribution, page 67

C_{4-AP} The concentration of 4-AP, page 70

D Diffusion coefficient, page 67

g_F The conductance density of fast delayed rectifier ion channels, page 54

g_K Conductance density of the voltage-dependent K^+ channels, page 32

g_L Conductance density of the leak ion channels, page 32

g_{Na} Conductance density of the voltage-dependent Na^+ channels, page 32

g_S The conductance density of slow delayed rectifier ion channels, page 54

I_chan intrachannel current, page 17

LIST OF TABLES

I_n RMS current-noise, page 17

I_{cm} The transmembrane current, page 78

K Botlzmann constant, page 17

K_F The fast delayed rectifier ion channels, page 81

K_S The slow delayed rectifier ion channels, page 81

K_A The blockade concentration blocking 50% of targeted ion channels, i.e. the IC50 value., page 54

K_d The apparent dissociation constant, page 54

L_c The length of a microchannel, page 26

L_{clog} The length of the clogged area in a microchannel, page 37

n The Hill coefficient, page 54

r radius of the neurite, page 10

R_a axial specific resistance, page 10

R_c Pearson's linear correlation coefficient, page 29

R_m specific membrane resistance, page 10

R_{chan} end-to-end resistance of the microchannel, page 10

R_{ch} The end-to-end resistance of the microchannel, page 17

R_{post} The end-to-end resistance of a microchannel with cell culture, page 28

R_{pre} The end-to-end resistance of a microchannel without cell culture, page 28

T Temperature, page 17

V_{ap} transient electrical potentials measured between two microchannel-connected culture wells, page 10

Greek Symbols

$\bar{\rho}_{clog}$ The increase in the overall resistivity of the μChannels at 10-14 days in vitro, page 33

$\bar{\rho}_{clog}(L_x)$ The measured average increase of the resistivity inside a microchannel; L_x is the microchannel length, page 37

$\bar{\rho}_{post}$ The average resistivity of a microchannel with cell culture, page 28

$\bar{\rho}_{pre}$ The average resistivity of a microchannel without cell culture, page 28

λ electrotonic length, page 10

$\rho_{clog}(x)$ The spatial distribution of the increase of the resistivity inside a microchannel, page 37

ρ_{ex} The extracellular resistivity, page 31

θ_i The fraction of unoccupied sites, i.e. functional ion channels; i can be any kind of ion channels, page 54

Acronyms

3,4-DAP 3,4-Diaminopyridine, page 50

4-AP 4-Aminopyridine, page 6

µChannel The microchannel, page 23

µM Micromolar, having a concentration of 10^{-6} mole per litre, page 14

µV microvolt, page 7

AH axon hillock, page 10

AP action potential, page 2

Ara-C Cytosine β-arabino furanoside, page 14

CC current-clamp, page 17

CNS central never system, page 2

CV Conduction velocity of an axon, page 75

D_{sc} The distance from the soma to the proximal entrance, page 59

distal entrance The microchannel entrance in distal-well, page 59

DIV Days in vitro, page 28

LIST OF TABLES

pA picoampere, page 2

PCE Phase cancelling effect, page 44

PDMS Polydimethylsiloxane, page 7

PECVD Plasma-enhanced chemical vapour deposition, page 9

pF pico Farad, page 17

PLL poly-L-lysine, page 14

proximal entrance The microchannel entrance in soma-well, page 59

RIE reactive-ion etching, page 109

RMS root mean square, page 3

SNR Signal to noise ratio, calculated by dividing maximum absolute peak value by RMS noise, page 3

V_{cm} Cross-membrane potential, page 61

V_{rec} Recorded signal waveform, page 78

VC voltage-clamp, page 17

LIST OF TABLES

Chapter 1 Introduction

Because the nerve system is responsible for controlling the animal body and motion planning, and is the origin of sensation, perception, cognition and emotion that the nerve system was, is and will be the one of the foci in biology attracting researches in many different fields (medical science, biology, mathematics, physics, engineering, computer science ...). In a nerve system, the neurons communicate with each other via synapses (electrical and chemical) to form a complex cell network, which can support learning, memory forming/extracting and pattern generation/recognition [1].

Due to the difference of permeability to different ions and the difference of ion concentrations between intracellular and extracellular solutions, there is a difference between the electrical potentials of intracellular and extracellular environment (cross-membrane potential) [1]. The permeability of neural membrane to different ions is controlled by a class of pore-forming transmembrane proteins (ion-channels).

The permeability of a fraction of ion-channels can be regulated by the cross-membrane potential, which can generate large transient positive cross-membrane potential peaks (action potential) while the cross-membrane potential excesses certain voltage threshold. This action potential will propagate to the axon terminals triggering or modulating the release of neural transmitters at synapses.

A fraction of ion-channels and receptors on neural membrane can be regulated by external stimulations (mechanical, chemical, temperature, optical, etc.) or by the neural transmitters leading to a local variation of cross-membrane potential in the neuron. This variation can then propagate through the entire membrane of the neuron and affect the action potential generation. The local variations of cross-membrane potential cause by different stimulations or different synapses can interact with each other, functioning as information processing or computing. **Hence it is believed that the variation of cross-membrane potential conveys the sensory information and is the most important indicator of neural information processing** [1]. Many diseases and

gene mutations can result in malfunction of ion-channels leading to abnormal regulation of the cross-membrane potentials, which is **one of the foci of drug screening** [2].

Hence, to **monitor or intervene the activity of neurons** at molecular level, small circuit level or even system level, **neuron-computer interfaces** are widely used in basic research [3–13] , drug discovery [14–19], neural prosthetics [20–26] and even environment toxin monitoring [27, 28].

There are 3×10^4-1×10^5 neurons and around 3×10^8 synapses per cubic millimetre in the mammalian central never system (CNS) [29, 30]. A neuron in CNS, usually containing a 5-30 μm diameter soma, 1-μm-diameter neurites, which have different roles in sensory signal processing, requires micrometer-scale monitoring technique to study. The action potential (AP) responsible for transuding information between neurons is usually as short as 1 millisecond (ms), require submillisecond time-resolution to monitoring them. Thus researchers are continuously labouring to develop neuron-computer interfaces to achieve **higher temporal, spatial resolution** and to record/stimulate **more neurons simultaneously**.

1.1 Electrical neuron-electrode interfaces

1.1.1 Conventional neuron-electrode interfaces

Conventionally, needle like electrodes (metal sharp electrodes or glass pipette filled with high conductible intro-electrode solution) are used to probe the membrane potential or extracellular potential. Specifically, because the patch-clamp method [31] can provide a submillivolt resolution for monitoring cross-membrane potential and pA resolution for recording transmembrane current, by accessing the neuron's internal space with relative low access resistance and significant low leakage conductance. It already becomes the golden method, since 1970s, to monitor electrical activity in vitro and in vivo. **However, patch-clamp is intrinsically low-throughput and technically complex** [2]. It involves careful manipulation, with submicrometer resolution, of one or more micropipettes to contact, seal and perforate the cellular membrane and achieve measurement and control of membrane potential. Alternatively, methods such as the loose-patch or cell-attach recording, which do not require to form gigaseal, were developed to speed up the manipulation speed, while the signal amplitudes are reduced from 50-100 mV range to 0.1-1 mV range.

1.1.2 Automated patch-clamp

To scale up the interfacing throughput without loosing the signal-to-noise ratio, some attempt to automate the patch-clamp procedure via robotic system [32–35]. At least one system, APATCHI-1TM [35] is already commercially available.

Others resort to develop lab-on-chip path-clamp devices by integrating microfluidic system and micro-orifice arrays in glass [36, 37], polymer [38, 39], silicon/SiO_2 [40, 41] and plastic/ SiO_2 [42] substrates. Suspended cells are drawn by a microflow or electric field towards micro-orifices where they seal, in a process analogous to the pipette-membrane seal of conventional electrophysiology.

For suspended cell lines, recently commercially available on-chip patch-clamp systems, such as, PatchXpress (Molecular Devices, Inc.), Ionworks population patch clamp (Molecular Devices, Inc.), and Qpatch (Sophion Bioscience, Inc.), can facilitate understanding mechanisms of the pathology of mutated ion-channels, and enables fast ion screening drug discovery. **But it is difficult to apply them to the neuronal culture or to a specific subcellular compartment of the neuron.**

1.1.3 Multi-Electrode Array (MEA)

To study the information process, synaptic plasticity and network formation of the small neuronal network, it requires to monitoring as many neurons as possible inside the network and as long as possible. It also requires the neurons to adhere to the substrate, develops functional neuron-to-neuron connections. The single electrode techniques such as patch clamp and intracellular recording are difficult to record more than 3-5 neurons. Due to the mechanical vibration and the wounds introduced by electrode-cell-membrane contact, they only allow recording from same neurons for a few hours. To overcome these disadvantages, MEA devices with an array of electrodes photolithographically fabricated were introduced in 1970s [43–45].

Because MEAs are capable of recording neural activity from multiple positions simultaneously for several weeks, there are emerging reports of using MEAs in basic neuroscience research, drug screening and toxicology. **Nevertheless, the typical SNR (maximum absolute peak value to RMS noise) is only 5-40** [46, 47]. To increase the SNR, many efforts are invested to provide better electrode materials [48–56] or micro-electrode shapes [57, 58].

Another disadvantage of contemporary MEAs is very low ratio of distinguishable units to total number of neurons in the culture. Only on the order of 1%, of neurons are monitored at unclear sites on the MEA [47, 59]. It requires that the soma is located within ∼5-10 µm of a micro-electrode [60, 61] to generate recordable extracellular signals. Moreover, the cells tend to migrate, leading to unstable electrode-neuron interfacing [62].

Some researchers try to increase electrode density, bringing the spatial resolution to subcellular scale [63, 64]. Hence, a neuron can generate recordable signals whereas the soma is located. Others resort to physically or chemically anchor neurons onto electrodes [47, 65–74]. However, these straightforward methods either **suffer from high fabrication costs and complexity or fail to maintain long-term electrode-cell coupling due to strong mobility of cells**.

1.2 Non-electrical interfaces

All the electrical interfacing techniques at cellular/subcellular level require certain kind of direct electrical connection to target neurons. It is difficult to form long-term interfacing due to mechanic motion of electrodes, glia proliferation around electrodes, the turning/growth of neurites, and the migration of somata. Therefore, there are emerging trends to develop non-electrical interfacing techniques such as magnetic resonance imaging (MRI) and optical imaging.

Recent developed new generation of **calcium-sensitive MRI contrast agents** [75] and **magnetic resonance microscopic techniques** [76, 77] bring the MRI spatial resolution to amazing 20-40 µm [76], which already allowing identifying single cells and temporal resolution to around 100 ms. **However, it is still a big challenge to reach millisecond requirement for identifying the single AP.**

Fluorescence-based optical imaging of neural activities usually have subcellular spatial resolutions [78–83]. Most of the reports are based on **calcium imaging** whose signal is an indirect indicator of neural activity, the calcium release/influx induced by the depolarization of the cell membrane. Single AP monitoring is difficult for this technique. The **voltage-sensitive dyes** [84, 85] or **voltage-sensitive fluorescent proteins** [82, 83, 86, 87] can directly monitor the membrane potential. However, due to reactive oxygen species and oxidization of dyes generated in fluorescence emission,

fluorescence based methods usually **suffered from photobleaching and phototoxicity** [88–90], although they have been dramatically reduced after 20 years efforts. This limits the monitoring time. The temporal resolution is usually 100-1000 ms depends on the imaging technique and the number of monitored neurons. **High temporal resolution remains challenging.**

To avoid the **photobleaching**, others start to search **non-fluorescence based** techniques, such as scattering/birefringence [91, 92] and second-harmonic [93, 94] signal detection. **Nevertheless, the signal generation mechanism remains unknown; and the extremely small signal magnitude usually requires averaging over time to obtain reasonable SNR.**

1.3 Dissertation Overview

To further **increase the SNR** of high-throughput neuron-computer interfaces, **increase the chronic robustness**, **reduce the fabrication costs**, and **reduce the human intervention during usage**, in this dissertation we used microfabrication techniques, numerical simulations, electrophysiological experiments to explore the feasibility of enhancing neuron-computer interfaces with microchannels and the biophysics of the signal generation in microchannel devices.

In chapter 2, we introduced to use microchannels integrated in polymer or plastic substrate as a **low-cost and scalable** neuron-electrode interface to support low-complexity multi-unit loose-patch recording and stimulation of developing networks with high-throughput potential. In these devices, micrometer-sized channels serve as substrate-embedded recording pipettes. Somata are plated and retained in the culture wells. Due to geometrical constraints while neural processes grow along the microchannels, a loose-patch configuration without human intervention can be effectively established.

To optimize the signal amplitudes, we further studied the biophysics of the signal generation of microchannel devices by experiments and numerical simulations. Chapter 3 discusses the impact of microchannel geometry on the signal amplitude, SNR and waveform shape. Based on these results, **the optimal microchannel geometry providing a mean SNR of 101±76** (chapter 3) was proposed.

Chapter 4 discusses the biology criteria of the neuron such as ion-channel distribution, ion-channel types and axon diameters on the signal amplitude, SNR and waveform shape. The hypothesis of **origin of the recorded signal** were proposed (chapter 4) based on these results.

To demonstrate the advantages of microchannel devices, two applications were proposed and tested:

(1) **Ion channel screening at subcellular level**. In chapter 4, we discuss the mass transfer of chemical compounds in microchannels and the effects of 4-Aminopyridine (4-AP) applied to different culture compartments on recorded signals.

(2) **An enhancer of the MEA for study of neuronal networks with the maximum SNR of 142, and a high ratio (61%) of distinguishable units to total number of neurons in the culture**. In chapter 5 a design of MEAs enhanced with embedded microchannels were proposed based on the biophysics of signal generation of microchannels. Chapter 6 describes the fabrication process and field tests with the hippocampal neuronal culture. We demonstrate that this microwell-microchannel enhanced MEA is a promising tool for the study of low-density neuronal networks.

Chapter 2 PDMS-on-polystyrene microchannel devices as integrated extracellular electrophysiology platform

2.1 Abstract

The electrophysiological characterization of cultured neurons is of paramount importance for drug discovery, safety pharmacology and basic research in the neurosciences. Technologies offering low cost, low technical complexity and potential for scalability towards high-throughput electrophysiology on in vitro neurons would be advantageous, in particular for screening purposes.

Here we describe a plastic culture substrate supporting low-complexity multi-unit loose-patch recording and stimulation of developing networks while retaining manufacturability compatible with low-cost and large-scale production. Our hybrid PDMS-on-polystyrene structures include culture wells (6 mm in diameter) and microchannels (25 µm × 3.7 µm × 1 mm) serving as substrate-embedded recording pipettes. Somas are plated and retained in the culture wells due to geometrical constraints while their processes grow along the microchannels, effectively establishing a loose-patch configuration without human intervention.

We demonstrate that off-the-shelf voltage-clamp, current-clamp and extracellular amplifiers can be used to record and stimulate neural activity with the aid of our dishes. Spikes up to 50 pA in voltage-clamp and 300 µV in current-clamp modes are recorded in sparse and bursting activity patterns characteristic of 1 week-old hippocampal cultures. Overall, this work suggests a strategy to endow conventional culture plastic ware with added functionality to enable cost-efficient network electrophysiology.

2.2 Introduction

As we mentioned in the previous chapter, conventional technology such as patch-clamp, loose patch, and single electrode intracellular recording, always require labouring human intervention, with submicrometer resolution, of one or more micropipettes to

contact, seal and perforate the cellular membrane and achieve measurement and control of membrane potential. Integrated lab-on-a-chip patch-clamp devices have recently been developed [36–42] towards high-throughput electrophysiology. However, for the proper function of existing lab-on-a-chip patch-clamp is the use of cells in suspension, detached from any substrates.

MEA an array of micron-scale electrodes fabricated on glass or silicon substrate was introduced to overcome this disadvantage and is capable of recording from multiple sites in one culture simultaneously. Conventional membrane voltage-clamp is, however, not possible with existing MEAs because stimulation relies on capacitively coupled short-lasting transients, rather than steady-state membrane charging as realized with the intracellular access afforded by conventional patch-clamp.

Nevertheless, the compatibility with fully developed networks offsets these limitations in applications requiring measurements on cultured neurons and networks. MEAs are used for studies on neurotoxicity [95], stem cell differentiation [96, 97], network computation [98, 99] and drug screening [100, 101]amongst other applications.

Ongoing research on MEAs aims at increasing the number of available electrodes, typically limited to about 100 in passive devices, by means of integrated electronics for on-wafer multiplexing and amplification [102]. Further work addresses the patterning of 2D cultures on MEAs by chemical means [98] and laser patterning of polymeric structures [69] as well as the coupling of MEAs and scaffolds to support 3D cultures [103] and the development of stand-alone portable systems [104].

Overall, although MEAs are well suited for electrophysiological studies on in vitro networks, they remain a rara avis in the average neuroscience lab, used only in about 0.4% of the neuroscience papers involving cell culture (source PubMed). Such limited impact in the neurosciences can be partly explained by the cost of MEA technology, with market prices in the range of 50-250 euros/device, compared to plastic culture consumables available at 0.50 euros/dish and inexpensive glass coverslips [105]. Moreover, a future reduction of MEA production costs appears problematic given the multi-mask clean-room photolithography procedures involved and the large substrate surface (up to 10 cm^2) used per device. Adding to cost considerations, a further deterrent against migration from standard dishes to MEAs is the still poorly known impact on the cultures of the switch from polystyrene substrates or glass coverslips, for which most protocols

have been established, to MEA surfaces with polyimide, PECVD SiO_2 or Si_3N_4 as insulators.

Here we describe a consumable plastic (PDMS-on-polystyrene, Figure 2.1 (a)) dish technology with low-cost per well that supports multi-unit recording of extracellular currents and potentials from adherent and anatomically complex neurons. Our devices are compatible with conventional electrophysiology instrumentation, including voltage-clamp, current-clamp and extracellular amplifiers and cultures are performed using standard dissociation and plating protocols growing on well-characterised polystyrene surfaces to establish functional networks.

Our approach involves integrating microchannel structures of appropriate geometries with culture dishes. The resulting confinement of neurites and their extracellular currents leads to electrical potentials recordable in large isopotential culture wells by means of low-cost and reusable macroelectrodes avoiding the need for microfabrication and substrate integration of micrometer-sized electrodes. This strategy enables routine functional inspection of the cultures and can potentially enable systematic large scale compound screening at low cost and technical complexity.

2.2.1 Rationale of the device

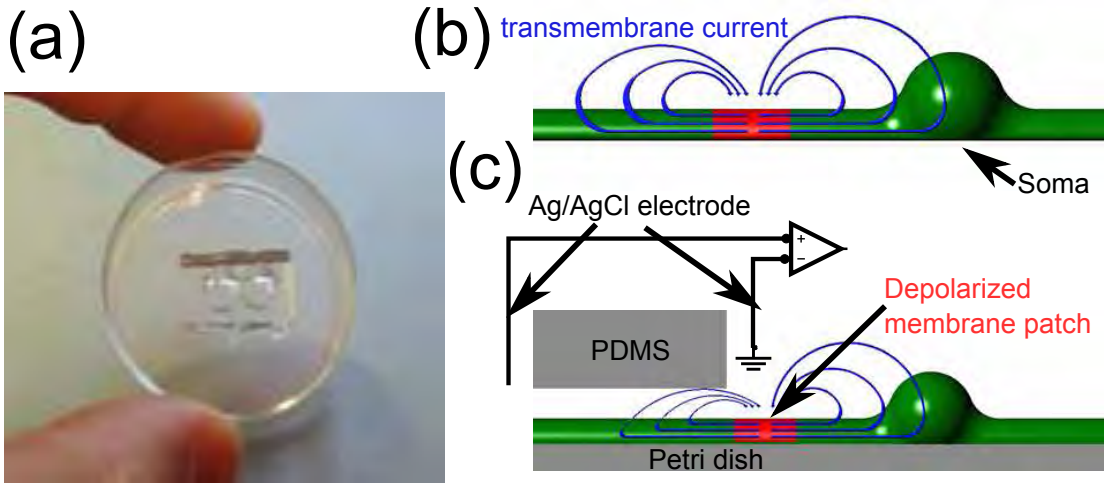

Figure 2.1. Rationale of the microchannel device (adapted from [106]). (a) 35 mm polystyrene dish with overlaid chamber-channel-chamber structure. (b-c) Cartoon sketch of transmembrane currents of a depolarized membrane patch in unconfined (b) and channel-confined neurons (c).

2. PDMS-ON-POLYSTYRENE MICROCHANNEL DEVICES AS INTEGRATED EXTRACELLULAR ELECTROPHYSIOLOGY PLATFORM

Action potentials (APs) involve $>$ 60 mV membrane depolarization and subsequent hyperpolarization at millisecond time scales by transiently sinking/sourcing Na^+/K^+ ions at the axon hillock (AH). The associated short-lived current loops (see blue arrows in Figure 2.1 (b)) extend in passive neurites as far as the electrotonic length [107], λ, ($\lambda = \sqrt{rR_m/(2R_a)}$), where R_m is the specific membrane resistance of the neurite ($\sim$50 K$\Omega\cdot$cm^2 for pyramidal cells[107]), R_a the axial specific resistance ($\sim$200 $\Omega\cdot$cm) and r its radius ($\sim$1 µm), resulting in λ = 1.12 mm. In practise regeneration of the APs by voltage-dependent Na^+/K^+ channels beyond the AH (e.g. at Ranvier nodes) can support longer range AP propagation and so λ is often taken as a lower bound for current spread distance. If the extracellular segments of the current loops are confined, for example with manually-positioned large-bore micropipettes in a loose-patch configuration [107], recordable potentials ensue.

Because hippocampus neurons extend neurites reaching up to several millimetres when cultured on appropriate substrates, i.e. coated with adhesion and growth promoters, we reasoned that confinement could be effected without human intervention due to spontaneous sprouting of neuronal processes within microchannels (Figure 2.1 (c)). The extracellular branch of the current results then in extracellularly recordable potentials associated with APs.

Indeed, preliminary data using invertebrate neurons showed that intrachannel potentials could be recorded with substrate-embedded micrometer-sized ITO [108] electrodes, akin to those used in conventional MEAs. We further anticipated that APs by confined axons would result in transient electrical potentials (V_{ap}) measured between two microchannel-connected culture wells and recordable by millimetre-sized Ag/AgCl macroelectrodes, avoiding altogether the need for substrate-embedded microelectrodes. The expected voltage V_{ap} is estimated as$\bar{I}_{ex} \times R_{chan}$ where $\bar{I}_{ex}$ is the magnitude of the microchannel-confined extracellular current averaged along the channel and R_{chan} its end-to-end resistance. Assuming $\bar{I}_{ex}$ and R_{chan} in the order of picoamperes and MΩ respectively, V_{ap} would reach values of microvolts.

We show here that channels with a cross-section of 25 µm $\times$ 3.7 µm support sprouting of axons (radius $\sim$1 µm), retain somas outside the channels and produce a resistance path of R_{chan} =10-20 MΩ (1 mm-long channel) sufficient to produce recordable signals. The needed well-channel-well structure can be realized with soft-lithography, resulting in low-cost all-plastic culture dishes that support low-complexity electrophysiology

on adherent, as opposite to suspended, neurons. We demonstrate that conventional voltage-clamp and current-clamp amplifiers in addition to extracellular low-noise instrumentation can be used for this purpose.

2.3 Methods and results

2.3.1 Device fabrication

A soft lithography master was produced by spinning SU-8 2005 (Microchem) at 3.7 µm on a 2 mm-thick Pyrex substrate. A 25 µm × 10 mm strip was photolithographically defined as the negative of the microchannel and a 7 mm-thick slab of PDMS was cured on the master (Figure 2.2 (a), 2.2 (b)). Under microscope inspection two culture wells with a diameter of 6 mm were opened (Figure 2.2 (c)). The separation between the culture wells (and the length of the channel) was 1 mm. The PDMS structure was overlaid on a polystyrene substrate, either a commercial culture dish (Corning treated 35 mm) or a custom cut 2 mm-thick polystyrene plate (Figure 2.2 (d)). For recording and stimulation a plexiglass frame with two wire electrodes was fitted on the culture wells (Figure 2.2 (e)-(h)). To produce the Ag/AgCl electrodes, 4 cm segments of Ag wire (WPI, diameter 0.015 inches) were bleach-chlorided by soaking for 20 minutes in household bleach and thoroughly rinsed with Milli-Q water.

Characterisation of the master and PDMS replicas made use of a mechanical profiler (Dektak, Veeco) and Cambridge S-360 scanning electron microscope (Leica).

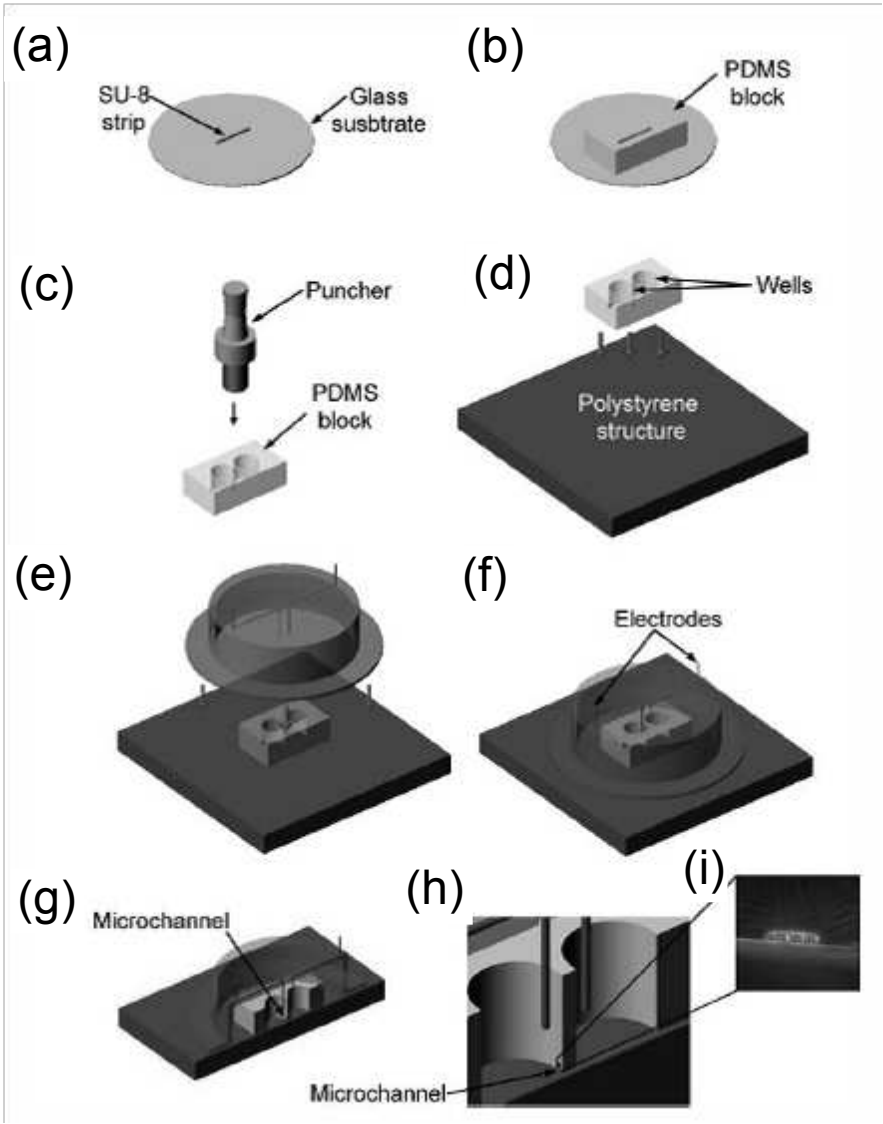

Figure 2.2. Fabrication steps (adapted from [106]). (a) An SU-8 master is produced by photolithographically defining a 3.7 μm × 25 μm × 10 mm strip on a circular Pyrex substrate. PDMS is cast on the master (b) and 6-mm wells are punched (c). The PDMS piece is overlaid on a polystyrene substrate d). A plexiglass structure including two Ag/AgCl macroelectrodes is lowered into the wells (e-f) to support recording and stimulation. (g-h) show the position of the macroelectrodes inside the wells with respect to the connecting microchannel. A SEM picture of the microchannel entrance is shown in (i) (scale bar 5 μm).

2.3.2 CO_2 priming of microchannels

Filling micrometer-sized microcavities and microchannels with aqueous solutions is possible using pressure or sequential rinsing with increasingly hydrated solvents such as ethanol + water. Yet widespread use of our devices would be facilitated if priming of the microchannels occurred spontaneously upon filling the culture wells with cell culture medium.

Despite treatment of the PDMS with oxygen plasma (Harrick), the resulting hydrophilic surface does not support consistent priming of the substrates. Moreover, plasma-induced hydrophilicity reverses with time, limiting shelf-life and likely introducing variability in filling performance.

Air micro bubbles in water can block the channel and hamper priming. They are stable long-term because the liquid in open air is at equilibrium and will not solubilize nitrogen, which makes up 80% of the micro bubble volume, beyond 20 mg/L. However, the atmospheric concentration of CO_2 is low, 385 ppm in volume, and its solubility in water is high at 1.45 g/L. Therefore a 100% CO_2 micro bubble in water will dissolve quickly due to the high solubility and low concentration of the gas in cell culture medium at equilibrium with atmosphere.

We superfused the device with CO_2 by placing it in a sealed container with gas inlet and outlet at a flow of 2 L/min for 2 minutes. The culture wells were filled with culture medium while inside the container to ensure entrapping of pure CO_2 inside the microchannels. Intrachannel CO_2 bubbles solubilize within seconds resulting in complete priming.

It was later discovered that it is also possible to fill the culture wells in air, and consistently achieve fully filled microchannels, with the condition that the operation is performed within 20 seconds of removing the device from the CO_2 container. Note that the diffusion time of nitrogen into the microchannel and the higher weight of CO_2 compared to air likely contributes to this result.

CO_2-enabled microchannel priming facilitates commercialisation because the devices are primed trivially by swift filling of the culture wells after opening gas-filled packaging and prior to culture. Moreover, shelf-life is not limited by the priming methodology.

2.3.3 Cell culture, neuronal transfection and microchannel-confined growth

Dissociated cultures of mouse hippocampus neurons were prepared as previously described [105]. Briefly, hippocampi were dissected from E18 embryonic mice, dissociated with papain (40 units/mL) at 37°C and gently triturated. Fresh cells were seeded at densities ranging from 10^4 to 10^5 neurons/culture well (3×10^2 neurons/mm^2 to 3.5×10^3 neurons/mm^2) in Neurobasal (NB) and supplemented with 2% B27, 2 mM L-glutamine, 5% horse serum (all from Invitrogen) and 20 µg/mL gentamycin (Sigma). Cytosine β-arabino furanoside (Ara-C) (Sigma) was added at 1 µM after 1 week to inhibit glial proliferation. 50% of the culture well volume was replaced with fresh culture medium weekly. Prior to cell plating and assembly of PDMS and polystyrene dishes, the substrates had been coated overnight with 0.01% poly-L-lysine (PLL).

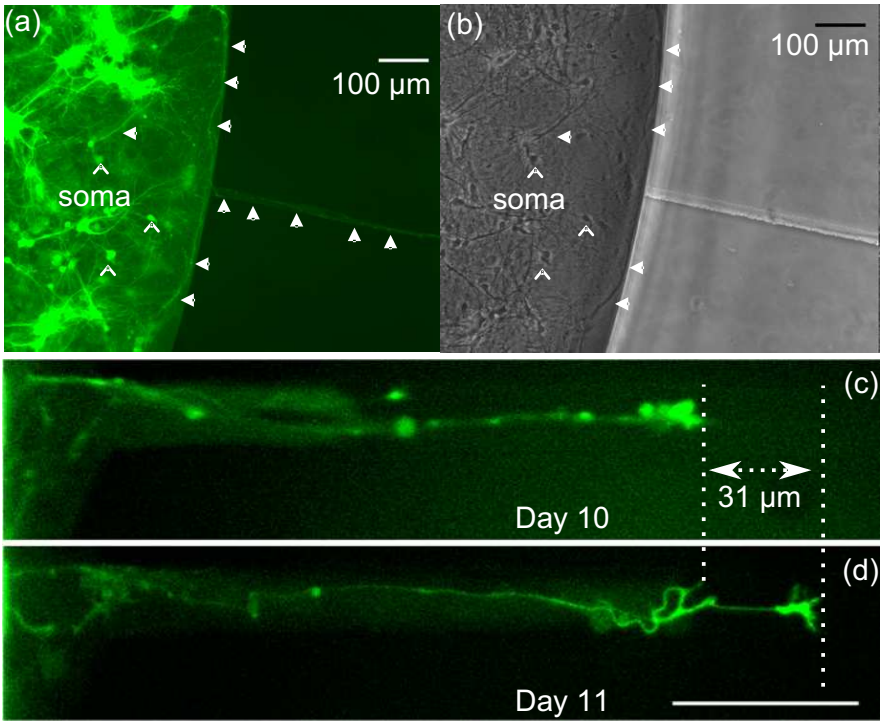

Figure 2.3. (a) Fluorescence and (b) phase contrast images of a GFP-transfected culture after 7 days in vitro illustrating sprouting within the microchannel. (c-d) show processes elongating in a microchannel from a different dish.

On occasions fresh hippocampus chunks (approximately 1 mm^3 in volume) were cryopreserved [109] with 10% Dimethyl sulfoxide (DMSO) as cryoprotectant in modified DMEM (Dulbecco's Modified Eagle Medium) supplemented with 100 µg/ml strepto-

mycin, 100 units/ml penicillin, 5% foetal calf serum, 5% horse serum and maintained in liquid nitrogen. Up to 6 months after freezing, cryopreserved tissue could be quickly thawed in a conventional water bath (2.5 mins), mechanically dissociated by gentle pipetting and plated at 4×10^4 to 10^5 neurons/culture well (1.4×10^3 neurons/mm^2 to 3.5×10^3 neurons/mm^2). Consistently with previous results [109], cell anatomy and activity patterns were similar in cultures of fresh and cryopreserved neurons.

To aid in visualising intrachannel outgrowth, selected cultures were transfected with Green-Fluorescence-Protein (GFP) using the lentivirus vector.

Lentiviral particles were produced by transient transfection of 293T cells with FuGENE6 (Roche) by use of the GFP-expressing vector pWPXL-GFP, the second-generation packaging construct psPAX2, and the envelope plasmid pMD2G. 293T cells were cultured in DMEM, supplemented with 10% foetal calf serum (FCS) and without antibiotics before transfection. Medium was changed and supplemented with antibiotics after 18 hours. Vector supernatants, containing viral particles, were harvested approximately 24 and 48 hours later and concentrated by ultracentrifugation (2 hours, 26000 g at 4°C).

After 4 days in vitro, the neuronal cultures were incubated at 33°C and 5% CO_2 with the lentivirus for 24 hours. The cultures were then rinsed with lentivirus-free medium and further incubated (37°C, 5% CO_2) until use. Fluorescence imaging made use of an inverted Nikon Eclipse TE200 microscope.

Figure 2.3 (a-b) show fluorescence and phase-contrast image, respectively, of a typical GFP-transfected culture after 7 days in vitro. Figure 2.3 (c-d) show elongation of processes within a microchannel from a different culture.

Figure 2.4 compares low versus high density cultures. Low density cultures resulted from plating densities of 10^4 fresh cells per well or, due to lower viability, 4×10^4 -10^5 cryopreserved cells per well. Low density cultures (figure 2.4 (a)) usually show sparse growth of processes along the microchannels whereas high density populations (10^5 fresh cells/well, Figure 2.4 (b)) often form bundles of processes threading the channels.

Recordings were attempted upon observation of axonal growth within the microchannel, typically 1 week after plating. For this purpose a patch-clamp (2400 AM-Systems) or a conventional extracellular (Multichannel Systems) amplifier were used.

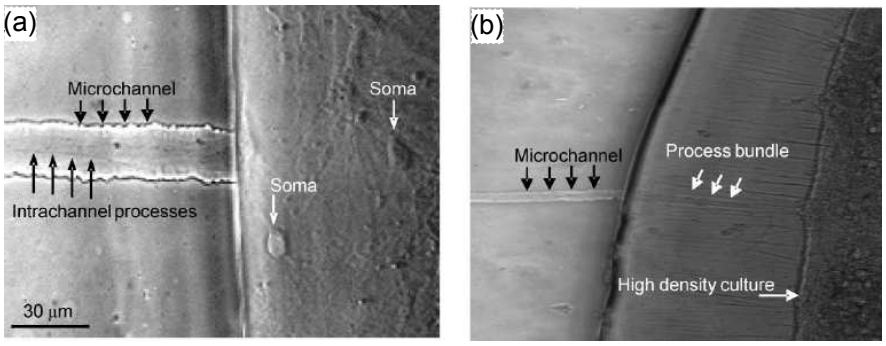

Figure 2.4. Culture of cryopreserved cells plated at 1.4×10^3 neurons/mm^2 (a) and fresh cells at 3.5×10^3 neurons/well (b) after 2 weeks in vitro showing multiple processes growing along the microchannel.

2.3.4 Extracellular spontaneous activity recorded with voltage-clamp amplifiers

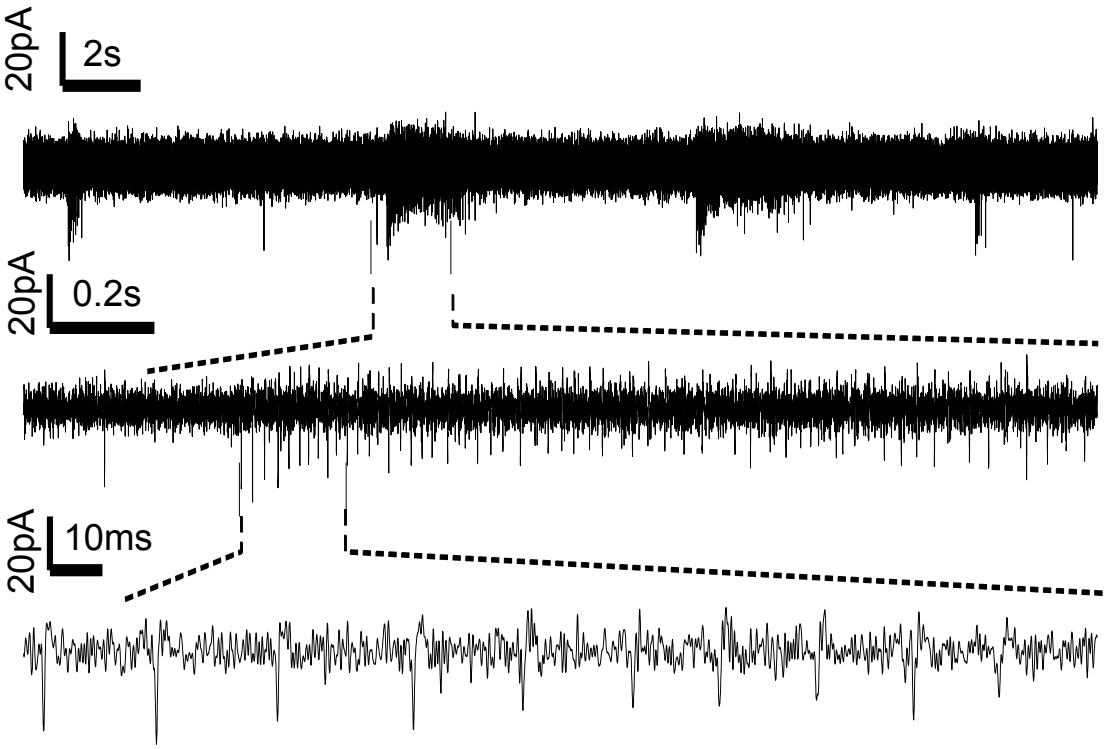

Figure 2.5. Raw data obtained in voltage-clamp mode with clamping voltage set to null offset currents. The traces contain typical hippocampal bursting activity (mean burst duration 2 s and inter-burst period 7.5 s) including single-unit spikes.

A voltage-clamp amplifier (2400 AM-Systems) was set up with sensing and ground Ag/AgCl electrodes in two microchannel-connected wells and the clamping-voltage was adjusted to null the channel current. Stray capacitance between the wells, measured at 15 pF, was compensated prior to obtaining the recordings. In this configuration transients of intrachannel current, I_chan, produced by confined neurons partly flow into the low-impedance input stage of the amplifier (see setup sketch in Figure 2.1 (c)) and are recorded as (extracellular) intrachannel current spikes.

Figure 2.5 shows activity recorded in voltage-clamp (VC) mode from the culture in Figure 2.4 (a), including bursts of negative-going single-unit spikes of up to 35 pA in amplitude and a duration of 450 µs (full-width half-height).

Note that the current-noise (I_n) in the recordings is dominated by the thermal noise of the microchannel: $I_n = \sqrt{4KBT/R_{ch}}$; where K is the Botlzmann constant, B the bandwidth, T the temperature and R_{ch} the end-to-end resistance of the channel. The measured noise in the recording is $I_n = 5.5$ pA_{rms} compared with the theoretically predicted thermal-noise of 4 pA_{rms}. Overall signal-to-noise ratio was 6.4 (AP peak to RMS noise).

The observed activity patterns obtained in VC mode are consistent with previous work showing that monolayer cultures of hippocampal neurons on conventional MEAs display spontaneous bursting activity [98].

2.3.5 Recordings with current-clamp and extracellular amplifiers

Conventional current-clamp (CC) and extracellular amplifiers use high impedance input stages, as opposite to low impedance in VC electronics, to measure intracellular and extracellular potentials. The former are usually employed for whole-cell recordings of intracellular potentials in the range 1-100 mV, and therefore noise levels of the order of hundreds of µV are acceptable whereas the latter aim at measuring much smaller signals (10 µV - 1 mV) and usually display proportionally lower noise levels.

Figure 2.6 shows bursting activity from different hippocampal cultures and demonstrates that both CC (figure 2.6 (a)) and extracellular (figure 2.6 (b)) amplifiers can be used with our dishes. Note, however, the superior signal-to-noise ratio of the latter (SNR = 13) versus CC (SNR = 6.5).

The possibility of recording activity with extracellular amplifiers but also with instrumentation designed for intracellular CC and VC measurements will facilitate adoption of our substrates by neuroscience labs. See movies M1 and M2 as supplementary information for real-time visualisation of sparse and bursting signals obtained with extracellular amplifiers.

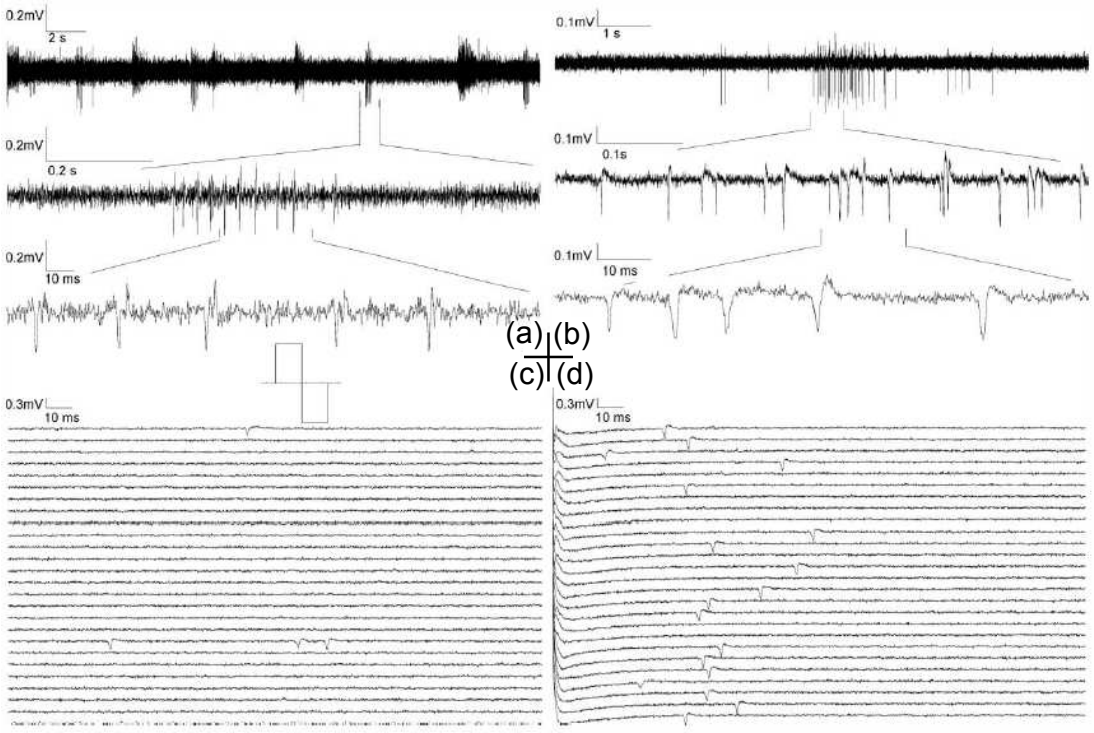

Figure 2.6. Spontaneous bursting activity recorded in current-clamp mode with conventional patch-clamp (a) and extracellular (b) amplifiers. (c) Baseline activity levels from a single microchannel (extracellular amplifier). (d) Stimulus-locked spikes evoked by ±30 nA biphasic pulses of 100 µs/phase (inset) applied to the microchannel in (c).

2.3.6 Stimulation

Beyond measuring spontaneous activity, we sought to demonstrate the suitability of our dishes to electrically probe the network. Figure 2.6 (c) shows 200 ms of extracellular recording prior to stimulation indicating that the baseline activity was sparse, averaging 46 spikes/minute. Biphasic voltage pulses (100-µs-long each phase, see inset in figure 2.5 (d)) were applied between the wells using a National Instruments DAC board under LabView control. We found that pulses of ±30 nA elicited the stimulation-locked response shown in figure 2.6 (d), increasing the effective mean spike rate to 204

spikes/minute or a factor of 4.4 with respect to baseline. Interestingly, the latency between stimulation (see left-most artefact) and the evoked activity averaged 63.4 ms suggesting that the response involved polysynaptic pathways.

2.4 Discussion

Dissociated neuronal cultures are ubiquitous in academia and industry as convenient preparations for pharmacological and electrophysiological studies. These are usually performed on O_2 plasma-treated polystyrene (PS) surfaces produced with plastic injection moulding and available at prices ranging from 0.50 euros for mono-well dishes to a few euros for a multi-well plate.

It is of broad interest to monitor spontaneous neuronal activity, electrically stimulated responses and their modulation by exogenous compounds in these cultures. Multi-electrode arrays (MEAs) provide this functionality and, yet, MEAs are used as culture substrates in only a small fraction of the publications employing monolayer preparations. Conventional pipette-enabled electrophysiology and calcium-sensitive optical probes are usually favoured and this is despite the technical complexity and low-throughput of pipette-electrophysiology and the moderate temporal resolution and staining issues associated with calcium imaging.

A possible explanation for the limited adoption of substrate-integrated electrophysiology is the cost of MEA dishes, which in 2007 ranged from 50 to 250 euros per well, more than two orders of magnitude higher than plastic consumables. A second deterrent against MEA adoption is the often encountered variability in cell anatomy and physiology introduced by changes in the type of surface used for culture, e.g. in switching from PS to glass-based electrical insulator-coated MEAs.

We set to develop a plastic dish that supports multi-unit extracellular electrophysiology while retaining convenient manufacturability, low cost per well and a standard PS surface.

Our approach relies on the spontaneous sprouting of neurites along microchannels serving as dish-embedded analogous of loose-patch pipettes. We first demonstrated that 3.7 μm × 25 μm PDMS microchannels overlaid on PS surfaces support normal outgrowth of processes from hippocampal neurons while excluding, due to size constraints, the

entry of somas. Processes form bundles after 1-2 weeks in vitro when seeding at densities of 10^5 cells/well but remain sparse at lower densities (Figure 2.4).

Note the similarity between the loose-patch (LP) [110] configuration and our devices. In LP a glass pipette forms a low-impedance seal (5-50 MΩ) around a membrane patch of ∼5 μm^2. Our microchannels, once threaded by axons, effectively provide a gap seal with a resistance of 10-20 MΩ distributed over a large membrane patch (axon length × perimeter = ∼6000 μm^2), separating the outgrowth into the distant well from the soma and local processes. It is to all effects a loose-(macro)patch configuration.

Hippocampal neurons from E18 embryos are spontaneously active in vitro[98] and we successfully attempted to measure this activity lowering Ag/AgCl macroelectrodes in microchannel-connected wells. Conventional current-clamp, voltage-clamp and extracellular amplifiers proved adequate to record sparse spikes and bursting activity, in accordance with previously described results with this type of cultures.

Stimulation was attempted using standard biphasic pulses and artefact-locked responses were obtained. This result suggests that stimulation-response studies as used for neurotoxicity tests [108] are possible with our dishes.

Production makes use of replica and injection moulding for the microchannels and PS substrate respectively, in addition to well punching. Therefore labour intensive clean room-bound tasks required for MEA fabrication [44] such as sputtering of conducting layers, spinning of photoresists, mask alignment/exposure, baking, development, etching, PECVD insulator deposition and electrode platinization can be avoided. The Ag/AgCl electrodes are easy to produce and reusable, and do not contribute to the cost per well. Overall, the functionality and plastic nature of our dishes suggest that they could replace conventional culture ware in the context of dissociated neuronal cultures.

2.5 Conclusions

We have demonstrated a plastic substrate for neuronal cultures which facilitates multi-unit recording and stimulation of extracellular potentials and currents. The suitability of our substrates for recordings on neurite-bearing neurons as opposed to non-adherent spherical cells renders them especially useful for studies on in vitro networks.

Since recordings are affected by reusable macroelectrodes that are lowered in and lifted from the wells as needed, the dish itself does not include metal parts and can be produced by a combination of replica/injection moulding and punching.

The convenient manufacturability, low-cost and microchannel priming of our devices make them a potential replacement for conventional culture dishes in the context of in vitro neuroscience.

2. PDMS-ON-POLYSTYRENE MICROCHANNEL DEVICES AS INTEGRATED EXTRACELLULAR ELECTROPHYSIOLOGY PLATFORM

Chapter 3 Biophysics of microchannel-enabled neuron-electrode interfaces

3.1 Abstract

We have previously described the use of microchannels (μChannels) as substrate-integrated equivalents of micropipettes and advantageous neuron-electrode interface enhancers. The use of μChannels to establish stable recording and stimulation of threading axons results in a high-SNR, potentially high-throughput and low-cost alternative to conventional substrate-embedded microelectrodes. Here we confirm the consistent achievement of high SNRs with μChannels and systematically characterise the impact of μChannel geometry on the measured signals via numerical simulations and in-vitro experiments. We demonstrate and rationalize how channels with a length of $\leq$ 200 μm and channel cross section of $\leq$ 12 μm^2 support spontaneous formation of seals and yield spike sizes in the millivolt range. Despite the low degree of complexity involved in their fabrication and use, μChannel devices provide a single-unit mean SNR of 101$\pm$76, which compares favourably with the SNR obtained from recent developments employing CNT-coated electrodes and Si-NWFETs.

3.2 Introduction

Neuron-electrode interfaces are promising tools against a wide range of neurological disorders in vivo [20, 21] and have demonstrated applicability to in vitro neuroscience research [7–15, 27, 28].

Multi-site electrical neural stimulation by means of macro (millimetre-sized) electrodes has been used to treat epilepsy [111, 112] and Parkinson's disease [24], proving to be of striking therapeutic value, whereas the higher spatial resolution afforded by micrometer-sized electrode arrays is best suited to functional stimulation of the retina [22, 23] and visual cortex [25, 26]. In addition to chronically robust electrical stimulation, intensive efforts have also been made to achieve interfaces capable of stable long-term recording of neural activity [113]. These could facilitate closed-loop stimulation [114],

enabling for example fine motor control of prosthetic limbs [21]. Microelectrode arrays (MEAs) capable of providing high spatial resolution without compromising time resolution, are among the most promising interfaces. Robotic arms can be precisely controlled via neural signals acquired by cortically implanted MEAs [115, 116]. The Utah array, an MEA with 3D needle electrodes, even allows the control of hand prostheses by a human subject [117].

Further, in vitro applications of MEAs are today well established in the fields of drug screening [14, 15], toxicology [27, 28] and basic network neuroscience research [7–9]. Recently, MEAs were used to study the learning, memory [10, 11] and pattern recognition [12, 13] of in vitro neuronal circuits.

Improving neuron-electrode coupling remains a challenging goal in the field. Notwithstanding application-specific requirements, a multipurpose optimal neuron-electrode interface would be characterised by: a high signal-to-noise ratio (SNR) in recording mode, high charge-transfer capacity for stimulation configurations and long-term mechanical and electrical stability of the neuron-electrode coupling, ideally with sustained access to individual cells.

To achieve low impedance, a high electrochemical-surface area to geometrical-surface area ratio (ESA/GSA) is often required [118]. Hence many proposals focus on coating electrodes with high-surface-area materials, such as platinum black [48], IrO_2, TiN, gold nanoparticles [49], gold flakes [50], nanoporous gold [51] or soft-conductive polymers [52]. Due to the exceptionally high ESA/GSA ($\sim$2.55 $F \cdot cm^{-2}$) of carbon/silicon nanotubes [53], nanotube coated electrodes [54] and nanowire-based field-effect transistors (NWFET) [55, 56] have recently been shown to provide excellent SNR. The use of 3D protruding microelectrodes [57] can also benefit SNR by providing close contact, e.g., in the case of acute measurements on slices, or may even aim to engulf the electrodes in the neuronal membrane for better coupling [58].

Despite improvements in SNR, most contemporary modifications to MEAs suffer from high fabricating costs and complexity. Biocompatibility studies also suggest that further studies are necessary to assess how nanotubes affect the neural activity via direct electrical coupling between neurons [119]. We previously described low-cost, easy-to-fabricate, microchannel-macroelectrode assemblies as an alternative to planar and protruding electrodes [106]. Neurites spontaneously sprouting into the polymeric microchannel (µChannel) cause an end-to-end potential difference during the action potential (AP);

in this way, the µChannels act like integrated electrophysiological pipettes in loose patch mode. Using 6-mm culture wells as widened µChannel ends allows for large (millimetre-sized) metal surfaces used as electrodes to record intrachannel neurite-related activity. An in vitro electrophysiology application of this principle (E2 technology, Aleria Biodevices) was released onto the market in 2009.

Because neurites usually grow up to several millimetres along the µChannel [106, 120], stable long-term access to individual cells is conceivably possible. Moreover, the use of large electrodes results in low electrode impedance (good charge-transfer characteristics) and controlling the µChannel geometry could potentially result in optimization of seal resistance and SNR. During depolarization at the axon hillock, the net membrane current flows inward; a fraction of this current, flowing along the axon and crossing the membrane, returns extracellularly back to the axon hillock. The returning current contained in the µChannel will cause an end-to-end potential difference (figure 3.2). According to Ohm's law, increasing the resistance of the µChannel (e.g., modifying its cross-section and length) would result in an increase of the potential difference.

Here, we report a quantitative study with hippocampal neurons and numerical simulations of compartmental models to assess the impact of µChannel cross section and length on signal magnitude, noise level and SNR. Optimized geometry can provide a good single-unit SNR of between 18±4 and 428±9, with a mean value 101±76. This value is already comparable to the maximum SNR obtained from CNT-coated electrodes (∼135 [54]) or from Si-NWFET (∼210 [55] and ∼120 [56], estimated from the figures), comparing to the typical SNR of traditional MEAs (5-40) [46, 47].

3.3 Methods

3.3.1 Device Fabrication

SU-8 layers spin coated onto glass substrates were photo-patterned in a mask aligner (MJB4, SUSS Microtec) under chrome masks to form SU-8 stripes of different widths. SU-8 layer thicknesses were controlled by spinning (Ws-650Sz Spin Coater): SU-8 2000.5 at 1000 rpm for 1 µm, SU-8 2002 at 3000 rpm for 2 µm and SU-8 2002 at 1000 rpm for 3.7 µm. Thicknesses and widths were then confirmed with an optical profiler (Wyko NT1100, Veeco) in vertical scanning interferometry (VSI) mode. A 5-mm-thick slab of PDMS was cured onto the master, peeled off and punched to form two culture wells (6 mm in diameter) as described previously [106]. The distances between the wells were controlled manually under a microscope.

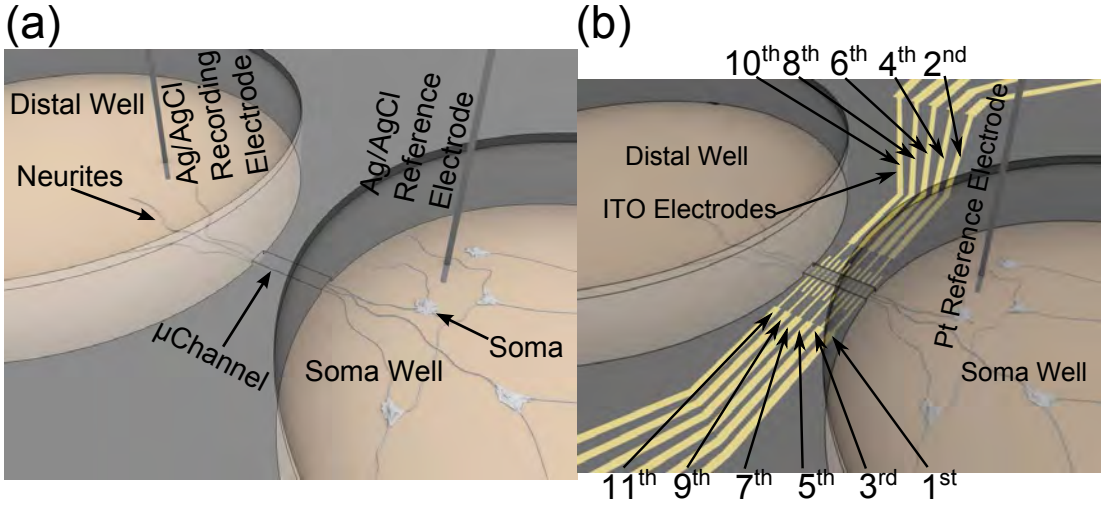

Figure 3.1. (a) Shows the device used in end-to-end recordings (N=110), with two chambers connected by a μChannel and an Ag/AgCl wire electrode (diameter 380 μm) per well. Neurons were plated only in one well (the soma well), whose electrode was used as reference. (b) Intrachannel recordings (N = 3) made use of a μChannel overlaid on an interdigitated MEA (ITO electrode width 40 μm with interelectrode spacing of 60 μm). In this case a Pt wire (diameter 250 μm) was placed in the soma well as the reference electrode.

Before culturing, μChannel devices were attached to polystyrene dishes (end-to-end experiments) or aligned to MEAs (intrachannel experiments) and primed with CO_2 [106]. Then the channel lengths (L_c) were measured using ImageJ software from phase contrast images of the devices.

MEA fabrication: A 100-nm-thick ITO layer on the glass substrate protected by a photo-patterned photoresist layer (SPR220-1.2) was etched at 50°C with mixed acids (HCl: 14.5%, HNO_3: 6.3%) to form 40-μm-wide electrodes with 60-μm separation. Before culturing, the MEA was cleaned using oxygen plasma for 15 mins in a PDC-002 plasma oven (Harrick Scientific) to enhance hydrophilicity.

3.3.2 Cell Culture

Dissociated cultures of mouse hippocampus neurons were prepared as described previously [106]. Briefly, E18 embryonic mice hippocampi blocks were dissected and cryopreserved in DMEM with 10% DMSO as cryoprotectant and with 100 mg/ml strepto-mycin, 100 units/ml penicillin and 10% horse serum as supplements (all from Invitrogen). After maintaining the tissue blocks in liquid nitrogen for up to 6 months, they were quickly thawed in a 37°C water bath, dissociated by gentle puffing and then plated at 5×10^4 cells/well ($\sim1.7\times10^3$ cells/mm^2) in Neurobasal supplemented by 2% B27, 1% Gluta-

mate, 10% horse serum and 20 µg/ml gentamicin (all from Invitrogen). Cells were only plated in one well (the soma well in figure 3.1) for each device. Then they were incubated in a 37°C, 5% CO_2, humidified environment for 12-14 days before recording; 50% of the medium by volume was exchanged twice a week with fresh medium.

3.3.3 Immunocytochemistry

Cells cultured on glass were fixed at room temperature for 30 mins with 4% formaldehyde + 4% sucrose in PBS, permeabilized with 0.1% Triton-X (Sigma; 23472-9) in PBS, and blocked with 1% goat serum (Invitrogen; PCN5000) in PBS for 1-2 hours. The cells were incubated in the primary antibodies overnight and then in the secondary antibodies for 6 hours. Following each incubation step, samples were washed with PBS for 6 hours to reduce non-specific labelling. The following primary antibodies were used: mouse anti-β-III isoform tubulin monoclonal (1:500; Millipore; MAB1637), rabbit anti-MAP2 polyclonal (1:500; Millipore; AB5622). As secondary antibodies, we used: anti-mouse-IgG conjugated Alexa Fluor 488 (Invitrogen; A21202) and anti-rabbit-IgG conjugated Alexa Fluor 555 (Invitrogen; A31572).

After mounting with Fluoramount (F4680 Sigma), the cells were imaged under a Leica SP1 confocal microscope, with excitation wavelengths of 488nm and 543nm, and emission filters: BP 500-548nm for Alexa 488 and BP 561-618nm for Alexa 555.

3.3.4 Electron Microscopy

Cells cultured on glass coverslips were fixed at 4°C for 90 mins with 2.5% Glutaraldehyde in PB, and washed in PB. After fixation the samples were dehydrated by the one-step method: after incubation in 1,1,1,3,3,3-hexamethyldisilazane (HDMS) for 5 mins, the samples were transferred into desiccators allowing the HDMS to evaporate for 25 mins. After complete evaporation of the HDMS, the samples were mounted, sputter-coated with a 60-nm gold layer and scanned in a Quanta 200 FEI, XTE 325/D8395 scanning electron microscope.

3.3.5 Resistance Measurements and Electrophysiology

The resistance of each µChannel filled with Neurobasal was measured using a patch clamp amplifier (A-M system, Inc.; Model 2400) in voltage-clamp mode (20 Hz square wave, 100 mV). Stray capacitance (10∼20 pF) between Ag/AgCl electrodes was compensated for before adding the culture medium. Two resistances were measured for each

μChannel: the resistance before cell plating (R_{pre}) and the resistance 12-14 DIV after cell plating (R_{post}). Then the resistivities ($\bar{\rho}_{pre}$, $\bar{\rho}_{post}$) were calculated from:

$$\bar{\rho} = \frac{R \times Area_{cross-section}}{Length_{\mu Channel}}$$

End-to-end Experiments: Immediately after the resistance measurement, electrophysiology recordings were conducted in a humidified incubator (37°C, 5% CO_2) with an Aleria 600A amplifier (Aleria Biodevices) at modified gain (×240) for at least 10 minutes per device. Reference electrodes were always placed in the soma well (figure 3.1). A pair of Ag/AgCl electrodes was used as recording and reference electrodes; the reference electrode was placed in the soma well (figure 3.1).

Intrachannel Experiments: at 14 DIV, recordings were performed in a dry incubator (37°C, 5% CO_2) with a multi-channel amplifier (Multichannel Systems, MEA1060-Inv-BC). MEA electrodes were recording from several sites within the μChannel, soma wells were grounded via a platinum wire.

3.3.6 Spike Detection and Sorting

After the raw signal was filtered with a 10-3000 Hz bandpass filter, spikes were detected via simple thresholding. We use a dynamically adjusted spike detection threshold [121], recalculated every 1 sec as $Threshold = Standard\,Deviation \times \sqrt{2 \times ln(N)}$, where N is the number of samples per second. Then spikes were clustered hierarchically using the squared Euclidean norm as the distance metric and average linkage clustering as the linkage criterion. The hierarchical cluster trees were manually cut to make sure clusters did not contain clearly different units in one group. Then manual group merging was conducted as described previously [106] to avoid redundant groups. All these procedures were performed with MATLAB.

3.3.7 Statistical Analysis

To analyze the impact of the channel geometry on the signal amplitude, the average height of the positive peaks was calculated for each unit to represent the amplitude. The amplitude of the largest unit of a μChannel was plotted against the geometry parameters (figure 3.6).

To characterize the noise level of a μChannel, the standard deviation of a randomly selected, 1-second-long continuous signal trace containing no spikes was calculated as the RMS noise.

SNR was calculated for each unit, via dividing the positive peak value by the RMS noise for the corresponding signal. To analyze the impact of the μChannel geometry on SNR, two populations of SNR values (M-SNR and L-SNR) were used:

- The L-SNR is the SNR of the largest unit from a μChannel.
- The M-SNR is the median SNR of all the units from the same μChannel, which provides a population view of the SNRs in that μChannel.

All values (SNRs, amplitudes and noises, etc.) were reported as 'Mean±Standard Deviation'.

All the correlation analyses, linear regressions, stepwise linear regressions and t-tests were conducted using the MATLAB Statistics Toolbox (Mathworks). The estimated coefficients were reported as 'Coefficient±Standard Error'.

To compare mean values from two groups with similar variance, Student's t-test was applied to the datasets. For datasets with different variances, we used the Welch-Satterthwaite t-test instead of Student's. For the datasets that did not have a normal distribution, we used the Mann-Whitney U-test to compare the median value instead of the mean value.

In linear correlation analyses, R_c represents Pearson's linear correlation coefficient. Corresponding p values reported together with R_c show how significantly R_c is different from zero. If $p < 0.05$, the correlation is considered as significant.

In linear regression, the robust regression algorithm with a bisquare weighting function was used to reduce the effect of outliers.

To study the relationship between multiple predictive terms and responses, natural logarithms are applied to both predictive terms and responses to convert the non-linear regression to the multiple-linear regression. A stepwise regression procedure was conducted to exclude redundant terms in the model [122].

3.3.8 Numerical Simulation

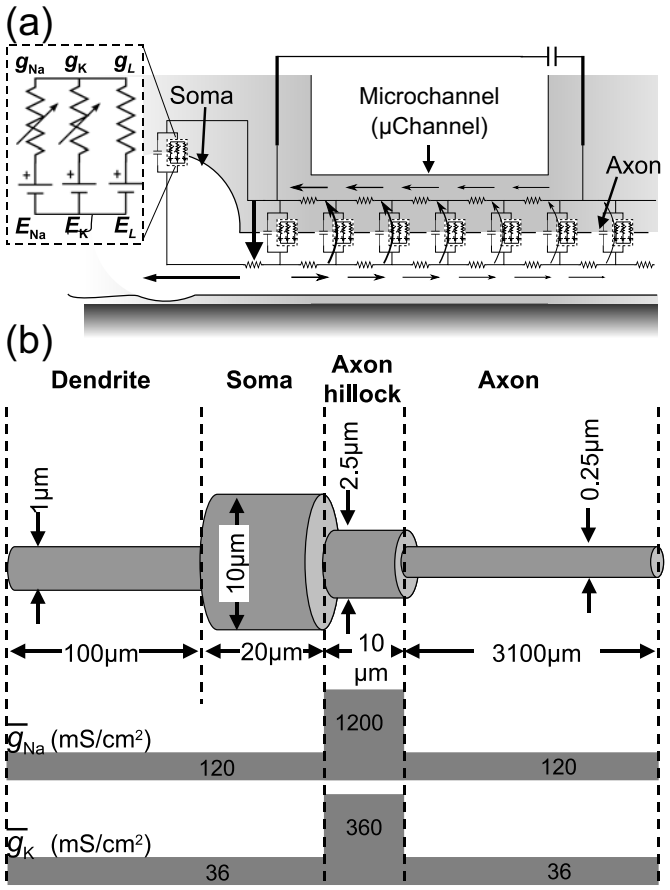

Figure 3.2. Detail of compartment model: (a) each membrane compartment includes 3 populations of ion channels: voltage-dependent sodium channel (g_{Na}), voltage-dependent potassium channel (g_K) and a leak channel (g_L). The intra-cellular medium and extra-cellular medium are modelled as axial resistances in series. During depolarization of the axon hillock, net current flows inwards at the axon hillock, caused by Na^+ channel opening. A fraction of this current (black arrows) flows along the axon, crosses the membrane and then returns back to the axon hillock through the μChannel. (b) The geometry of the neuron model and the spatial distribution of the voltage dependent sodium maximal conductance density $\bar{g}_{Na}$ and the voltage dependent potassium maximal conductance density $\bar{g}_K$.

Models were computed using MATLAB (Mathworks, version 2007b) running on Microsoft Windows-XP-SP2-64bit on a PC with a 2.5-GHz Intel$^{\mathrm{R}}$ Core$^{\mathrm{TM}}$2 Quad processor and 4 GB of RAM. The models were written in M script language.

Figure 3.2 illustrates the detail of our model. By default, a neuron model consists of a 100-μm-long dendrite with a diameter of 1 μm, a 20-μm-long soma with a diameter of

Table 3.1: Hodgkin - Huxley model parameters

Passive components	
Extracellular resistivity	$\rho_{ex} = \begin{cases} 2.55\Omega \cdot m;\ L_x \leq 200\mu m \\ 1.04\Omega \cdot m;\ L_x > 200\mu m \end{cases}$
Intracellular resistivity	$\rho_i = 0.7\Omega \cdot m$
Leak membrane conductance density	$g_L = 0.7S/m^2$
Membrane capacity	$C_m = 0.01F/m^2$
Leak Nernst potential	$E_L = -60mV$

Active components[a]	
Voltage-dependent Na^+ channel	$g_{Na} = \bar{g}_{Na} \cdot m^3 \cdot h$
Voltage-dependent K^+ channel	$g_K = \bar{g}_K \cdot n^4$
Na^+ Nernst potential	$E_{Na} = 60mV$
K^+ Nernst potential	$E_K = -90mV$

Kinetic parameters[a]	
For all parameters	$\frac{\mathrm{d}x(V,t)}{\mathrm{d}t} = (1 - x(V)) \cdot \alpha_x(V,t) - \beta_x(V,t);\quad x \in [m,\ h,\ n]$
m	$\alpha_m(V) = \frac{\frac{V+45}{10}}{1 - \exp(-\frac{V+45}{10})};\ \beta_m(V) = 4\exp(-\frac{V+70}{18})$
h	$\alpha_h(V) = 0.07\exp(-\frac{V+70}{20});\ \beta_h(V) = \frac{1}{1 + \exp(-\frac{V+40}{10})}$
n	$\alpha_n(V) = \frac{0.1 \times \frac{V+60}{10}}{1 - \exp(-\frac{V+60}{10})};\quad \beta_h(V) = 0.125\exp(-\frac{V+70}{80})$

[a] The m, n, h are the kinetic parameters in the standard HH model [123]; g_{Na} and g_K are the conductance densities; $\bar{g}_{Na}$ and $\bar{g}_K$ are the maximal conductance densities.

20 µm, a 10-µm-long axon hillock with a diameter of 2.5 µm and a 3100-µm-long axon with a diameter of 0.25 µm. The soma is placed 100 µm from the µChannel entrance. All external nodes in the distal well are grounded through a 10 pF capacitor to mimic the effect of stray capacitance between the electrodes and the input capacitance of the amplifier. The electric potential of external nodes inside the soma well is set to 0, which is the reference potential. The electric potential of external nodes inside the distal well mimics the input voltage into the amplifier. Extra-cellular medium inside the µChannel is modelled as a series of axial resistors: $R_{ex} = \frac{L_{comp} \cdot \rho_{ex}}{A_{\mu Chan} - A_{axon}}$ The length of the axon compartments (L_{comp}) is set to $\lambda/20$, with λ being the space constant of neurites; ρ_{ex} is the extra-cellular resistivity; and $A_{\mu Chan}$ is the cross-sectional area of the µChannel.

Two populations of voltage-dependent conductances: g_{Na} and g_K were used for the Hodgkin-Huxley model H-H model. The conductance at the axon hillock was 9-fold

higher than the conductance at the soma and normal neurite segments. The models were solved via the backward-Euler method [124]. All the details regarding the passive and active parameters are given in table 3.1.

3.4 Results

3.4.1 Hippocampal Cultures

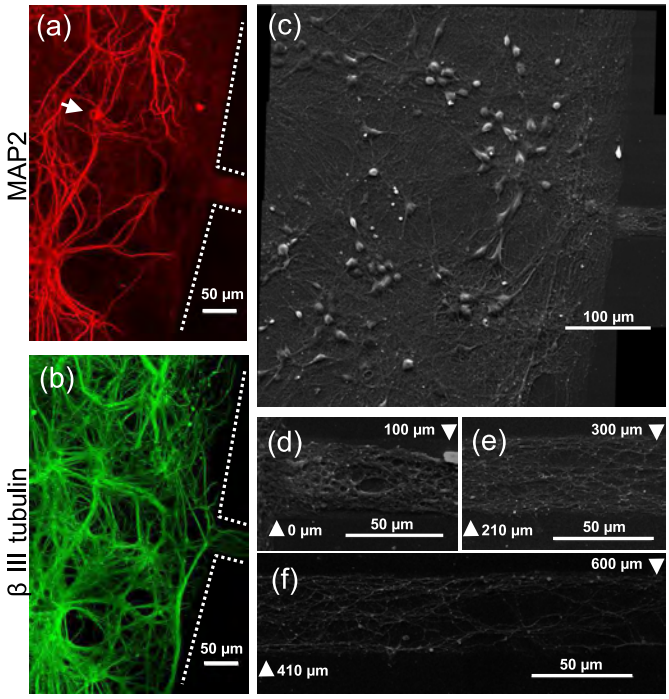

Figure 3.3. (a, b) Fluorescent images of the same cell culture near the µChannel entrance. The dashed line shows the border of the soma well and µChannel. MAP2 immunoreactive dendrites (a) rarely grew into a µChannel, while a large amount of β-III-tubulin immunoreactive neurites (b) grew into it. The arrow head marks a soma near the entrance. (c) The SEM image near the µChannel entrance of a soma well. (d-f) Dependence of the neuronal tissue density inside the µChannel on the distance from the µChannel entrance for the same sample as in (c). (d) the tissue within 100 µm of the entrance has the highest density. (e) the density decreases 200-300 µm from the entrance. (f) The density continues to decrease 400-600 µm from the entrance (in the central part of the µChannel).

After 10-14 DIV, we observed large amounts of tissue extended into the µChannels in all hippocampal cultures (N = 110) under a phase contrast microscope (data not shown). To identify the type of tissue inside the µChannels, neurites (dendrites and axons) were stained with anti-β-III-tubulin (figure 3.3 (b)) and the dendrites were also stained with anti-MAP2 (figure 3.3 (a)). Although there were large amounts of neurites inside the

μChannels, only a few dendrites were observed, indicating that most of the neurites growing in the μChannels were axons, which is consistent with previous observations [120]. The SEM image (figure 3.3 (c-f)) also shows large amounts of tissue threaded into the μChannel. Interestingly, the density of tissue near the channel entrance (figure 3.3 (d)) is much greater than it is in the middle of the μChannel (figure 3.3 (e, f)).

3.4.2 Overview of Experimental Results

The neural activity of the 110 cultures was recorded, with spike amplitudes ranging from 0.10±0.02 to 8.5±0.2 mV, L-SNR ranging from 6.2±0.8 to 428±9 and M-SNR ranging from 5.3±1.1 to 141±11 (figure 3.4). The number of units per channel was determined by spike sorting and ranged between 1 and 9, with an average of 2 units per channel. No negative leading spikes were observed, suggesting that all the spikes originated inside the soma well outside the μChannel; this is consistent with the fact that the somata were usually located more than 60 μm from the channel entrances (average 116 μm, N = 6, SD = 50 μm).

3.4.3 Spontaneous Seal

Figure 3.3 (c-f) shows a large amount of cell tissue (e.g., neurites, glia, etc.) threaded into the μChannel. Due to the high resistivity of the cell membrane which is abundant in tissue, the tissue clogging the μChannel can form a high-resistance seal (spontaneous seal), similar to the loose seal in loose patch experiments. The paired t-test on $\bar{\rho}_{pre}$ and $\bar{\rho}_{post}$ showed a significant ($p < 0.001$) increase of resistivity inside μChannels with all kinds of cross sections and channel lengths, indicating that the spontaneous seal does exist.

To quantify the magnitude of the spontaneous seal, the increase ($\bar{\rho}_{clog}$) in the overall resistivity of the μChannels at 10-14 DIV was measured and plotted (figure 3.5). The values of $\bar{\rho}_{clog}$ are averagely 1.6 times the culture-medium resistivity ($\bar{\rho}_{pre}$). The cross-section area of the μChannel (A_c) did not affect $\bar{\rho}_{clog}$ (figure 3.5 (d)). There is also no clear dependence of $\bar{\rho}_{clog}$ on the μChannel length (L_c), when L_c is shorter than 200 μm (figure 3.5 (c)). The correlation analysis confirmed this observation: $p > 0.05$ for A_c or $1/A_c$ vs. $\bar{\rho}_{clog}$; $p > 0.8$ for L_c or $1/L_c$ vs. $\bar{\rho}_{clog}$. This means that there is neither proportional nor inverse-proportional correlation between A_c or L_c and $\bar{\rho}_{clog}$ in μChannels shorter than 200 μm. Stepwise linear regression further confirmed this result, as no geometry parameters can be included inside the model (table 3.2).

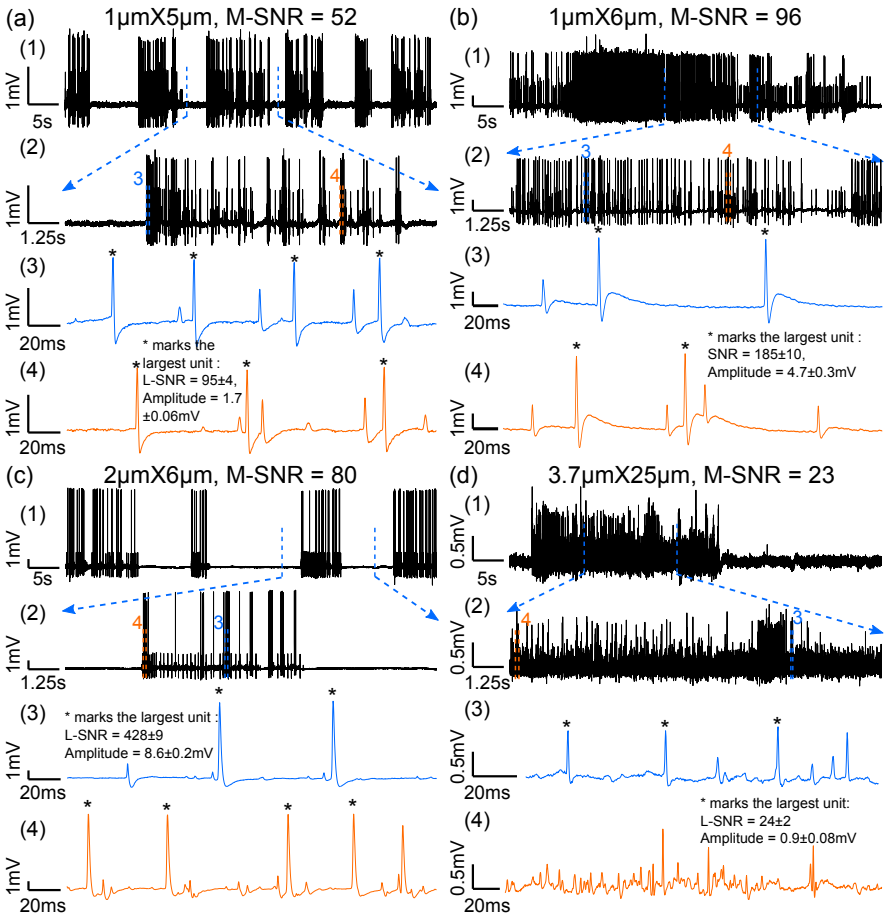

Figure 3.4. Raw data traces without any digital filtering from μChannels with various cross-sectional geometries. In each panel (a-d), sub-panel 1 shows a 1-minute signal trace; sub-panel 2 is the detail view of a 15-seconds trace taken from sub-panel 1. A short fragment (between blue dashed lines) with low density spikes is magnified in sub-panel 3; and another short fragment (between orange dashed lines) with high density spikes is magnified in sub-panel 4. The asterisks identify spikes from the unit with the largest amplitude. (a) A 1-μm-high, 5-μm-wide μChannel yielding a signal with a median SNR of 52 for all units (M-SNR), and SNR = 95±4 for the unit with the largest amplitude (L-SNR). (b) A 1-μm-high, 6-μm-wide μChannel yielding a signal with M-SNR = 96 and L-SNR = 185±10. (c) A 2-μm-high, 6-μm-wide μChannel yielding a signal with M-SNR = 80 and L-SNR = 428±9. This μChannel yielded the largest amplitude of all the μChannels. (d) A 3.7-μm-high, 25-μm-wide μChannel yielding a signal with M-SNR = 23 and L-SNR = 24±2. Large numbers of axons in wide channels result in recordings with large numbers of units, occasionally showing as a burst-like complex (d.4).

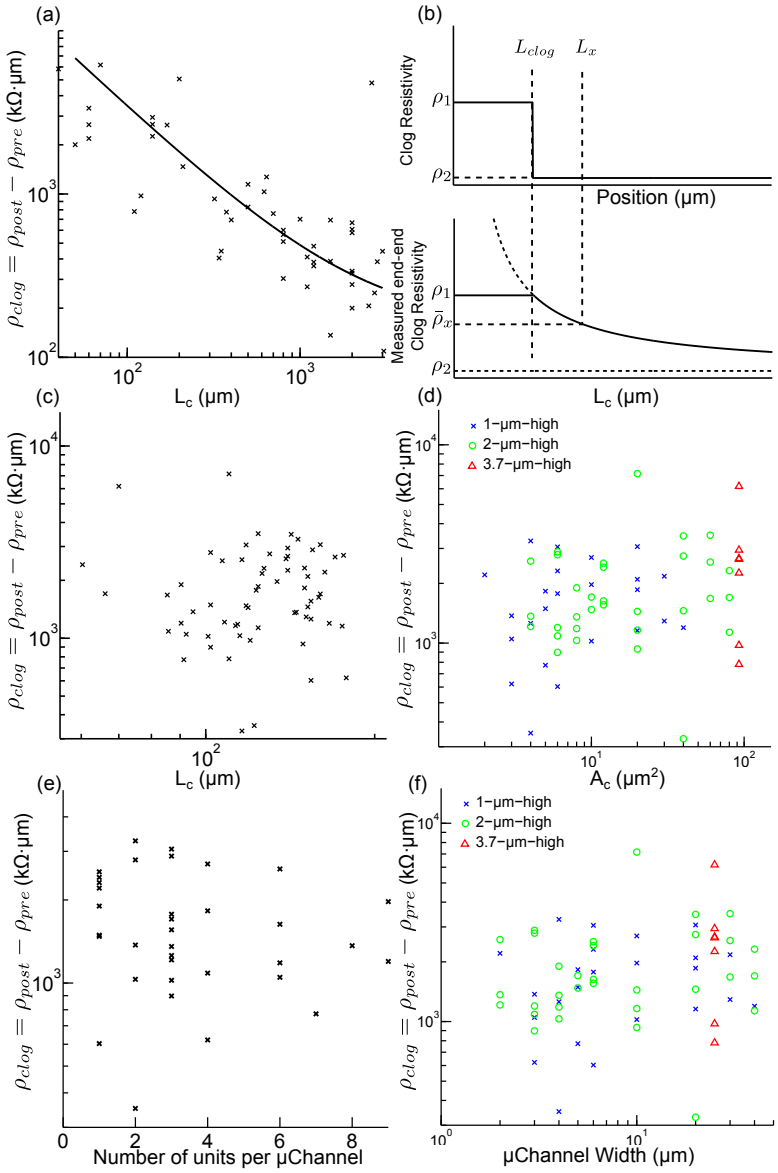

Figure 3.5. (a) Dependence of the clog resistivity (ρ_{clog}) on the channel length (L_c). All channels have the same cross-sectional geometry (3.7 µm × 25 µm). The line is the linear regression of the ρ_{clog} vs. $1/\ L_c$. (b) Step distribution of the ρ_{clog} along the channel (upper panel) can result in inversely proportional dependence of the measured ρ_{clog} on L_c. (c) the ρ_{clog} of µChannels with an A_c between 2 and 100 µm^2 is plotted against L_c ($L_c \leq 200$ µm). (d) the ρ_{clog} is plotted against A_c. The µChannel heights are identified by different marker shapes. (e) the ρ_{clog} is plotted against the number of units per channel for selected µChannels ($L_c \leq 200$ µm, $A_c \leq 12$ µm^2). (f) The ρ_{clog} is plotted against µChannel widths. The µChannel heights are identified by different marker shapes.

Table 3.2: Stepwise linear regression of the clog resistivity function[a].

Response: $\bar{\rho}_{clog}$

Potential Predictive Terms: L_c, A_c, Height (H), Width (W)

Initial Terms included: none

Final Terms included: none

Term	Coefficient[b]	Std. Err[c]	Status[d]	p-value
L_c	-0.205	0.348	OUT	0.442
A_c	-0.183	0.078	OUT	0.029
H	0.438	0.211	OUT	0.037
W	0.141	0.084	OUT	0.116

[a] $ln(\bar{\rho}_{clog}) = \beta_0 + \beta_i \times ln(X_i) + \epsilon, \in [L_c, A_c, H, W]$.

[b] Coefficient is the estimated β_i.

[c] Std. Err is the standard error of corresponding coefficient.

[d] OUT/IN means a term is excluded/included into the model.

However, interestingly, there is a significant decrease in $\bar{\rho}_{clog}$ with increasing L_c in longer µChannels (200 µm $\sim$ 3 mm, figure 3.5 (a)). The declining trends can be modelled by formula (3.1) ($p < 0.001$):

$$\bar{\rho}_{clog} = \bar{\rho}_{post} - \bar{\rho}_{pre} = \frac{323 \pm 25 M\Omega \cdot \mu m^2}{L_c} + 0.155 \pm 0.1 M\Omega \cdot \mu m^2 \tag{3.1}$$

The average $\bar{\rho}_{clog}$ in shorter µChannels ($<$ 200 µm) is about 2-fold larger than in longer ones (200-400 µm). This indicates that the spontaneous seal was concentrated within 200 µm of the µChannel entrance; consistent with the negative dependence of the tissue density on the distance from the µChannel entrance (figure 3.3 (d-f)).

$$\rho_{clog}(x) = \begin{cases} \rho_1, & 0 \leq x < L_{clog} \\ \rho_2, & L_{clog} \leq x < L_{\mu Chan} \end{cases} \tag{3.2}$$

If the model of the increase (ρ_{clog}) of the resistivity inside the µChannel due to the spontaneous seal is distributed as a step function (figure 3.5 (b) upper panel, formula (3.2)), then the overall clog resistivity measured ($\bar{\rho}_{clog}$) is actually an average ρ_{clog} over the entire length ($L_{\mu Chan}$) of the µChannel (figure 3.5 (b) lower panel), which can be expressed

as:

$$\begin{aligned}\bar{\rho}_{clog}(L_x) &= \frac{1}{L_x} \cdot \int_0^{L_x} \rho_{clog}(x)\,\mathrm{d}x \\ &= \begin{cases} \rho_1, & 0 \le L_x < L_{clog} \\ \dfrac{(\rho_1 - \rho_2) \times L_{clog}}{L_x} + \rho_2, & L_x \ge L_{clog} \end{cases}\end{aligned} \tag{3.3}$$

If $L_x > L_{clog}$, it shares the same form as formula (3.1), which fits the experimental data well. If $L_x < L_{clog}$, it does not depend on L_x, which is also suggested by the experimental data (figure 3.5 (c)). This suggests that our simplified model can already explain most of the data, although the actual distribution of ρ_{clog} may be much more complicated than the step function. Therefore, we use this step function to model the spontaneous seal in our numerical simulations described in the following sections.

The $\bar{\rho}_{post}$ in short µChannels ($L_c < 200$ µm) is averagely 3.4 times the $\bar{\rho}_{pre}$. In most cases (65 out of 71), the $\bar{\rho}_{clog}$ is more than twice as large as the $\bar{\rho}_{pre}$. This means that, after cell culture, the effective cross-section area typically shrinks down to less than half of the geometric area of the µChannel cross-section. For a channel cross-section area of 12 µm^2 and a typical axon diameter of 0.2 µm to 0.5 µm [125–127] (A < 0.2 µm^2), it can be estimated that at least 12 axons should thread the channel to achieve this effect.

However, from µChannels with a cross-section larger than or equal to 12 µm^2, only up to a maximum of 7 units per µChannel were recorded. The correlation analysis also shows there is no clear correlation between clog resistivity and number of units per channel ($p > 0.7$). In µChannels with channel width larger than or equal to 20 µm^2, the recorded signal usually contained many bursts (heavily overlapped spikes), some spike units may not be distinguishable. Thus there may be an underestimation of the axon number in µChannels with large cross-sections. (≥ 20 µm^2). Hence we limited the correlation test on selected µChannels with $A_c \leq 12$ µm^2. Figure 3.5 (e) shows there is no clear correlation between clog resistivity and number of units per channel ($p > 0.7$) either. These results are suggestive of a role of the glia in clog resistance as axons alone can not account for this resistivity increase.

3.4.4 Impact of the Channel Length (L_c) on Spike Amplitudes

To understand the dependence of spike amplitudes on L_c, a series of numerical simulations with constant A_c (92.5 μm^2) and varying L_c (30-3000 μm) were performed. Interestingly, the dependence is not monotonic (figure 3.6 (a) orange traces). The simulation shows spike amplitude increases with increasing L_c while L_c is shorter than 200 μm. As L_c increases from 200 μm to 3000 μm however, the simulation predicts a decrease in spike amplitudes.

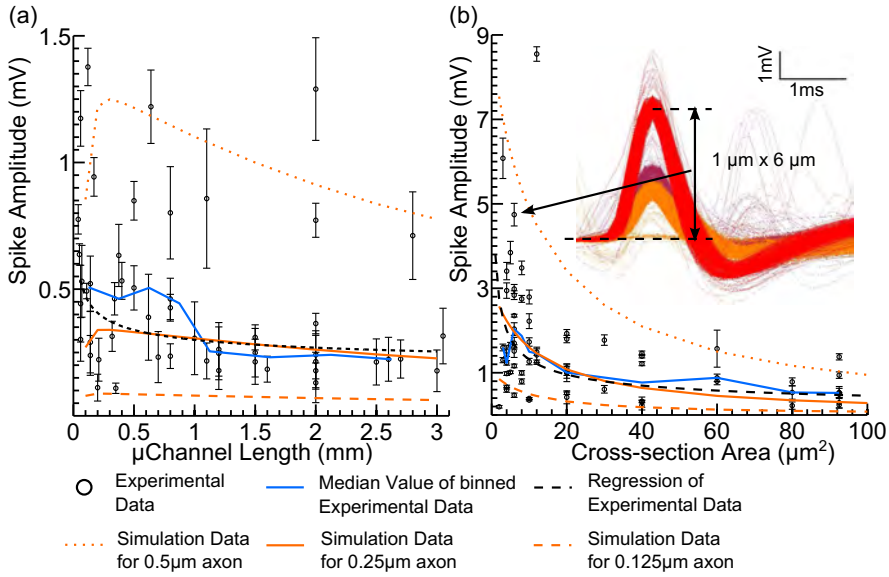

Figure 3.6. (a) The impact of the channel length (L_c) of μChannels (3.7-μm-high, 25-μm-wide) on measured spike amplitude (circles with error bars) of the highest unit obtained after spike sorting for each μChannel. The median amplitude (blue line) of every 250 μm bin of L_c and the regression result (dashed line) are compared with the simulation results (orange). The simulation results (orange) are obtained by varying L_c from 30 μm to 3100 μm, while maintaining the cross-sectional area constant (A_c = 92.5 μm^2). Amplitudes decrease with decreasing axon diameter from 0.5 μm (orange dash) to 0.125 μm (orange dot). (b) The impact of the A_c (2-100 μm^2) on spike amplitude (circles with error bars) of the highest unit obtained after spike sorting for each μChannel. L_c values range from 60 μm to 178 μm. The median amplitude (blue line) for each A_c and the multiple linear regression result (black dashed line) are compared with the simulation results (orange). The simulation results are obtained by varying A_c from 2 μm to 100 μm^2, while maintaining L_c (130 μm). (Inset) Spikes from a μChannel (1 μm × 6 μm) sorted into 3 units (red, purple and orange) aligned with the positive peaks. The spike amplitude of the highest unit (red unit in the inset) from this μChannel is plotted as a circle (arrowed).

To verify the simulation results, we experimentally investigated the relationship between L_c and the spike amplitude of the largest unit from each μChannel (figure 3.6

(a)). Data from 51 µChannels (L_c: 40 - 3050 µm, cross section: 3.7 µm × 25 µm) show a decreasing trend similar to the simulation. The correlation analysis also confirmed that spike amplitudes are significantly correlated ($R_c = 0.29$, $p < 0.05$) to $1/L_c$, i.e., the spike amplitudes are inversely-proportional to L_c. The relationship can be formulated (figure 3.6 (a) dashed black line) as:

$$Spike\ Amplitude = \frac{1.5 \pm 0.5mV}{\sqrt[3]{L_c}} + 0.15 \pm 0.07mV \tag{3.4}$$

However, the increasing trend in the range of L_c = 0-200 µm cannot be observed in end-to-end experiments, because of the relatively large spread of data. This large spread could result from a lack of control over other important parameters, e.g., the diameter of the axons, ion-channel densities, length of axons inside the µChannel, etc. Three series of simulations with different axon diameters demonstrated that the maximum spike amplitudes can vary from 0.1 mV (0.125-µm diameter, dashed orange trace) to 1.3 mV (0.5-µm diameter, dotted orange trace).

In contrast to end-to-end experiments, intrachannel recordings of the same µChannel show an increasing trend of amplitudes in the first 200 µm, similar to the simulation results. This is because of obtaining data from the same population of axons by intrachannel electrodes can minimize the deviation introduced by parameters other than the channel length (figure 3.7 (a, b)). All the spikes from a single unit show the same trend: spikes recorded from the 2nd electrode (129 µm) always have the largest amplitude and closer to or further from the entrance of the soma well, there is always amplitude attenuation. The simulation result (figure 3.7 (d)) shows a similar trend.

Figure 3.7 (c) shows the development of extracellular electrical currents inside the µChannel during the simulation of an AP propagating through the µChannel. At certain moments after the AP propagating into the µChannel, e.g., 1.4 ms in figure 3.7 (c), the directions of longitudinal extracellular currents are opposite at the positions of the different intrachannel electrodes. This phase cancelling effect (PCE) may be partially responsible for the non-monotonic dependence of amplitudes on the L_c (see discussion).

3.4.5 Impact of the Channel Cross Section on Spike Amplitude

To understand the dependence of the spike amplitudes on the cross-sectional area (A_c), a series of numerical simulations with different A_c (2-100 µm^2) and constant L_c (130 µm) were performed. As expected, the signal amplitudes monotonically decreased

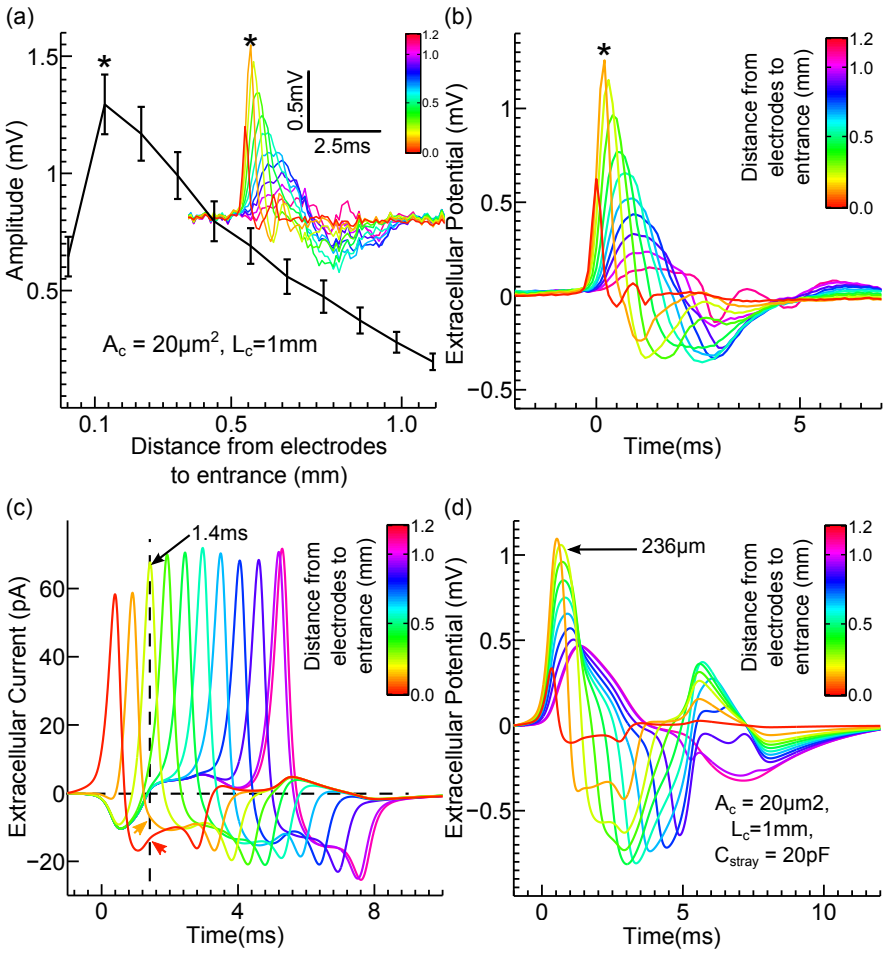

Figure 3.7. (a) The dependence of the spike amplitudes on the position of MEA electrodes. Data were obtained via intrachannel recording from a 1-μm-high, 20-μm-wide and 1-mm-long μChannel. The inset shows a single unaveraged spike recorded by different electrodes. Colour indicates the distance away from the μChannel entrance closest to the soma well. (b) The dependence of the averaged spike waveform (n = 239) on the electrode distance to the entrance of the channel, from 22 μm (red trace) to 1092 μm (pink trace). The electrode at 129 μm from the entrance recorded the waveform with the biggest amplitude (orange trace, star marked). (c-d) Simulation results of the compartment model with 1-mm-long, 1 μm × 20 μm μChannel. (c) The extracellular current waveform at different places inside the μChannel, from 22 μm (red trace) to 1092 μm (pink trace) from the entrance. At 1.4 ms the current at 236 μm (light green trace) reaches the maximum value, while the currents closer to the entrance (red (22 μm) and orange (129 μm), traces arrowed) have already become negative. (d) Action potential waveforms at different places inside the μChannel show the same variation pattern as the experimental data shown in (b).

Table 3.3: Stepwise linear regression result of the spike amplitude function[a].

Response: Spike Amplitudes

Potential Predictive Terms: L_c, A_c, $\bar{\rho}_{post}$

Initial Terms included: none

Step 1, added Term 2, p=5.67241 $\times 10^{-5}$

Step 2, added Term 3, p=0.0283412

Final Terms included: 2, 3

Term	Coefficient[b]	Std. Err[c]	Status[d]	p-value
L_c	-0.407	0.399	OUT	0.313
A_c	-0.459	0.093	IN	0.000
$\bar{\rho}_{post}$	0.281	0.125	IN	0.028

[a] $ln(Amplituide) = \beta_0 + \beta_i \times ln(X_i) + \epsilon, \in [L_c, A_c, \bar{\rho}_{post}]$.

[b] Coefficient is the estimated β_i.

[c] Std. Err is the standard error of corresponding coefficient.

[d] OUT/IN means a term is excluded/included into the model.

with increasing A_c (figure 3.6 (b) orange traces). If we assume a constant extra-cellular current, then a smaller A_c results in a larger extra-cellular resistance of the μChannel, which can lead to a larger potential drop along the μChannel.

The scatter plot of actual amplitudes vs. A_c from 66 end-to-end experiments (L_c = 60-178 μm, Mean: 125 μm, SD: 24 μm, figure 6 (b)) shows a similar decreasing trend, thus confirming that μChannels with smaller A_c can yield larger amplitudes. The correlation analysis shows that there is no significant correlation between L_c and spike amplitudes (R_c = -0.2, $p > 0.1$) or between $1/L_c$ and spike amplitudes (R_c = 0.2, $p > 0.1$). However, $1/A_c$ is significantly positively correlated to amplitudes (R_c = 0.5, $p < 0.001$) while $\bar{\rho}_{post}$ does not show any significant correlation with amplitudes, due to the strong interference of A_c. After cancelling the effect of A_c by multiplying the amplitudes by A_c, $\bar{\rho}_{post}$ does show positive correlation (R_c = 0.3, $p < 0.04$). Stepwise linear regression (table 3.3) further confirmed this result: L_c cannot be included in the statistic model; whereas, A_c ($p < 0.001$) and $\bar{\rho}_{post}$ ($p < 0.03$) do have significant impacts on the model. The relationship can be expressed as:

$$Spike\ Amplitude = 41.1\mu V \times \frac{\rho^{0.281\pm0.12}}{{A_c}^{0.459\pm0.09}} \tag{3.5}$$

The paired t-test was applied to amplitudes from different aspect ratios but the same A_c. The aspect ratio does not show any significant effect on amplitudes ($p > 0.35$) either.

Small cross sections also dramatically reduce the number of units which are recorded from, i.e. reducing the chance of recording heavily overlapped units (figure 3.4). This facilitates data analysis in comparison to the large cross-section (3.7 μm × 25 μm) version.

3.4.6 Dependence of Signal to Noise Ratio (SNR) on μChannel Geometry

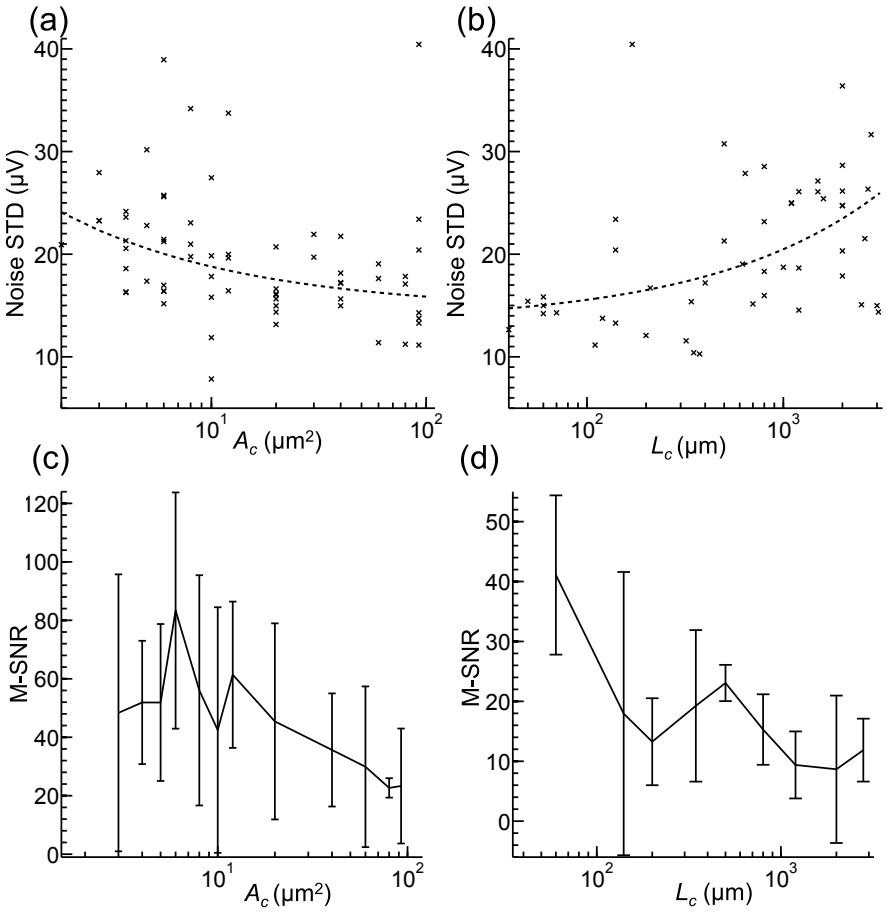

Figure 3.8. (a-b) The dependence of the noise standard deviation (RMS noise) on A_c (a) and L_c (b). The dashed lines show the linear regression of RMS noise against $1/\sqrt{A_c}$ (a) and against $\sqrt{L_c}$ (b). (c-d) The median signal-to-noise ratio (M-SNR) as a function of A_c (c) and L_c (d). Please see methods section for details.

The thermal noise level from a resistive channel should correlate to the square root of its overall resistance, which is a function of L_c and A_c: $R = \frac{\rho \cdot L_c}{A_c}$. Figure 3.8 (a, b) shows that RMS noise level is inversely proportional to $\sqrt{A_c}$ and proportional to $\sqrt{L_c}$. The correlation analysis also confirmed this result: $R_c = 0.28$, $p < 0.02$ for $\sqrt{1/A_c}$; $R_c = 0.46$, $p < 0.001$ for $\sqrt{1/L_c}$. As mentioned before, spike amplitudes increase while L_c or A_c decreases. Therefore, the SNR increases with decreasing A_c (figure 3.8 (c)) and decreasing L_c (figure 3.8 (d)). The correlation analysis also confirmed this result: SNR showed significant positive correlation to $\sqrt{1/L_c}$ ($R_c = 0.45$, $p < 0.001$) and $\sqrt{1/A_c}$ ($R_c = 0.32$, $p < 0.01$).

The µChannels with smaller cross sections ($A_c \leq 12$ µm^2, N = 36) may have average M-SNR values (65±35) that are significantly larger ($p < 0.005$) than the M-SNR values (40±26) of larger cross section µChannels ($A_c > 12$ µm^2, N = 29). The SNR of the largest units (L-SNR) from the small cross section group is 18±4 - 428±9, with a mean value of 101±76, which is comparable to the maximum SNR obtained from CNT coated electrodes (∼135 [54]) and from Si-NWFET (∼210 [55] and ∼120 [56]), comparing to the typical SNR (5 - 40) of traditional MEAs [46, 47].

3.5 Discussion and conclusions

In an alternative approach to neuron-interfacing we have demonstrated that axons spontaneously threading µChannels support stable recordings with excellent SNRs. Indeed, when an AP propagates along a neurite inside the µChannel, part of the outward trans membrane currents are forced to flow via the resistive extracellular path in the µChannel (see figure 3.2). These currents generate a recordable electrical potential difference along the µChannel whose SNR we anticipated can be optimised by informed design of the µChannel geometry.

The reduction of the intrachannel volume available for current flow due to threading neurites, glia and debris accumulation can amplify this signal by raising the extracellular resistivity in the µChannel. A smaller A_c also increases the resistance per unit length, thereby increasing the amplitude of the signal.

In µChannels shorter than 200 µm, increasing L_c yielded larger spike amplitudes due to an increase in overall resistance. However, when in the case of long channels, ($L_c > 200$ µm), the opposite result is observed in both simulations and experiments.

There are 2 mechanisms which can lead to this result:

1) Low-pass filtering effect. The high resistance of the μChannel combined with stray capacitance acts like a first-order low-pass filter and attenuates high-frequency ($\omega = 1/(R \cdot C)$) signal amplitudes, i.e., positive peaks of AP. The longer the channel, the higher the resistance, the lower the cut-off frequency, the smaller the amplitude. This hypothesis is consistent with the clear increase in spike widths at electrodes further from the soma well (figure 3.7 (b)).

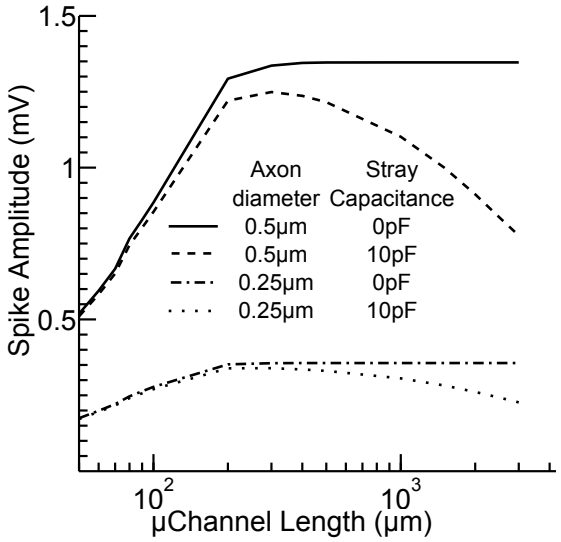

Figure 3.9. The phase cancelling effect and the low pass filtering effect due to stray capacitance. Simulation results are obtained by varying the channel length (L_c) from 30 μm to 3100 μm, while maintaining the cross-sectional area constant (A_c = 92.5 μm^2). After the spike amplitude reaches a maximum value at the transition length (L_c=200 μm for 0.25-μm-diameter axon or L_c=300 μm for 0.5-μm-diameter axon), the spike amplitude decreases (dashed and dotted line) with increasing L_c, when there is a stray capacitance of 10 pF, due to the low pass filtering effect. Even without any stray capacitance (solid and dash-dotted traces), the spike amplitude cannot continue to increase beyond 200-300 μm, due to the phase cancelling effect.

2) Phase cancelling effect (PCE). Numerical simulations (figure 3.9) demonstrate that even without any stray capacitance, the signal amplitude cannot increase continuously beyond the transition length (∼200 μm for an axon with a 0.25-μm diameter; ∼300 μm for an axon with a 0.5-μm diameter). This indicates that the phase cancelling effect (PCE) does play an important role in restricting signal amplitudes.

As the AP propagates along the axon with finite speed (0.3-10 m/s, [128, 129]), at any given moment different membrane patches at different positions along the axon are at different stages of the AP. As a result, after AP propagating into the µChannel (figure 3.11 (d, f) time point 4) an active axon in the channel simultaneously produces extracellular currents of opposite longitudinal directions at different positions (figure 3.7 (c)).

Because the measured end-to-end voltage is the integral of the electric field along the entire extension of the channel, same-direction currents will contribute constructively, whereas, opposite currents will summate destructively, thus preventing the spike amplitude from increasing monotonically along the channel.

In detail, the PCE sets in once the µChannel is longer than the positive-phase spreading length (L_1/L_2 in figure 3.11 (c, e)) of the longitudinal extracellular current; PCE therefore depends on µChannel length and conduction velocity of axons (CV). For a given µChannel, the faster the AP propagates along the axon, the wider the positive phase can spread along the axon (figure 3.10 (e, f) and 3.11 (e, f)), therefore the smaller the PCE. Thus axons with higher conduction velocity, e.g., axons with larger diameters or axons of DRG neurons, have longer transition lengths (figure 3.9).

To obtain the best SNR, signal amplitude and frequency response, a µChannel should be around 50 - 200 µm long, with a cross section of less than 12 μm^2. Such µChannels yielded signal amplitudes as large as 2 mV on average and up to 8.6 mV at maximum, resulting in an L-SNR as high as 101 on average. The channel height should be around 1 µm; lower channels (< 0.5 µm) will prevent most large neurites from growing into them.

In addition, compensating stray capacitance and input capacitance, by a positive feedback circuit as in patch-clamp amplifiers, is going to improve spike amplitudes, too. Though the improvement is still limited by the phase-cancelling effect, the compensating strategy can be extremely useful in certain circumstances where shortening µChannel length is not an option or not easy to achieve.

Moreover, due to the low-pass filtering effect, long channels distort the AP shape. Short channels with higher cut-off frequencies are definitely better for AP shape analysis, especially for fast ionic currents.

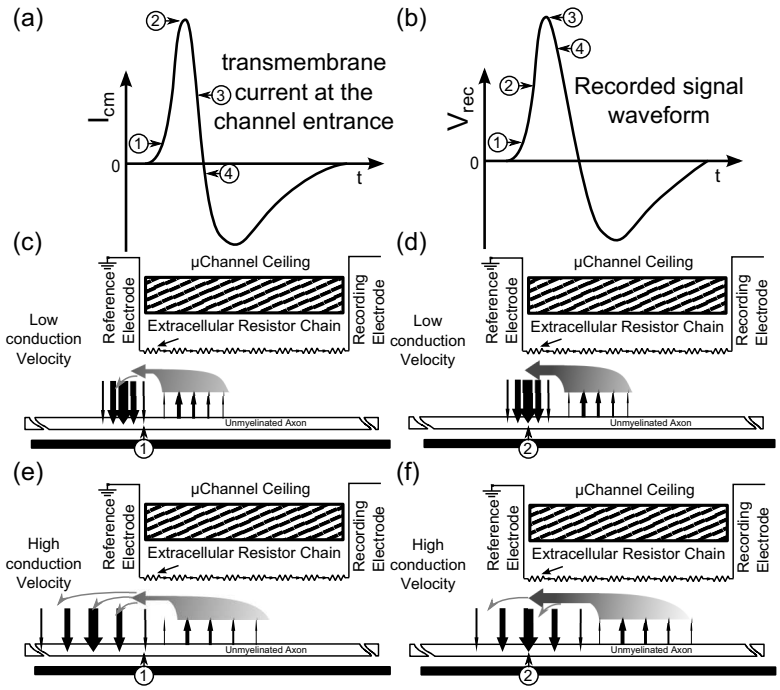

Figure 3.10. The phase-cancelling part I. (a) The transmembrane current (I_{cm}) of the membrane patch at the channel entrance. (b) The recorded signal waveform (V_{rec}). (c, d) illustrate the phase-cancelling effect (PCE) on axons with low conduction velocity (CV). (e, f) illustrate the PCE on axons with higher CV. During AP propagation, the I_{cm} (black arrows, the bigger the black arrow, the stronger the current) varies with time and position. When the AP starts to enter the μChannel, I_{cm} of the membrane patch at the channel entrance will first flow inwardly (positive in (a)), due to Na channel opening, then flow outwardly (negative in (a)) due to K channel opening. At time point 1 (c, e), I_{cm} starts to cause a leftward longitudinal extracellular current (I_{ex}, grey arrows), which leads to a positive voltage (V_{rec}) on the recording electrode (b). The more Na channels open, the stronger the inward I_{cm} becomes, the stronger the I_{ex}, the higher the V_{rec}. At time point 2 (d, f), the inward I_{cm} at the channel entrance reaches its maximum value (a), and the Na channels inside the μChannel near to the channel entrance also start to open, leading to a stronger I_{ex}.

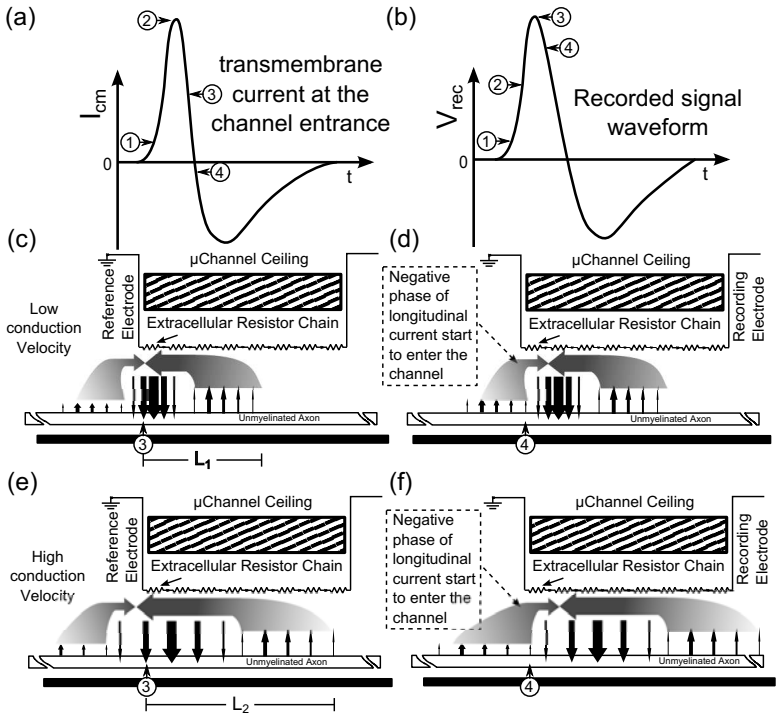

Figure 3.11. The phase-cancelling part II. At time point 3 (c, e), the I_{cm} outside the μChannel starts to flow outwardly and the negative-phase of I_{ex} enters the μChannel. Thus, I_{ex} can not increase further, resulting in V_{rec} reaching its positive peak (b). At time point 4 (d, f), the I_{cm} at channel entrance starts to flow outwardly (a). Thus the negative phase of I_{ex} becomes stronger and reaches deeper into the μChannel, resulting in V_{rec} dropping. L_1 and L_2 represent how far the positive phase of I_{ex} can spread inside the μChannel ($L_2 > L_1$ as the I_{cm} distribution is wider for high-CV axons). At time point 3, the extracellular resistors outside this range do not contribute to the V_{rec} generation due to lack of longitudinal extracellular current. Hence, a μChannel longer than L_1 for low-CV axons or L_2 for high-CV axons will not increase the signal amplitude, but μChannels shorter than L_1 or L_2 will reduce it.

3. BIOPHYSICS OF MICROCHANNEL-ENABLED NEURON-ELECTRODE INTERFACES

The spontaneously sealed μChannel may also act as a fluid/chemical barrier to facilitate pharmacological study in different neuronal compartments. For example, in our simple device, the target compound can be applied either to the compartment on the soma side or to the distal axon compartment. Because the recorded signal waveform should depend on the ionic-current distribution of both compartments, we should be able to study the distribution of ion-channel types or effects of target chemical compounds on different sub-cellular compartments.

Further, we shall also investigate the possibility of using μChannel arrays to record neuronal-network multi-site activity at high SNRs to support network studies.

Chapter 4 Microchannel enhanced electrophysiology platform for functional ion-channel profiling on axon compartment

4.1 Abstract

We have previously described that the use of microchannels as substrate-integrated equivalents of micropipettes is a potentially high-throughput, low-cost alternative to conventional multi-electrode arrays with a moderate-to-low complexity of use. By studying the biophysics of the signal generation inside microchannels, we established the impact of microchannel shape on signal amplitude and SNR. We also demonstrate that optimized microchannels yield spike sizes in the millivolt range with relatively high SNR (∼101). In this chapter, we continue to explore the biophysics behind the signal generation to reveal the dependence of recorded electrical signals on biology criteria of the neuron (such as ion-channel distribution, ion-channel types and axon diameters). By experimental data and numerical simulation, we demonstrate that the recorded signals are only affected by the membrane patches located inside the microchannel or within ∼100 μm to the microchannel entrances. This renders it a promising technique for high-throughput automatic ion channel screening at subcellular level. This subcellular ion channel profile can provide important information about demyelination disorders such as multiple sclerosis, and even learning/memory disorders.

4.2 Introduction

Ion channels are large family of pore-forming proteins which regulate the ion currents across the plasma membrane. Thus they are indispensable to maintain membrane potential of neurons and key elements of neuronal information processing. Their subcellular localization is an important determinant of the spiking pattern and the computational role of the neuron [130]. The subcellular clustering of ion channels is also necessary for correctly transmitting action potential (AP). Hence there are a substantial number of neuropathies caused by ion-channel disorders.

4. MICROCHANNEL ENHANCED ELECTROPHYSIOLOGY PLATFORM FOR FUNCTIONAL ION-CHANNEL PROFILING ON AXON COMPARTMENT

Most known channelopathies are due to missense or nonfunctional mutations of ion channel structures. However, there are also some neuropathies are mainly manifested as abnormal distribution of normal ion channels. For example, multiple sclerosis (MS), a chronic and progressive inflammatory neurodegenerative disease of the central nervous system, for which no cure exists. Its neurological symptoms are mainly attributed to several ectopic distribution of ion channels after the demyelination: up-regulation, in the demyelinated area on axons, of Na^+ [131], K^+ [132, 133], Ca^{++} [134] channels, etc. Therefore, researchers are labouring to find target ion channel subtypes and develop corresponding chemical compounds as subtype-specific channel blockade. Recently, several fast-delayed-rectifier-potassium-channel blockers, such as 4-Aminopyridine (4-AP) and 3,4-Diaminopyridine (3,4-DAP) are tested in patients [135]. Conceivably, a high-throughput ion-channel profiling tool for obtaining the ion-current type and density on the axon compartment can speed up these studies.

Also, in basic neuroscience research, there is increased attention on subcellular distribution of ion channels. Besides the great variety of genes responsible for ion channel expression, the variability in the subcellular localization of ion channels is considered as one of the important factors to expand the neuronal diversity [136, 137]. The nonuniform distribution of potassium channel in dendrites has already been proved to play a vital role in dendritic computation [138]. Traditionally, axon is only regarded as an information conveyor between soma and presynaptic compartments of synapses. In this view, the information processing is only happened in soma, synapses and dendritic arbours. Recently, new emerging evidence imply axons can also perform a computation role in information processing of the neuronal circuits [139, 140].

There are many evidences imply the variances of ion channel profile on axon compartments may also modulate presynaptic AP frequency and waveform in axons and terminals. Different ion channel profiles can facilitate produce or cease AP reflection in axons which may enhance the synaptic transmission [141]. The AP can also be gated directly in axon compartments during transmission [142–144]. Cumulative inactivation of potassium channel mediates activity-dependent spike broadening which can contribute to control of glutamatergic synapse efficacy by prolongation of the presynaptic voltage waveform [145].

More recent evidence indicates the AP is rather analog than digital in the role of modulating transmitter release [146, 147]. A detailed study on layer 5 pyramidal neurons

[148], implied that high density of Kv1 on axon can shorten the duration of cortical axonal APs. This can lead to an increase of the fidelity of axonal AP propagation during high-frequency AP firing. More important, varying the Kv1 channel profile can modulate transmitter release. Hence the ion channels and their distribution are regarded as important players in the plasticity of neural circuits.

Moreover, many studies also show that during development and ageing, there is a clear variation of ion channel types and density on subcellular compartments of neurons in CNS [149–153]. This variability may be one of the probable mechanisms by which neurons may gain plasticity required for learning processes. The time-dependent variation of ion-channel profile during development may link to the regulatory mechanisms of synaptogenesis and synaptic activity [149, 154].

Therefore, the data revealing the ion channel profile on subcellular compartments and its time dependence are considered to have serious impact on developing ion-channelopathy therapies, and understanding learning processes and memory formation. Many researchers already focus on profiling ion channel distribution in CA1, CA3, DRG or other CNS regions by immunohistology, in situ hybridization, RT-PCR, etc.[149, 151–153, 155].

Although electrophysiology study specified on axonal membrane can provide more intuitive information about the ion-channel density and functionality, due to difficulty of forming gigaseal on axons with relative small diameters of many cell types, the electrophysiological data are very rare [139, 148, 155–157]. Therefore, improved direct electrophysiological recording methods on axon compartments are demanding for yielding new insights into the axons, APs and related mechanisms in learning and memory processing [139].

Because the AP waveforms and related ion currents can have large difference between the soma and the axon [142, 148], methods only recording APs from the soma or those methods which cannot identify the position where the APs are recorded are not suitable. Usually, as an alternative to patch clamp, suction electrode recording is applied on axons to study the ion-current. Briefly, an axon end was drawn into a glass capillary electrode with a constricted orifice. The AP in the axon causes a current leaked from glass electrode to the bath which is recordable by the patch-clamp amplifier [150]. However it is still a labouring manual technique lack of high-throughput potential.

4. MICROCHANNEL ENHANCED ELECTROPHYSIOLOGY PLATFORM FOR FUNCTIONAL ION-CHANNEL PROFILING ON AXON COMPARTMENT

Automated patch clamp methods, recently developed for suspended cell lines, such as PatchXpress (Molecular Devices, Inc.), Ionworks population patch clamp (Molecular Devices, Inc.), and Qpatch (Sophion Bioscience, Inc.), can facilitate understanding mechanisms of the pathology of mutated ion-channels, and enables fast ion screening drug discovery. But it is difficult to apply them to the neuronal culture or to a specific neuronal subcellular compartment. The MEA based techniques are good for monitoring the cultured neuronal networks. But the spike waveforms depend on many criteria, such as the distance from electrodes to signal sources [158], and the signal source location relative to the soma [60, 61]. The complexity of the signal waveform, companying with the low signal to noise ratio (SNR), make it difficult to identify the origin subcellular compartment of a spike unit.

Alternatively, an optimized micro-channel resembling suction electrode can provide stable AP waveforms with relatively high mean SNR (101±76, chapter 3), even comparable to the maximum SNR obtained with CNT-coated electrodes (∼135 [54]) or Si-NWFET (∼210 [55], and ∼120 [56]). To avoid manually suck the axon into glass pipette, in our technique, the axons spontaneously threaded into the micro-channel, causing a high resistive spontaneous seal (chapter 3). The micro-channels are integrated into the substrate to provide mechanical stability superior to the hanging glass pipettes. In this paper, we studied the signal waveform related to the biological criteria of recorded neurons and also demonstrate the potential applications of micro-channel enhanced electrophysiology platform in pharmacology study in cultured mammalian cells.

4.3 Methods

4.3.1 Device Fabrication

The polymer microchannel devices were fabricated via previously established procedures (chapter 3). Briefly, a 5-mm-thick slab of PDMS was cured onto the master, peeled off, and punched to form two culture wells (6 mm in diameter).

The MEAs were also fabricated according to the previously described method (chapter 3). A 100-nm-thick ITO layer on the glass substrate was etched to form 40-μm-wide electrodes with 60-μm separation. Before culturing, the MEA was cleaned using oxygen plasma for 15 mins in a PDC-002 plasma oven (Harrick Scientific) to enhance hydrophilicity.

4.3.2 Cell culture and electrophysiology

Dissociated cultures of mouse hippocampus neurons were prepared as described previously (chapter 3). In all pharmacology experiments the polystyrene dishes were used as culturing substrate. For obtaining conduction velocity the SiO_2 surface of the MEA acted as the substrate.

Pharmacology experiment I:

To study the effect of applying channel blockade in different compartments, electrophysiology recordings were conducted in a humidified incubator (37°C, 5% CO_2) at 14 DIV with an Aleria 600A amplifier (Aleria Biodevices) at modified gain (×240). For each device, a control state was recorded with both well filled with Neurobasal (NB) (Invitrogen). Then 4-Aminopyridine (4-AP) (Sigma) was applied to soma-well or distal-well with a final concentration about 0.3 mM.

Pharmacology experiment II:

To obtain the dosage response curve, electrophysiology recordings were conducted with a normal Aleria 600A amplifier (Aleria Biodevices). The culture wells were superfused with the culture medium preheated to 37°C. After obtaining the control state, the soma-well was superfused with culture medium containing various concentrations of 4-AP. For each concentration, the recording lasted at least 10 mins.

MEA experiments:

To obtain the conduction velocity of axons, several cultures on MEAs were recorded in a dry incubator as described previously (chapter 3). The data were analyzed according to previously described procedures (chapter 3) to detect and sort the spikes.

4.3.3 Numerical simulation of compartment models

Models were written in M script language and computed using MATLAB. By default, a neuron model consists of a 100-µm-long dendrite with a diameter of 1 µm, a 20-µm-long soma with a diameter of 20 µm, a 10-µm-long axon initial segments with a diameter of 2 µm, a 1000-µm-long unmyelinated axon with a diameter of 0.25 µm and a 150-µm-long microchannel with a cross-section area (A_c) of 10 μm^2. The soma is placed ∼400 µm from the microchannel entrance.

Table 4.1: Hodgkin - Huxley model parameters I

Passive components			
Extracellular resistivity		$\rho_{ex} = \begin{cases} 2.55\Omega \cdot m;\ L_x \leq 200\mu m \\ 1.04\Omega \cdot m;\ L_x > 200\mu m \end{cases}$	
Intracellular resistivity	$\rho_i = 0.7\Omega \cdot m$	Leak membrane conductance density	$g_L = 0.7S/m^2$
Membrane capacity	$C_m = 0.01F/m^2$	Leak Nernst potential	$E_L = -57mV$

Active components[a]			
Voltage-dependent Na^+ channel		$g_{Na} = \theta_{Na} \cdot \bar{g}_{Na} \cdot m^3 \cdot h$	
Fast delayed rectifier K^+ channel		$g_F = \theta_F \cdot \bar{g}_F \cdot n^4 \cdot l$	
Slow delayed rectifier K^+ channel		$g_S = \theta_S \cdot \bar{g}_S \cdot a^2 \cdot (b_1 + b_2)/2$	
Na^+ Nernst potential	$E_{Na} = 66.5mV$	K^+ Nernst potential	$E_K = -85.7mV$

[a] The m, h, n, l, a, b1, b2 are the ion-channel kinetic parameters in pyramidal neurons (adapted from [151, 159, 160]). θ is the fraction of unblocked ion-channels. For example, $\theta_{Na} = 1$ means there is no blocker for the voltage-dependent Na^+ channels; $\theta_F = 0$ means all fast delayed rectifier K^+ channels are blocked.

To simulate the effect of 4-AP on the recorded signal (V_{rec}), two populations of voltage-dependent ion channels, a fast delayed rectifier g_F and a slow delayed rectifier g_S were used in this chapter instead of one mixed potassium conductance in the previous chapter. The kinetics of g_F (table 4.1, 4.2) were modelled as the 4-AP sensitive current in pyramidal neurons [151, 160]. The kinetics of g_F (table 4.2) were modelled as the 4-AP insensitive current in pyramidal neurons [151, 160]. The kinetics of voltage-dependent sodium conductance g_{Na} (table 4.2) were modelled as the voltage-dependent sodium channel in pyramidal neurons [159].

An additional rate factor (θ) for each active conductance at each compartment was used to mimic the blockade effect (table 4.1). For example, $\theta_F = 0.5$ means 50% of the fast delayed rectifier K^+ channels are blocked.

To mimic the dosage effect of the blockade, the hill equation were used to relate the blockade concentration and the fraction of unblocked ion channels which is the θ in our model:

$$\theta = \frac{K_d}{K_d + [L]^n} = \frac{(K_A)^n}{(K_A)^n + [L]^n}$$

θ is the fraction of unoccupied sites, i.e. functional ion channels

$[L]$ is the free ligand concentration, i.e. the concentration of the blockade
K_d is the apparent dissociation constant
K_A is the blockade concentration blocking 50% of targeted ion channels, i.e. the IC50 value.
n is the Hill coefficient.

In the model of this chapter, 4-AP only affects θ_F, with a K_d of 0.08 mM, a n of 1 [161].

Table 4.2: Hodgkin - Huxley model parameters II.

Kinetic parameters[a]	
For all parameters	$\tau_x(V) \cdot \frac{dx(V,t)}{dt} = x_\infty(V) - x(V,t); \quad x \in [m,\, h,\, n,\, l,\, a,\, b_1,\, b_2];$
m	$\tau_m(V) = \frac{1}{\alpha_m(V) + \beta_m(V)}; \quad m_\infty(V) = \frac{\alpha_m(V)}{\alpha_m(V) + \beta_m(V)};$ $\alpha_m(V) = \frac{0.182(V+35)}{1 - e^{-\frac{V+35}{9}}}; \; \beta_m(V) = \frac{-0.124(V+35)}{1 - e^{\frac{V+35}{9}}}$
h	$\tau_h(V) = \frac{1}{\alpha_h(V) + \beta_h(V)}; \quad h_\infty(V) = \frac{1}{1 + e^{\frac{V+65}{6.2}}};$ $\alpha_h(V) = \frac{0.025(V+50)}{1 - e^{-\frac{V+50}{5}}}; \; \beta_h(V) = \frac{-0.0091(V+75)}{1 - e^{\frac{V+75}{5}}}$
n	$\tau_n(V) = 0.34 + 0.92e^{-(\frac{V+71}{59})^2}; \quad n_\infty(V) = \frac{1}{1 + e^{-\frac{V+47}{29}}};$
l	$\tau_l(V) = 8 + 49e^{-(\frac{V+73}{23})^2}; \quad l_\infty(V) = \frac{1}{1 + e^{\frac{V+66}{10}}};$
a	$\tau_a(V) = \frac{1}{\alpha_a(V) + \beta_a(V)}; \quad a_\infty(V) = \frac{\alpha_a(V)}{\alpha_a(V) + \beta_a(V)};$ $\alpha_a(V) = \frac{0.0087(V-11.1)}{1 - e^{-\frac{V-11.1}{13.1}}}; \; \beta_a(V) = \frac{5}{3(-0.0053 + 0.01938e^{-\frac{V+1.27}{71}})}$
b_1	$\tau_{b_1}(V) = 360 + (1010 + 23.7(V+54))e^{-(\frac{V+75}{48})^2};$ $b_{1\infty}(V) = \frac{1}{1 + e^{\frac{V+58}{11}}};$
b_2	$\tau_{b_2}(V) = 2350 + 1380e^{-0.01118V} - 210e^{-0.0306V};$ $b_{2\infty}(V) = \frac{1}{1 + e^{\frac{V+58}{11}}};$

[a] The m, h, n, l, a, b1, b2 are the ion-channel kinetic parameters in pyramidal neurons (adapted from [151, 159, 160]).

4.3.4 The advection and diffusion analysis

To characterize the transport of chemical compounds, applied in the soma-well or distal-well, in microchannel devices, 0.1 mM Lucifer yellow CH dipotassium salt (LY) (Fluka) was applied to one of the two wells in our devices. The fluorescence intensity is recorded by a CCD camera (DP72; Olympus) mounted on a Nikon E600 microscope.

The camera is controlled by Metamorph software package. The data is then analyzed by MATLAB.

To study the flow speed and diffusion pattern in microchannel devices without any cell culture, the variations of fluorescence intensity under 3 different conditions were carried out for each channel (inset of figure 4.8 (b)):
EXPa. ∼200 µL of NB was maintained in the left well, then ∼100 µL 0.1 mM LY was added into empty right well. Thus the left well has higher liquid level than the right well.
EXPb. ∼100 µL of NB was sucked out from left well, at the same time another 100 µL 0.1 mM LY was added into right well. Thus the right well has higher liquid level than the left well.
EXPc. After the LY completely filled up the microchannel, the liquid level was reversed again.

For devices containing the cell culture, only EXPa and EXPb was performed.

For each site of a microchannel, a background fluorescence image was captured when the channel is filled up with Neurobasal culture medium as the negative control. After all experiments is finished. A fluorescence image was captured when the channel is filled up with 0.1 mM LY as the positive control. For all experiments, the camera parameters and optical filter sets were remained unchanged. For each fluorescence image, a phase contrast image was also captured to facilitate the image registration (image alignment and image stitching). The geometries of microchannels involved in these experiments were: 1-mm × 25-µm × 3.7-µm and 1-mm × 50-µm × 3.7-µm.

During data analyses, the mean intensity of negative control is regard as 0% and the mean intensity of positive control is regard as 100%. At least 10 landmarks were extracted via SIFT method with the VLFeat library for all the phase-contrast images of each device. Then the transform matrices were generated from the landmarks, which were used to register fluorescence images for each device. A Hough-transform based algorithm was used for automated microchannel recognition and image cropping.

The cell tissue inside microchannel forming local low-intensity regions, for example, the arrowed black spots in figure 4.1, can lead to underestimating the fluorescence intensity. To avoid the interference of the cell tissue, a mask was generated for each fluorescence images to exclude the low intensity regions. An adaptive local threshold

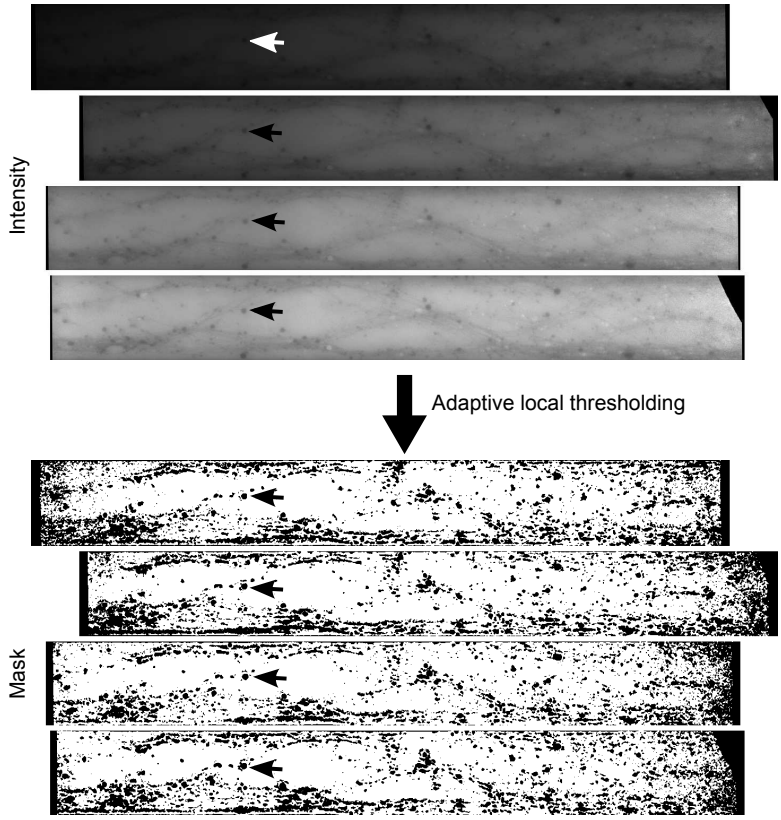

Figure 4.1. The example of masks for intensity analysis. Upper panel: The fluorescence images of a same channel obtained at different time after applying LY in to the right well. The cell tissue inside microchannel formed local low-intensity regions, e.g. the arrowed black spots, which may lead to underestimating the fluorescence concentration. To avoid this, a mask was generated for each fluorescence images to exclude the low intensity regions (the lower panel).

was applied to the fluorescence images to binarize them into masks (figure 4.1). Figure 4.1 shows that the mask can be stably generated, despite of the large variance of the intensities. The median intensities of 10-pixel-wide bins were used to represent the spatial distribution of fluorescence intensity along the microchannel longitudinal axis.

4.3.5 The finite-element-method (FEM) simulation of the diffusion pattern

To understand the diffusion pattern inside microchannel devices, a series of numerical simulation were performed in the COMSOL multiphysics simulation package. The device is modelled in 2 dimensions with the transient diffusion analysis module. Each device contained two 1-mm-wide, 3-mm-high rectangular wells, and a microchannel in between (figure 4.2). The diffusion coefficient was set to 1.37×10^{-9} m^2/s, which is the diffusion coefficient of 4-AP in water at 37°C. The initial concentration in the well,

which the 4-AP was applied to, was set to 1 mM; the initial concentration in the microchannel and the other well was set to 0 mM. After the simulation the results were ported into MATLAB for postprocessing.

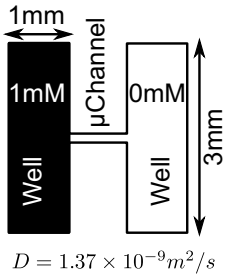

Figure 4.2. The geometry and initial value of FEM models. Each device contained two 1-mm-wide, 3-mm-high rectangular wells, and a microchannel in between. The diffusion coefficient was set to 1.37×10^{-9} m^2/s. The concentration in the left well was set to 1 mM.

4.4 Results

4.4.1 The impact of the soma location, axon length, axon diameter, and ion-channel distribution on the signal waveform

Simulation results (figure 4.3) show that the bigger the axon diameter or the higher the ion-channel density, the larger the recorded signal amplitude will be. The signal is proportional to the amplitude of extracellular current inside the microchannel (chapter 3), which is the integration of all transmembrane current inside a microchannel. The axon with smaller ion-channel density will lead to smaller transmembrane current density, which means smaller transmembrane current. The axon with smaller diameter has smaller membrane area, thus provide less transmembrane current, although the transmembrane current density is the same. Hence, the smaller axon diameter or smaller ion-channel density can result in smaller amplitude.

In the culture, the soma of the neuron projecting axon into the microchannel can be several millimetres away from the channel entrance. To understand the dependence of signal waveforms on the distance (D_{sc}) from the soma to the proximal entrance (the microchannel entrance in soma-well), a series of numerical simulation with different channel position but constant channel geometry and neuronal criteria were performed. Figure 4.4 (a) shows the positive, negative and peak-to-peak amplitudes, and the signal width maintained the same, while D_{sc} is smaller than 0.7 mm. All the amplitudes decrease with increasing D_{sc} beyond ~0.7 mm. In this range, the signal width also

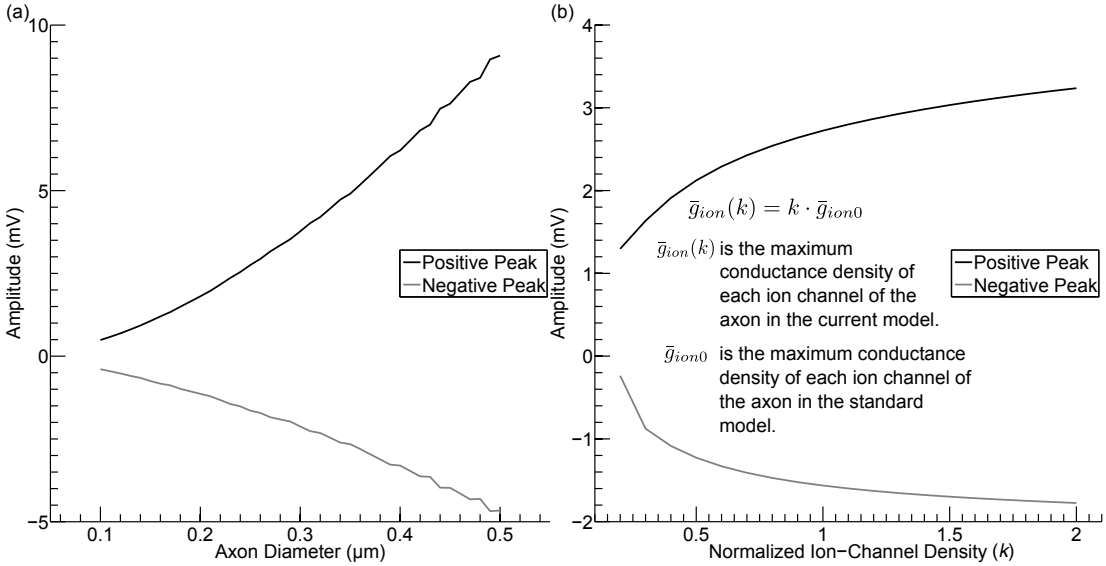

Figure 4.3. (a) The impact of the axon diameter on the recorded signal amplitudes, i.e. positive peak (black solid line), negative peak (grey solid line). In the numerical simulation, the bigger the diameter the larger the absolute value of peak values. (b) The dependence of recorded signal amplitudes on the ion-channel densities, with a constant proportion of the ion-channels.

decreased with increasing D_{sc}. However, the axon can not go through the microchannel, while D_{sc} larger than 0.85 mm. This suggests that the amplitudes rather depend on the length of axons inside the microchannel than the location of the soma.

In our devices, the axons can sprout several millimetres into the soma-well. If the cultures are at different ages or the neurons meet different extracellular matrix or different cellular signals during development in vitro, the axon lengths can have large variance. Severe dependence of the signal waveform on the axon length, which is difficult to determine experimentally, will impair the feasibility of using the device for ion-current screening. As expected, Figure 4.5 (a) shows the amplitudes do not depend on axon length longer than 0.4 mm. The axon shorter than 0.26 mm did not go through microchannel. This suggests the amplitudes do not depend on the axon length either.

Both simulation results suggest that: as long as the axon goes through the entire microchannel there is no dependence of signal waveform on distance from the microchannel to soma, or the length of the axon. But there is a decreasing trend of the signal amplitude, once the length of axon inside the microchannel (L_{in}) is smaller than the length of

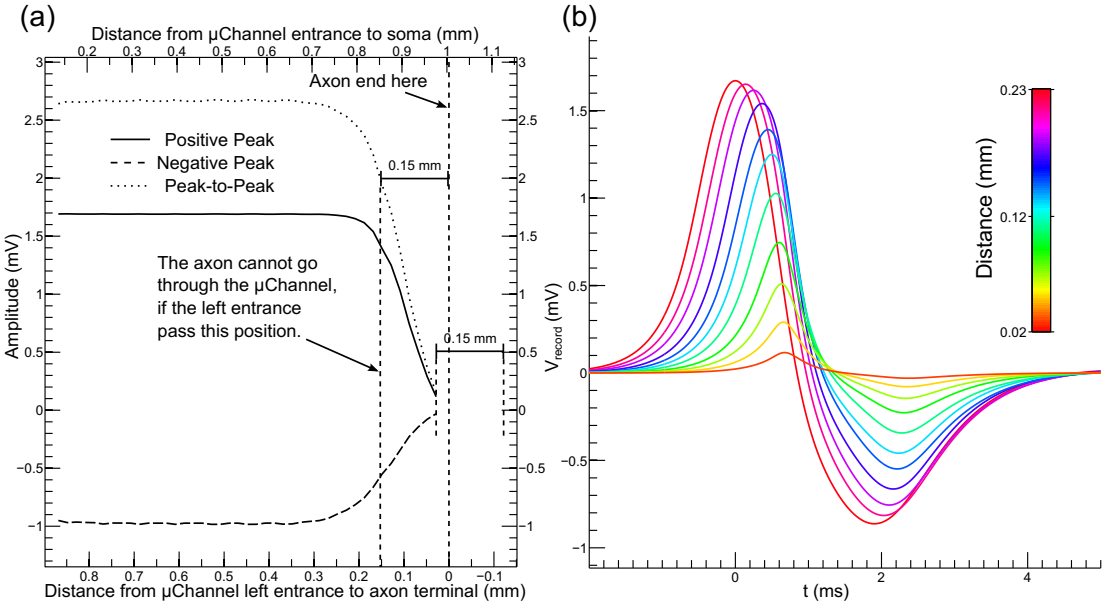

Figure 4.4. The impact of the simulated signal waveform on the soma location. The signal magnitude does not show clear dependence on the distance (D_{sc}) from proximal entrance (the microchannel entrance in soma-well) to the soma, when varying D_{sc} from 0.15 mm to 0.7 mm. After the D_{sc} increasing beyond 0.7 mm, the signal magnitude starts to decrease with the D_{sc} increasing. After the D_{sc} increasing beyond ~0.85 mm, where the axon terminal starts to enter the microchannel, the signal magnitude decreased quickly with the D_{sc} increasing.

microchannel. This might imply that the signal is mainly generated by the transmembrane current of the axon compartments inside the microchannel. Hence, the amount of the membrane outside the microchannel does not affect the signal shape; the ion-channel profile or AP shape outside the microchannel does not affect the signal shape either. Reducing the length of the axon compartment inside the microchannel however leads to reduce the magnitude of the transmembrane current inside channel, which responsible for signal generation. Thus the signal amplitude decreases while the L_{in} decreasing.

Interestingly, the decreasing does not happened exactly at the point where the axon terminal starts to enter the microchannel (Figure 4.4 (a) and 4.5 (a)), but at the point where there is still ~100 μm axon inside the distal-well. This is consistent with the length constant of the axon ($\lambda = \sqrt{\frac{r_m}{(r_i+r_o)}} = 123\mu m$). The length constant determines how far a point source on plasma membrane can affect the cross-membrane potential (V_{cm}) nearby: $V(x) = V_{max}(e^{-x/\lambda})$. If the V_{cm} at the compartment where the point source is inserted is V_0, the V_{cm} at the compartment λ away from the point source is about $0.37 \times V_{cm}$. Therefore, the axon compartments outside the microchannel do affect

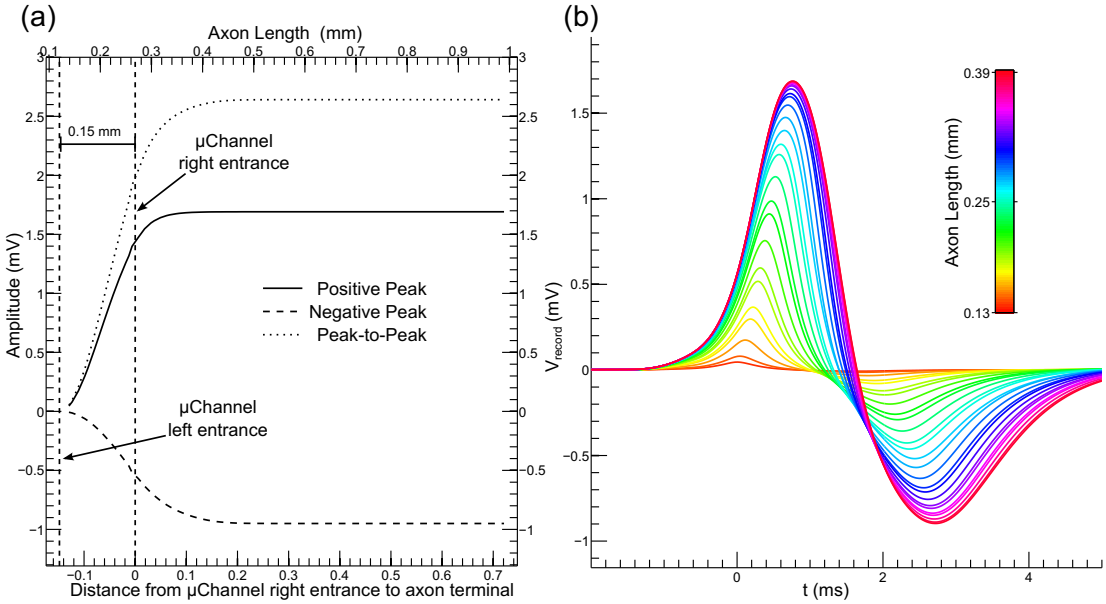

Figure 4.5. The impact of the simulated signal waveform on the axon length. The signal magnitude does not show clear dependence on the axon length, when varying axon length from ∼0.4 mm to 1 mm. The signal magnitude started to decrease with reducing the length of axons shorter than ∼0.4 mm. When the axon shorter than ∼0.26 mm, the length of the axon inside the microchannel (L_{in}) started to decrease. The signal magnitude decreased quickly with the L_{in} decreasing.

the signal generation but the influence fades off exponentially while the distance from the compartment to channel entrance increases.

To further test this hypothesis, a band of compartments containing less fast-delayed-rectifier ion-channels (the $\bar{g}_F$ is set to 1% of normal $\bar{g}_F$) were inserted at different positions in the model. Conceivably, due to this different ion-channel profile, the AP shape and transmembrane current density at these compartments are different from the normal axon compartments. If the low-I_F band located inside microchannel or nearby, the signal will vary accordingly.

Figure 4.6 shows that the simulation result is consistent with this hypothesis. The signal shape starts to vary when the low-I_F band is located at ∼100 μm to channel entrance, and the effect became much stronger when the band is located inside the microchannel (figure 4.6, the circle and square in (a), black and grey solid-line in (b)).

Interestingly, the band near to soma-well (figure 4.6, the square marker in (a), the dashed line in (b)) and the band near to distal-well (figure 4.6, the upward triangle

marker in (a), the dotted line in (b)) have reversed impact on signal shape: the amplitude of negative peak was decreased by the band near to soma-well but increased by the band near to distal-well. If the band located near to the centre of the microchannel, the two effects seem cancel each other (figure 4.6, the diamond marker in (a), the dash-dotted line in (b)).

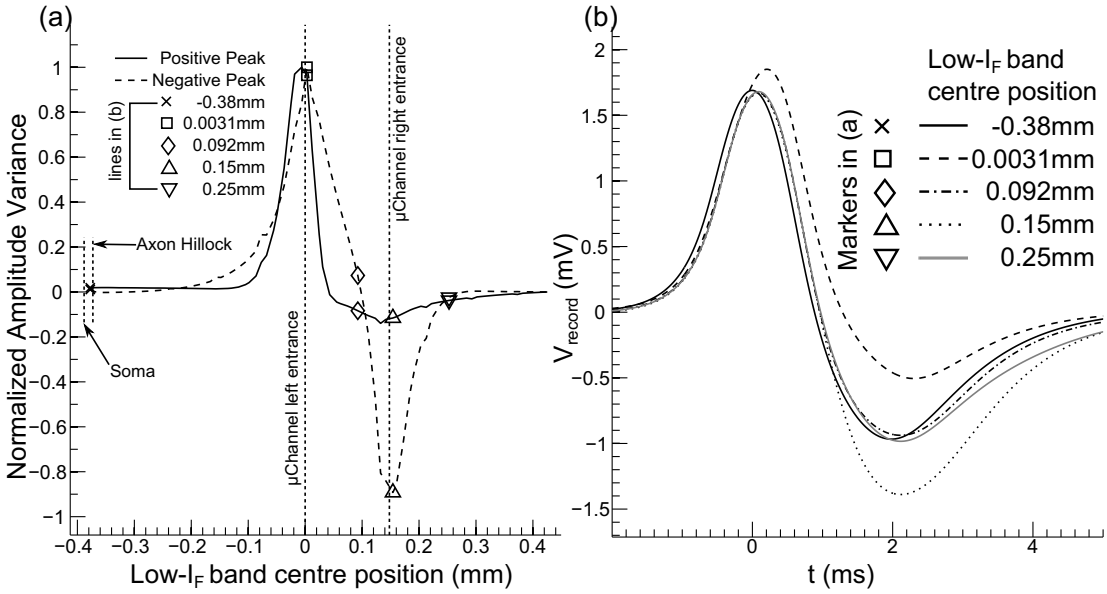

Figure 4.6. The dependence of the simulated signal waveform on the location of low-I_F bands (50-μm-long, is 1% of the normal axonal $\bar{g}_F$, the fast-delayed-rectifier ion-channel density is 1% of that in the normal axon). (a) The impact of the low-I_F band location on signal positive peak value (the solid curve) and negative peak value (the dashed curve). (b) The waveform shape of the signal obtained when low-I_F band centre located at different places: in soma-well far away from the channel entrance (the cross marker in (a), the solid line in (b)), at the proximal entrance of the microchannel (the square marker in (a), the dashed line in (b)), inside the microchannel (the diamond marker in (a), the dash-dotted line in (b)), at the distal entrance of the microchannel (the upward triangle marker in (a), the dotted line in (b)), and inside the distal-well ∼0.2 mm away from the right entrance (the downward triangle marker in (a), the grey solid line in (b)).

Inserted low-I_{Na} compartments affect the signal waveform at the similar position, but has reversed impact on signal waveform (figure 4.7). The low-I_{Na} band near to soma-well largely decreased the positive peak and slightly increased the negative peak. The band near to distal-well shrunk the negative peak.

These simulation results imply: 1. Only the membrane inside the microchannel or within ∼100 μm to channel entrances affect signal waveform; 2. The variation of ion-

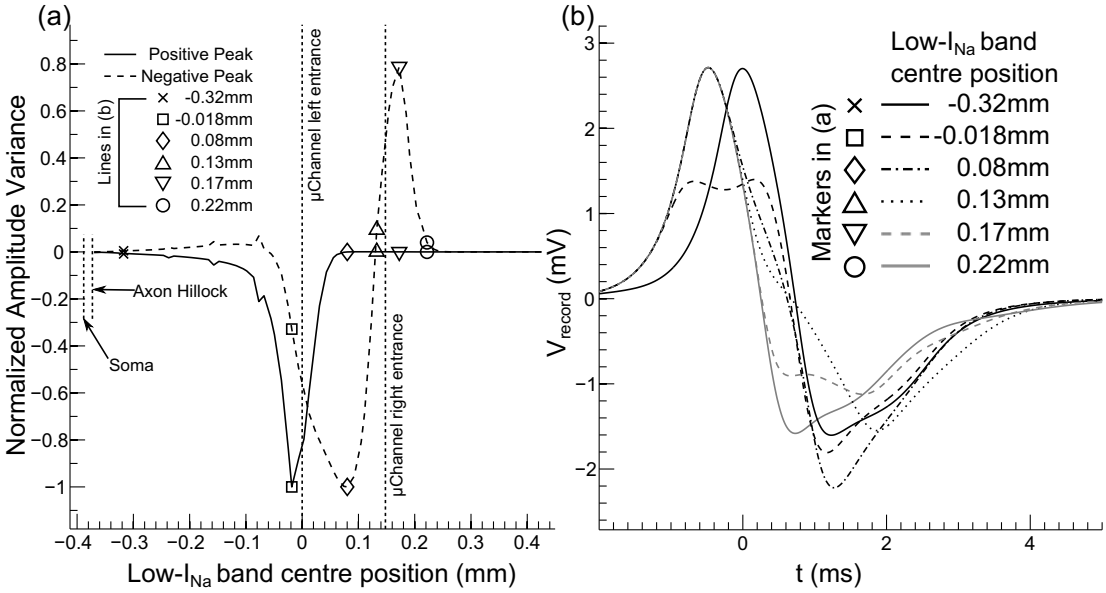

Figure 4.7. The dependence of the simulated signal waveform on the location of low-I_{Na} bands (50-μm-long, is 1% of the normal axonal $\bar{g}_{Na}$, the voltage-dependent ion-channel density is 1% of that in the normal axon). (a) The impact of the low-I_{Na} band location on signal positive peak value (the solid curve) and negative peak value (the dashed curve). (b) The waveform shape of the signal obtained when low-I_{Na} band centre located at different places: in soma-well far away from the proximal entrance (the cross marker in (a), the solid line in (b)), in soma-well near to the proximal entrance (the square marker in (a), the dashed line in (b)), near to the centre of the microchannel (the diamond marker in (a), the dash-dotted line in (b)), inside microchannel near to the distal entrance (the upward triangle marker in (a), the dotted line in (b)), inside the distal-well ∼20 μm away from the distal entrance (the downward triangle marker in (a), the grey dashed line in (b)), and inside the distal-well ∼150 μm away from the distal entrance (the circle marker in (a), the grey solid line in (b)).

current distributions in this detectable region can be represented as variation of the waveform of the recorded signals.

4.4.2 Transport of chemical compounds inside the microchannel

In last section, numerical simulation suggests using ion-channel blocker to modify the ion-current distribution in detectable region may change the signal waveforms. However, the influence on signal waveforms may depends on the spatial distribution of the blocker (figure 4.6 and 4.7). The diffusion and fluid flow inside microchannel may affect the blocker concentration inside microchannel or even in the wells. Hence, in this section, we study the mass transfer inside the microchannel by experiments and numerical simulation.

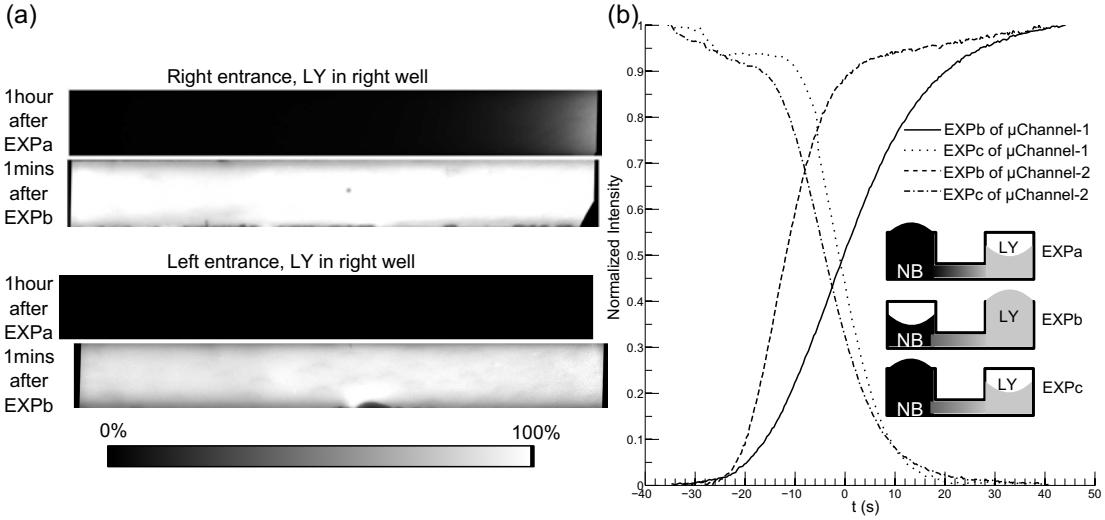

Figure 4.8. The microflow inside microchannels without any cell culture. For each device, there were 3 experiments in series. First, we applied LY in right well but maintained the liquid level the half of that in the left well (EXPa in inset of (b)). Then we increased LY's liquid level and decreased the liquid level of the culture medium (NB) to the half of the LY's (EXPb). At last, we reversed the liquid level again (EXPc). (a) 1 hour after EXPa, there is no detectable fluorescence intensity change in the entire channel. But after the LY's liquid level is higher than NB's, the fluorescence intensity increased ∼3% per second. The fluorescence images showed the final intensities at the both channel ends are similar. (b) The time dependence of the fluorescence intensity in the middle of the channel.

To characterize the flow speed inside microchannel, the fluorescence change due to the flow inside microchannel has been monitored and analyzed. A water-soluble fluorophore, Lucifer yellow (LY), was applied to one of the two wells in our devices. The flow, if there is any, would convey the LY through microchannel into another well. The fluorescence intensity is proportional to the fluorophore concentration, at low concentrations as we used (0.1 mM). Therefore, there is a variation of the fluorescence intensity, before the flow front completely goes through microchannel. In present work, the mean fluorescence intensity of negative control is regarded as 0% and the mean fluorescence intensity of positive control is regarded as 100% (see methods section for details). The variations of fluorescence intensity under 3 different conditions were carried out for each channel (illustrated in the inset of figure 4.8 (b)):

EXPa. ∼200 μL of NB was maintained in the left well, then ∼100 μL 0.1 mM LY was added into empty right well. Thus the left well has higher liquid level than the right well.

EXPb. ∼100 μL of NB was sucked out from left well, at the same time another 100 μL 0.1 mM LY was added into right well. Thus the right well has higher liquid level than

the left well.

EXPc. After the LY completely filled up the microchannel, the liquid level was reversed again.

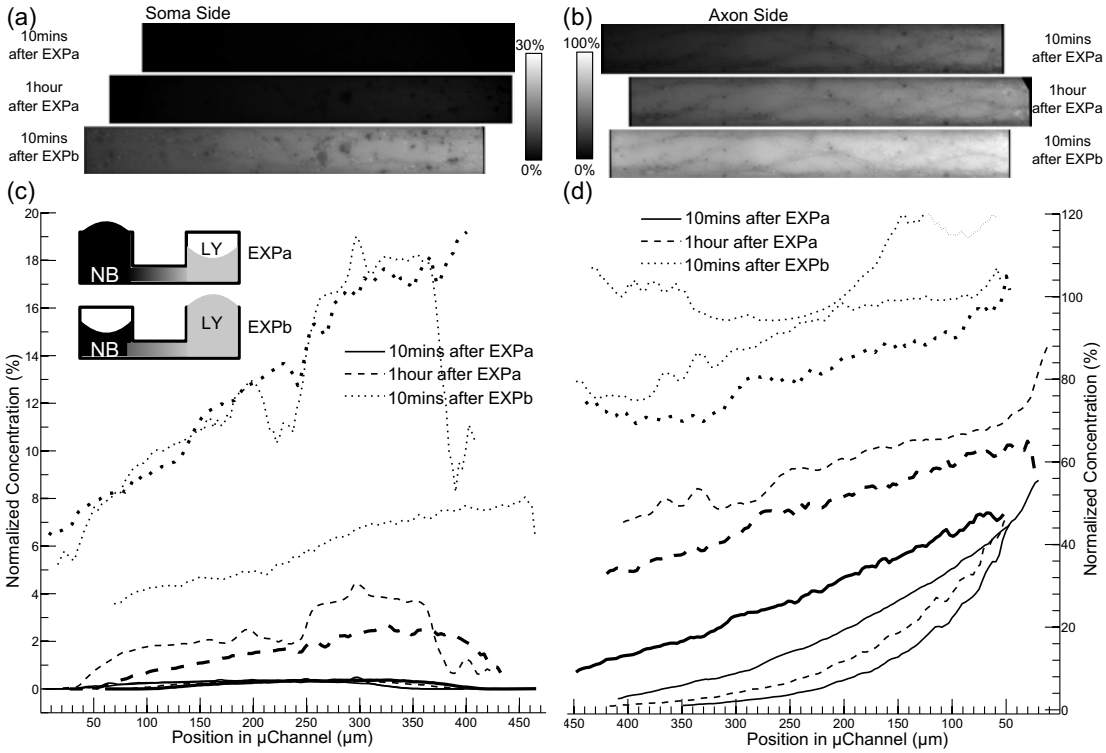

Figure 4.9. The diffusion of LY in microchannel with cell culture in left well at 14DIV. 0.1 mM LY was applied in right well. (a) The fluorescence intensity in a 50-μm-wide, 3.7-μm-high, 1-mm-long microchannel within 0.45 mm of the left entrance. 10 mins after EXPa, there was no detectable fluorescence intensity. 1 hour after EXPa , the fluorescence intensity was still low. 10 mins after EXPb, the intensity was still below 20%, although there was visible intensity gradient. The mean intensity of every 10-μm-wide bin at each time points were plotted as thicker lines in panel (c). (b) The fluorescence intensity in the same microchannel within 0.45 mm of the right entrance. 10 mins after EXPa, there was already visible fluorescence gradient. The mean intensity of every 10-μm-wide bin at each time points were plotted as thicker lines in panel (d). (c-d) The spatial distribution of mean intensity along the longitudinal axis of microchannels at 3 time points: 10 mins after EXPa (solid line), 1 hour after EXPa (dashed line), and 10 mins after EXPb (dotted line). There are 3 channels in total. The distributions in the channel of panel (a-b) were plotted as thicker lines.

In EXPa the pressure is higher in left channel entrance, then there should be a flow from left to right, the LY cannot be transported into microchannel. In EXPb due to reversing the pressure, the flow from right to left can transport LY into the microchannel. In EXPc, the flow from left to right should clear the LY from microchannels.

First, we performed this test on devices without any cell culture (figure 4.8). As expected, in EXPa there is no detectable fluorescence intensity inside microchannel other than the background autofluorescence of NB (figure 4.8 (a)). In EXPb, the fluorescence intensity increased 3% - 4% per second before reaching maximum value. In EXPc, the fluorescence intensity decreased 4% - 5% per second before reaching the autofluorescence level (figure 4.8 (b)).

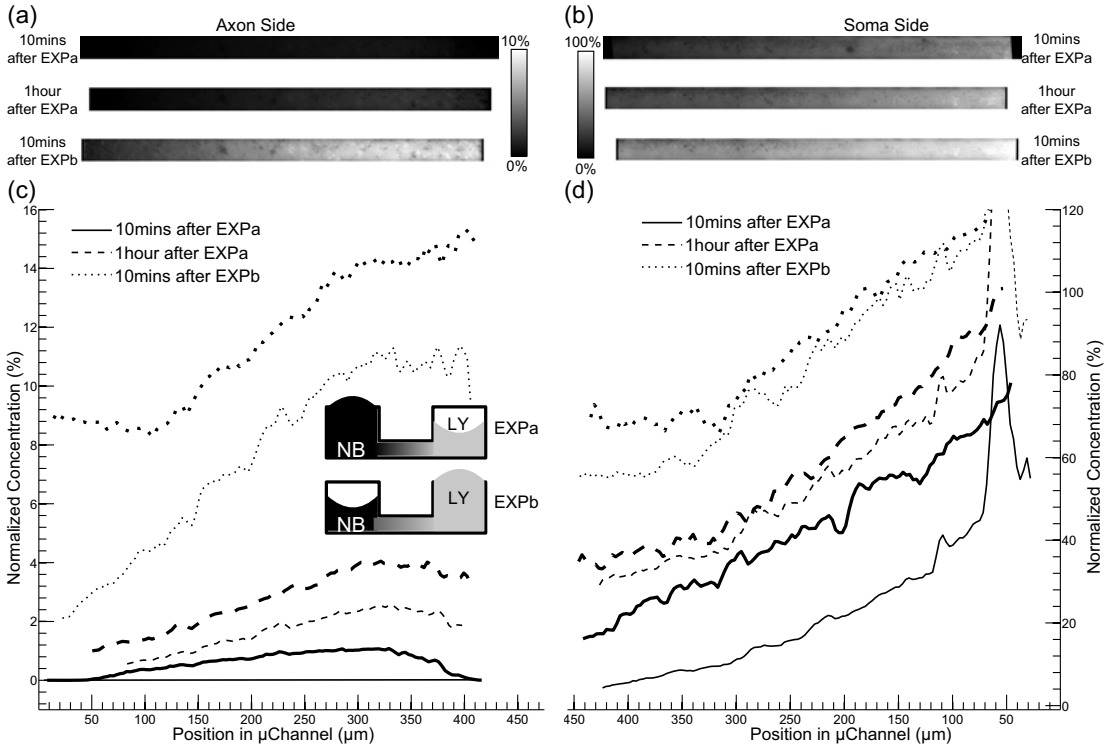

Figure 4.10. The diffusion of LY in microchannel with cell culture in right well at 14DIV. 0.1 mM LY was applied in right well. (a) The fluorescence intensity in a 25-μm-wide, 3.7-μm-high, 1-mm-long microchannel within 0.41 mm of the left entrance. 10 mins after EXPa, there was no detectable fluorescence intensity. 1 hour after EXPa, the fluorescence intensity was still low. 10 mins after EXPb, the intensity was still below 10%, although there is visible intensity gradient. The mean intensity of every 10-μm-wide bin at each time points were plotted as thicker lines in panel (c). (b) The fluorescence intensity in the same microchannel within 0.45 mm of the right entrance. 10 mins after EXPa, there was already visible fluorescence gradient. The mean intensity of every 10-μm-wide bin at each time points were plotted as thicker lines in panel (d). (c-d) The spatial distribution of mean intensity along the longitudinal axis of microchannels at 3 time points: 10 mins after EXPa (solid line), 1 hour after EXPa (dashed line), and 10 mins after EXPb (dotted line). There are 2 channels in total. The distributions in the channel of panel (a-b) were plotted as thicker lines.

Then, we performed this test on devices with cell cultures (figure 4.9 and figure 4.10). Interestingly, the result is very different from that of empty devices. In EXPa, although there is a positive pressure gradient from left to right, the fluorescence intensity still increased slowly inside microchannel. Usually, the intensity stopped increasing after 10-30 mins and maintained the similar value after 1 hour, although the intensity on the left side of microchannels is still at autofluorescence level. In EXPb, the fluorescence intensity increased much slower than in empty devices: after 10 mins the fluorescence intensity on the left entrance was still below 0.1; in contrast, the intensity on the left entrance always reached 1 within 1 min in empty devices.

This implies the spontaneous seal of microchannel not only increase the electrical resistance but also the fluid resistance. The flow speed inside sealed microchannel is so slow that the diffusion becomes the dominated mechanism of the mass transfer, which is not affected by the pressure gradient. The volume (100 µL range) and the cross-section area (square millimetre range) of 6-mm-diameter and 5-mm-high wells are much larger than the volume ($<$ 0.2 nL) and cross-section area ($<$ 200 µm^2) of the microchannel. Hence, the concentration at each end of microchannel can be roughly regarded as constant. The steady-state solution of the diffusion equation is:

$$\begin{cases} \frac{\partial C(x,t)}{\partial t} = D\frac{\partial^2 C(x,t)}{\partial x^2} \\ C(x,0) = 0,\ x > 0 \\ C(0,t) = C_0 \\ C(L,t) = 0 \end{cases} \Rightarrow C(x) = C_0 \times (1 - \frac{x}{L}) \tag{4.1}$$

$C(x,t)$ is the longitudinal distribution of chemical compound concentration inside the microchannel. D is the diffusion coefficient.

The steady-state concentration decreases linearly from C_0 at the right entrance to 0 the left channel entrance, which is consistent with the fluorescence-intensity distribution in EXPa with cell cultures, at 1 hour after adding LY. The diffusion coefficient of LY is about 1.4×10^{-10} m^2/s at 25°C, theoretically, it will take ∼30 mins to reach the steady state when L = 1 mm, which is also consistent with the result of EXPa with cell cultures. The potassium-channel blocker (4-AP) used in this paper has a much larger diffusion coefficient of 1.37×10^{-9} m^2/s at 37°C. It can reach the steady-state much faster (in several minutes) than LY in the microchannel with the same length.

To further investigate the diffusion behaviour of the potassium-channel blocker (4-AP) used in this paper, a series of 2D FEM simulation were performed. The cell tissue can reduce the effective cross-section area (A_E) of a microchannel by clogging it (spontaneous seal). Then a partially clogged microchannel can be modelled as a thin channel with smaller cross-section (A_E) concatenated with thicker channel with normal cross-section(A_0). Assuming that only the gap between cell tissue, filled with culture medium, acts like electrical path and diffusion path, then the ratio of A_E to A_0 can be estimated from the electrical-resistance of unclogged channel (R_{pre}) to that of the full clogged channel (R_{post}): $\frac{A_E}{A_0} = \frac{R_{pre}}{R_{post}}$, which is around 0.15 to 0.5 (chapter 3).

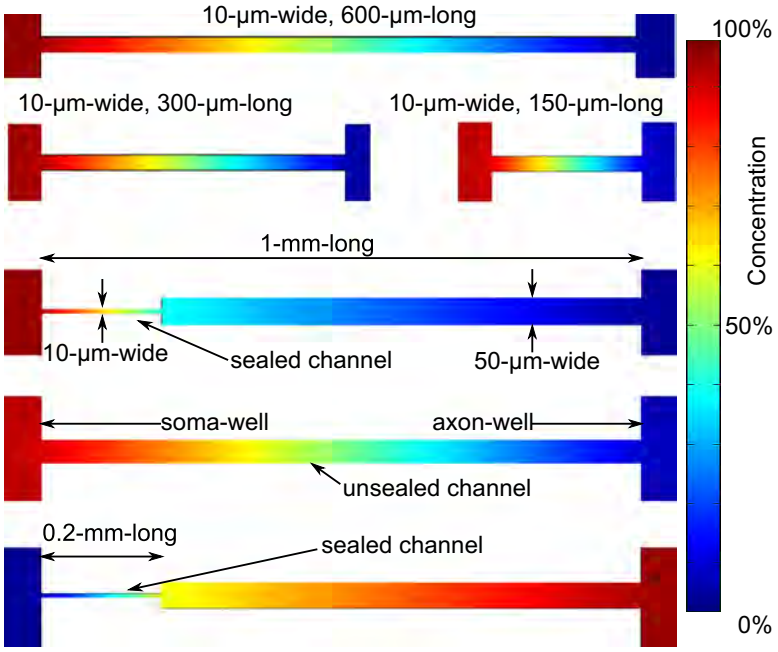

Figure 4.11. The FEM simulated concentration distribution of 4-AP in microchannel devices at 1 hour after EXPa. The wells were cropped to fit into the figure. The sealed channels were modelled as channel segments 5 times smaller in width than unsealed segments. The concentration in the well near to channel entrance varied along the time. The concentration in the well which the 4-AP applied is larger than 90%, the concentration in another well is smaller than 10%. The distributions are different between partially clogged channels and fully clogged channels. In partially clogged channels, the distributions are also different between applying 4-AP in distal-well and in soma-well.

The full clogged channel is actually degenerated into a simple channel with constant cross-section A_E, which should have the same dynamic behaviour as the unclogged channel. In the partially clogged model however, the mass transfer in big segment limited by the segment with smaller cross-section. This can lead to very different concentration

distribution. (figure 4.11)

Figure 4.12 (a) shows, the concentration reaches steady-state within 20 seconds, in channel shorter than 300 μm. The longer the channel the longer the time it needs to reach the steady-state.

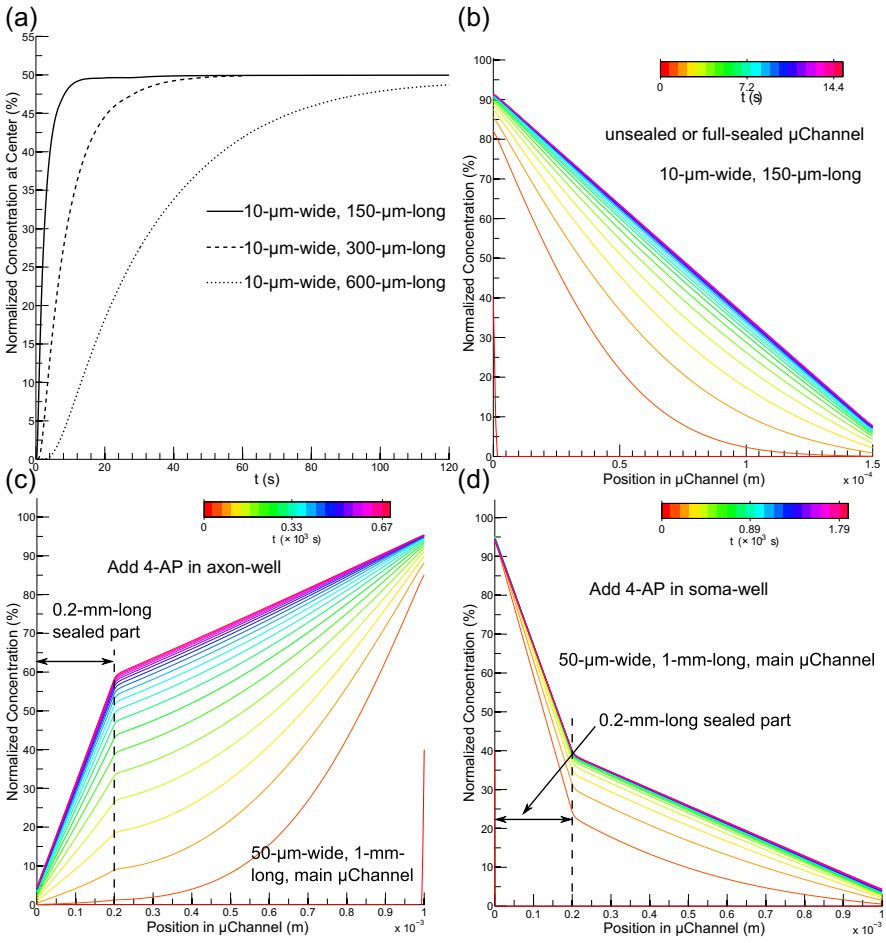

Figure 4.12. The time dependence of the concentration distribution in microchannels. (a-b) The concentration distribution in fully clogged microchannels. The time required to reach the maximum concentration depends on the channel length (a). After ∼10 seconds, the concentration distribution reached steady state, which is a linear distribution (b). (c-d) The concentration distribution in partially clogged microchannels. The steady states of the spatial distributions are segmented lines. Applying 4-AP in axon-well resulted in a higher concentration inside the microchannel than applying it in soma-well.

Figure 4.12 (b) shows the final concentration has linear distribution in full-clogged or unclogged channel. As expected, the partial clogged channel has different concentration

distribution: a segmented-linear distribution (figure 4.12 (c-d)). Interestingly, adding 4-AP in clogged side (figure 4.12 (c)) and in unclogged side (figure 4.12 (d)) also result in different distributions.

Previously, we found the spontaneous seal usually do not extend more than 200 µm into the microchannel. Thus, to describe the concentration distribution in the microchannel shorter than 200 µm, we use the full-sealed/unsealed model:
$C_{4-AP}(x) = C_0 \times 0.95 - 0.9\frac{x}{L}$. C_{4-AP} is the longitudinal distribution of 4-AP concentration; C_0 is the 4-AP concentration in the culture well; L is the microchannel length; x is the distance from interested position to the microchannel entrance located inside the well which the 4-AP is applied to.

4.4.3 Impact of 4-AP on signal waveform

Results of previous compartment simulations imply there is reversed influence on signal waveform of the low-I_F band near to soma-well and near to distal-well. The spontaneous seal can block the fluid flow inside microchannel, acting like a chemical barrier. Hence, adding 4-AP in soma-well may mainly block the I_F in soma-well and shrink the negative peak; adding 4-AP in distal-well may magnify the negative peak.

Having C_{4-AP} spatial distribution model allows us to simulate this situation. Figure 4.13 shows the result consistent with the hypothesis, the negative peak gradually disappeared while C_{4-AP} increasing in soma-well, but it increased while C_{4-AP} increasing in distal-well. Interestingly, when C_{4-AP} is high in soma-well, the simulation predicted that the secondary peak, the negative peak in normal condition, may become positive (figure 4.13 (a)).

To further verify this hypothesis, 4-AP with final concentration of 0.3 mM is applied to real devices with neuronal culture at 14 DIV. The results (figure 4.14) are highly consistent with simulations. 5 mins after applying 4-AP in distal-well, all the spike units developed larger negative peaks than control condition as expected (figure 4.14 (a-e)). Applying 4-AP in soma-well results in generating a secondary positive peak, which is even more significant than the simulation (figure 4.14 (f)).

Figure 4.15 shows the time dependence of the signal waveform after applying 4-AP in soma-well. The signal waveforms do not have any clear variation after 120 seconds, which imply that the C_{4-AP} reaches steady state within 120 s. This is much longer

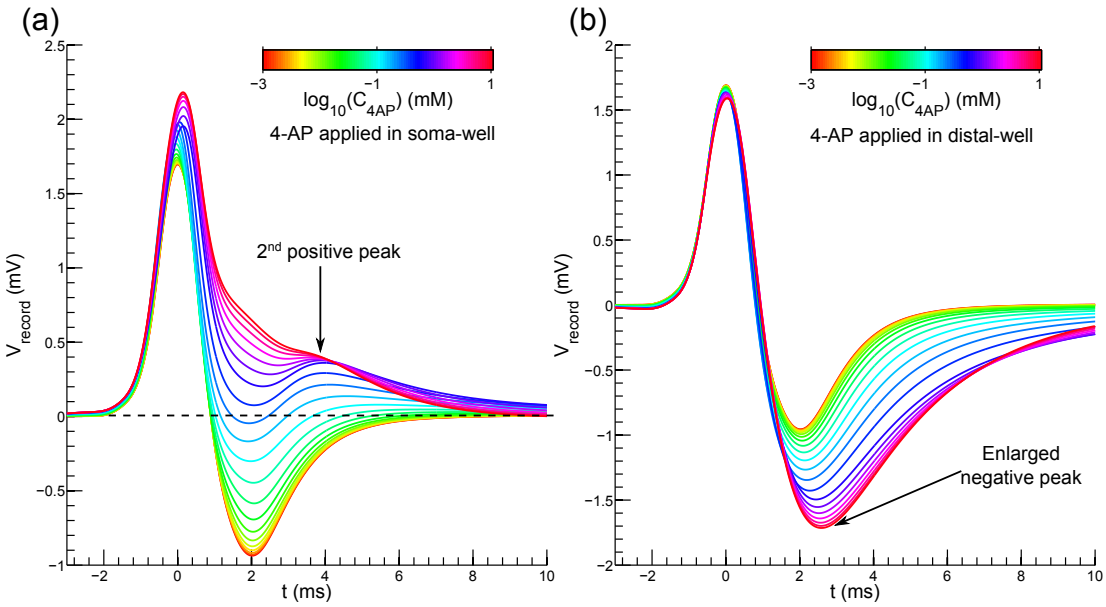

Figure 4.13. Simulated 4-AP effect on the signal waveform. (a) The simulation predicted that 4-AP applied in soma-well may eliminate the negative peak. The higher the concentration the stronger the effect will be. Interestingly, a 4-AP concentration higher than 0.1 mM may induce a secondary positive peak. (b) 4-AP applied in distal-well may enlarge the negative peak.

than the amount of the time which simulated diffusion process needs to reach steady-state concentration. It might due to the much more complicate diffusion condition in reality. The 4-AP might need more time to diffuse through the glial carpet to reach the axon membrane. To make sure that C_{4-AP} always reaches steady-state at the axon membrane, All data in flowing sections were obtained at least 5 mins after applying 4-AP into culture.

4.4.4 The dosage response of signal waveform on C_{4-AP}

In ion channel screening, the dosage response of ion currents on different chemical compounds is important for distinguishing the ion-channel subtypes or determining the specificity of a blockade. We plotted (data not shown) several criteria (negative peak value, peak-to-peak value, the ratio of negative to positive peak value, and the area) of the waveform against the C_{4-AP} and find out the area of the waveform is the most proper criterion to determine the dosage response. The blocking effect is estimated by formula: $\begin{cases} A = \int V_{recorded}\,\mathrm{d}t \\ y = \frac{A_0 - A_c}{A_0 - A_{cMax}} \end{cases}$, where A is the integration of recorded signal waveform over time; A_0 is the A when no blockade is applied to the culture; A_c is the A when

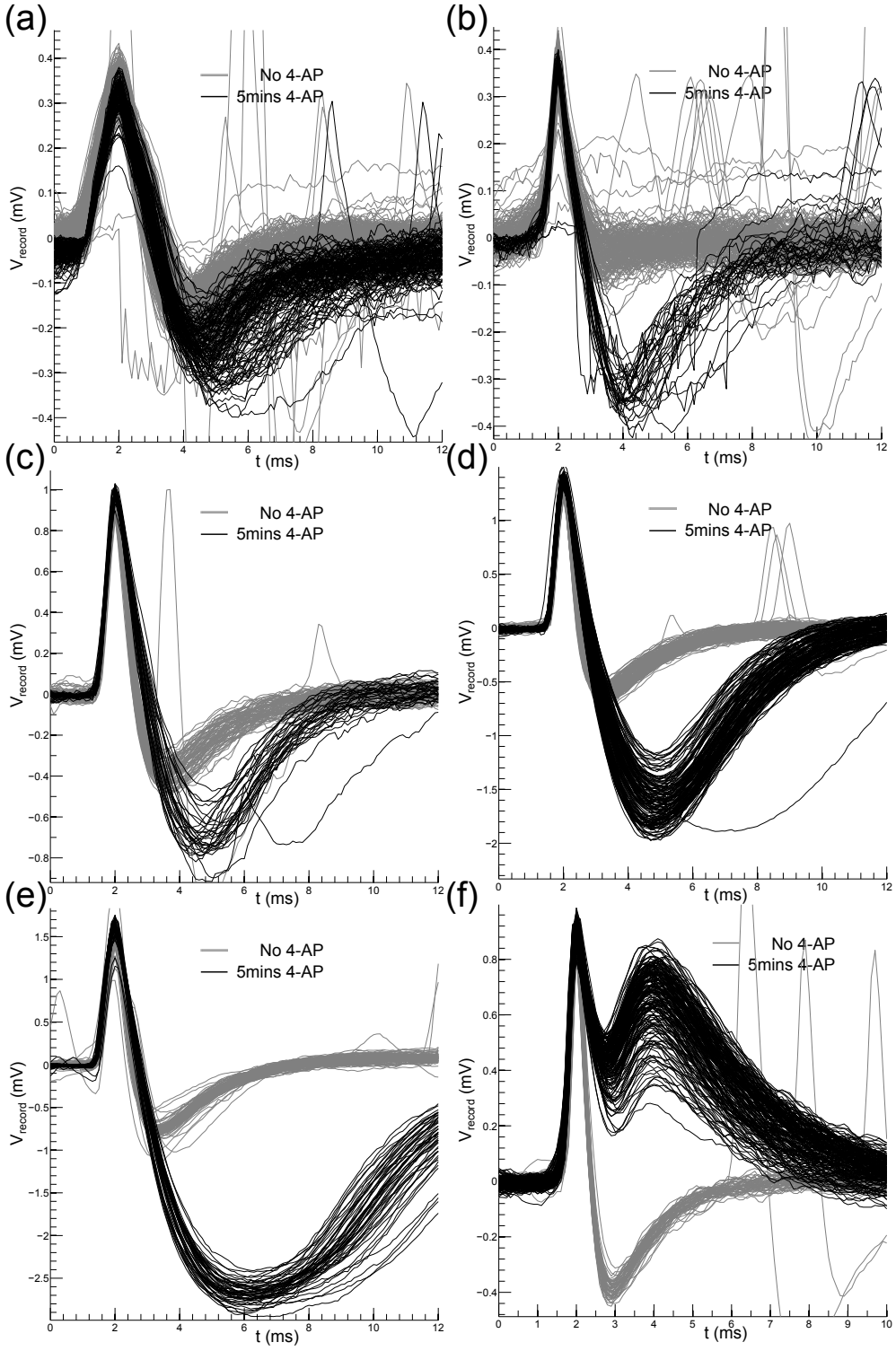

Figure 4.14. The 4-AP affected the signal waveforms recorded from hippocampal cultures. (a-e) All units recorded by a 1-μm-high, 3-μm-wide, 178-μm-long microchannel, before (grey) and 5 mins after (black) applying 0.3 mM 4-AP in its distal-well. (f) The only unit recorded by a 2-μm-high, 4-μm-wide, 115-μm-long microchannel, before (grey) and 5 mins after (black) applying 0.3 mM 4-AP in its soma-well.

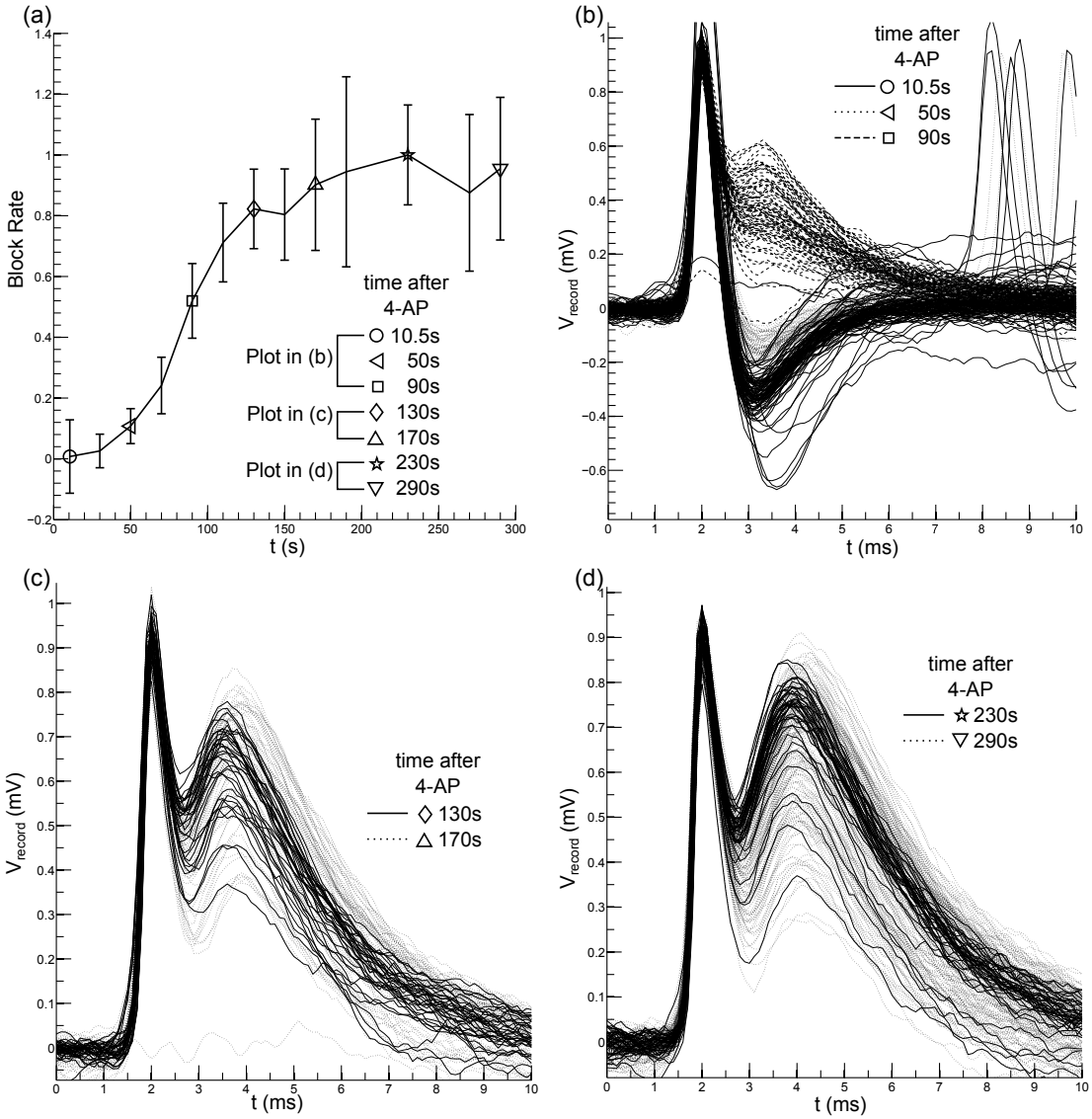

Figure 4.15. The time dependence of the 4-AP effect on the signal waveform recorded by the 2-μm-high, 4-μm-wide, 115-μm-long microchannel. 4-AP was applied into the soma-well. The block effect increased along the time and reached the maximum value after ∼120 s. (b-d) The signal waveforms at 7 different time points (markers in (a)). There was a clear development of the secondary positive peak along the time, from 10 s to 90 s after applying 4-AP. The signal waveform did not show clear variation from 130 s to 290 s after applying 4-AP.

the blockade concentration is c; A_{cMax} is the A when the blockade concentration is the highest; y is the resulted blocking effect.

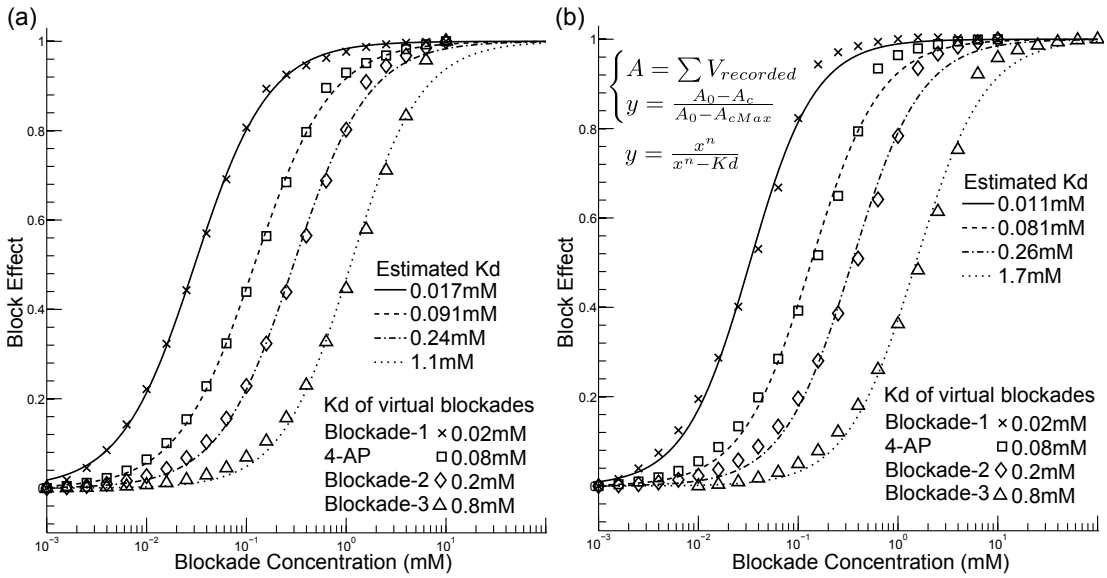

Figure 4.16. The simulated dosage response of 4 virtual blockades, which had different apparent dissociation constant (Kd). The variation of the integration of the signal waveform (A) was used as the criterion to calculate the block effect (y). Then the y was used to estimate the Hill equation parameter Kd (n = 1). (a) The blockades were applied in soma-well. (b) The blockades were applied in distal-well.

Then, the blocking effect is fitted to Hill equation: $y = \frac{c^n}{c^n - Kd}$ to determine the Kd, where c is the blockade concentration; y is the blocking effect. Figure 4.16 shows the simulated results provide a Kd of 0.017 mM for virtual blockade-1 (Kd = 0.02 mM), a Kd of 0.091 for virtual 4-AP (Kd = 0.08 mM), a Kd of 0.24 mM for virtual blockade-2 (Kd = 0.2 mM) and a Kd of 1.1 mM for virtual blocade-3 (Kd = 0.8 mM). Although there is a systematic error of Kd, the result may already good enough for the fast screening.

An IC50 around 0.03 mM (goodness of fit: $R^2 = 0.94$) were obtained from the experimental data with 4-AP in soma-well (figure 4.17), which is in the range of reported IC50 of 4-AP-sensitive ion current (0.024-0.1 mM) [161, 162].

4.4.5 Determining the conduction velocity of axon

Conduction velocity (CV) is useful for studying axon development and demyelination/remyelination or provides information about the axon diameters of recording neu-

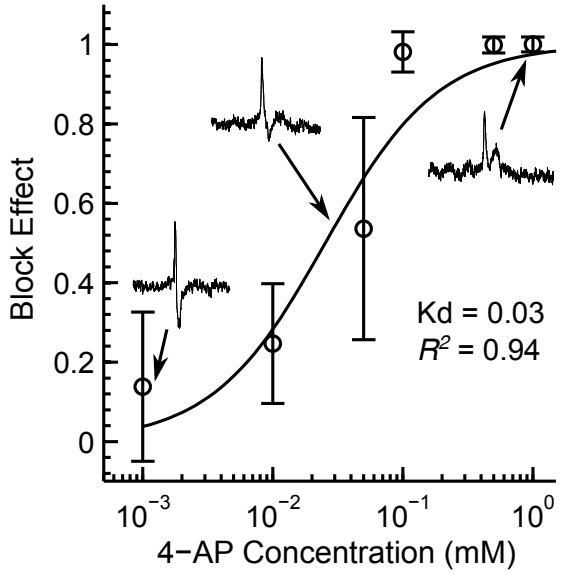

Figure 4.17. The dosage response of 4-AP on signal waveforms. 4-AP were applied in soma-well. The insets show the typical signal waveforms.

rons. MEA combined with microchannel can record extracellular signal from multiple sites along the axons. Intuitively, the delay of positive peak of each extracellular waveform may represent the delay of AP at each recording site.

However, the intrachannel signal is actually related to the integration of the transmembrane current inside the microchannel. Thus the delay of positive peaks of extracellular waveforms is going to highly overestimated the CV (figure 4.18 (a)). The numerical simulation shows delay of longitudinal-extracellular-current waveform (LEC) is tightly correlated to the AP propagation (figure 4.18 (b)). The normalized LEC shape can be easily estimated from the differential voltage between intrachannel electrodes: Normalized $I_i = \frac{\Delta V(t)_i}{max(\Delta V(t)_i)}$. $\Delta V(t)_i$ is the differential voltage between $(i-1)$th and ith electrodes ($\Delta V(t)_i = V(t)_i - V(t)_{i-1}$).

Figure 4.19 (b, d) shows the normalized LEC waveforms of all units (2 units in total) obtained from a 10-µm-wide, 2-µm-high and 1-mm-long microchannel. The CV was estimated via dividing offsets between electrodes by the delays of I_i. The mean CVs of these two units were 306 mm/s and 309 mm/s. From 3 different MEAs we obtained an average CV of 0.3509 m/s (0.2-0.5 m/s, N = 10, STD = 0.1) which is close to the reported CV of pyramidal axons in hippocampal slice (0.3-0.4 m/s from [129]).

4. MICROCHANNEL ENHANCED ELECTROPHYSIOLOGY PLATFORM FOR FUNCTIONAL ION-CHANNEL PROFILING ON AXON COMPARTMENT

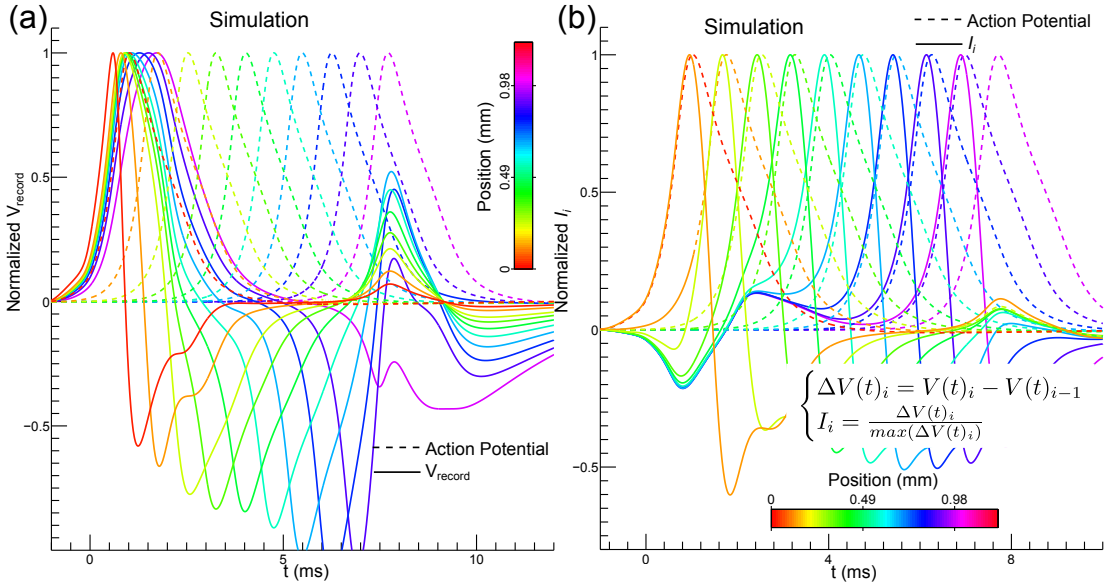

Figure 4.18. (a) The simulation result shows that the delay of cross-membrane action potential (AP) and the delay of the recorded signal waveform by intra-channel electrodes are quite different. (b) The delay of the differential-signal (I_i) waveform between electrodes was the same as the delay of APs.

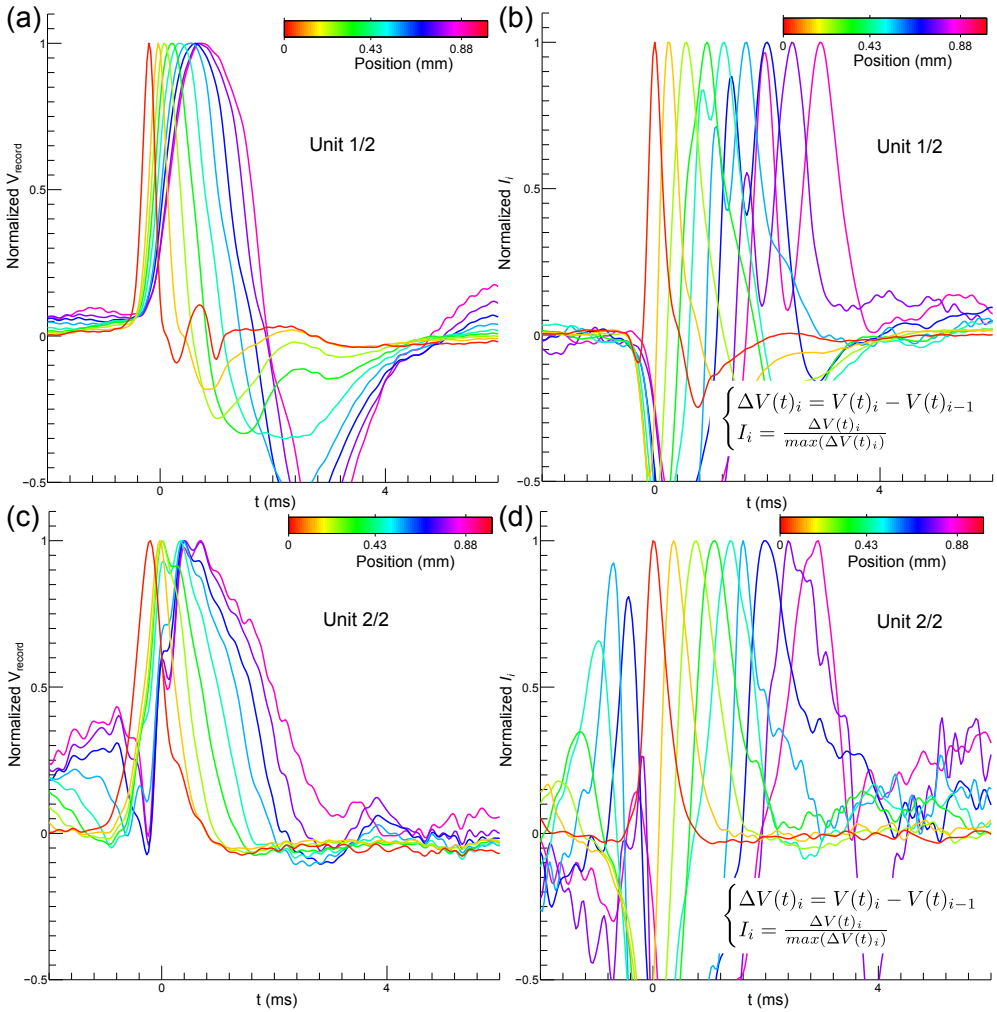

Figure 4.19. (a, c) The recorded signal waveforms by micro-electrodes of a MEA inside a 2-μm-high, 10-μm-wide, 1-mm-long microchannel. In total, two units were identified (unit 1/2 and unit 2/2). (b, d) The differential-signal (I_i) between electrodes. The conduction velocity ($\sim$0.3 mm/s) was estimated via dividing offsets between electrodes by the delays of I_i.

4.5 Discussion and conclusions

The present study provides a detailed investigation of the dependence of the signal waveform recorded in microchannel on biological criteria of cultured neurons. These data reveal that the distance from soma to microchannel entrance and axon length do not affect the signal waveform as long as the length of the axon segment in distal-well are longer than (100 µm), if the axon diameter and ion channel profile are constants. The ion channel profile of the compartments far away ($>$ 100 µm) from the microchannel does not affect the signal waveform either. The signal waveform in our devices strongly depends only on the biological criteria of the axon compartments inside the microchannel. The axon segments outside the microchannel but located within 100 µm of microchannel entrance can also affect the signal waveform.

This result suggests that the ion channel profiles obtained in our devices are rather exclusively of axon compartments than mixed with somata or dendrites. The present study also investigates the chemical compound transfer inside microchannel. These data imply the cell tissue will spontaneously seal up the microchannel leading to block the microflow inside the microchannel. It allows researchers applying chemical compounds exclusively at axon compartments. Finally, we demonstrated a way to obtain the dosage response curve of 4-AP sensitive current and a way to determine the conduction velocity of axons.

4.5.1 Origin of the V_{rec}

During AP propagation, the transmembrane current (I_{cm}, the black arrows, the bigger the black arrow, the stronger the current) varied along the time and position. When the AP propagates into the microchannel, I_{cm} of the membrane patch at the channel entrance will first flow inwardly (positive in figure 4.20 (b) figure 4.21 (c)) due to voltage-dependent sodium channel (Nav) opening. After Na^+ channel inactivation, I_{cm} will flow outwardly (negative in figure 4.20(b), figure 4.21 (a)) due to inward K^+ currents.

At time point 1 (figure 4.20 solid black line), the I_{cm} starts to cause a leftward longitudinal extracellular current (I_{ex}, figure 4.20 (c), grey arrows in figure 4.21), which leads to a positive voltage (V_{rec}) on the recording electrode (figure 4.20 (a) figure 4.21 (b)). The more Na^+ channels opened, the stronger the inward I_{cm} will become, the stronger the I_{ex}, the higher the V_{rec}.

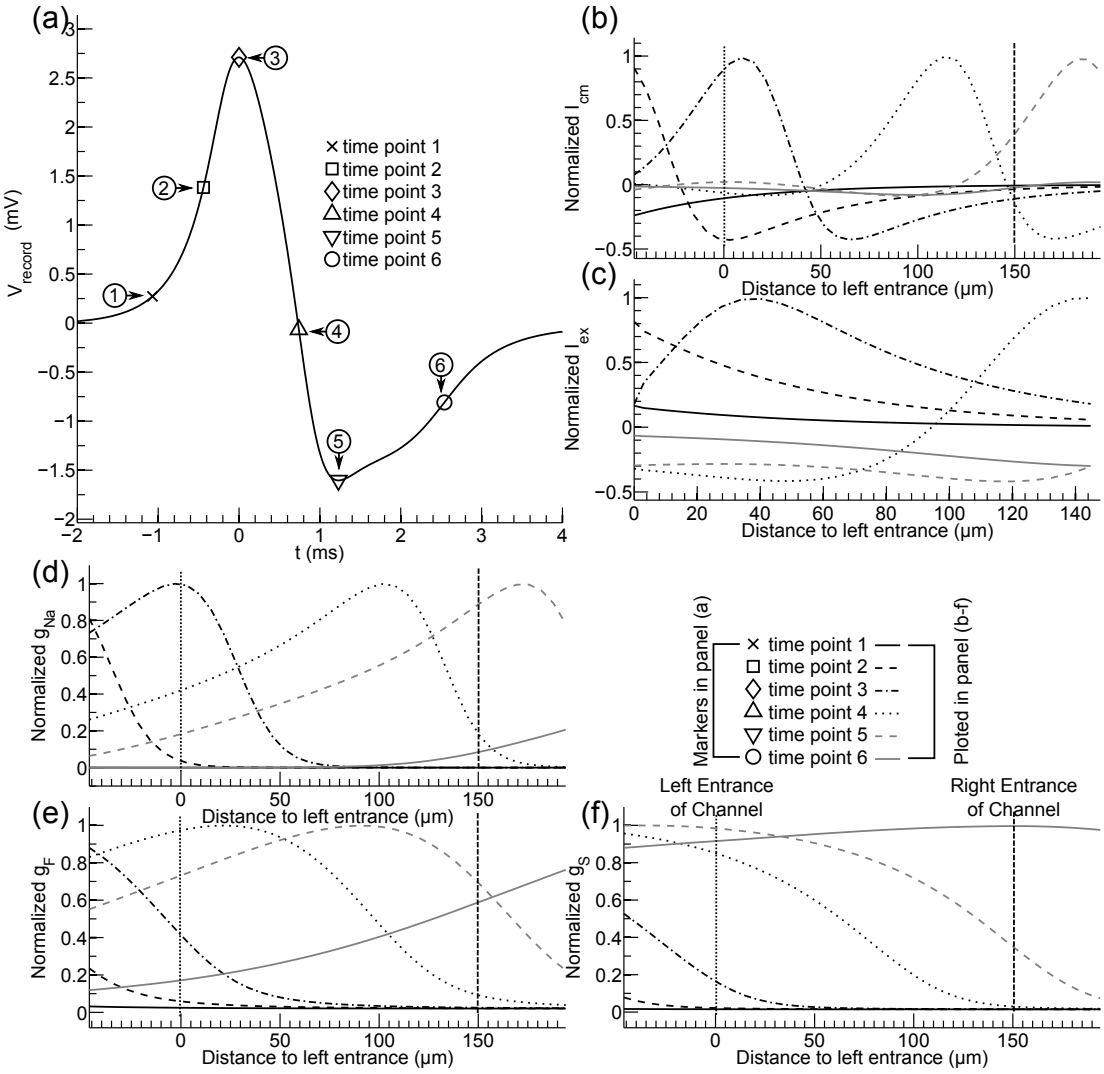

Figure 4.20. The origin of the signal waveform I. The spatial distribution of transmembrane current (I_{cm}, inward is positive), longitudinal extracellular current (I_{ex}, leftward is positive), the conductance densities of voltage-dependent sodium channels (g_{Na}), fast-delayed-rectifier potassium channels (g_F), and slow-delayed-rectifier potassium channels (g_S), at 6 different time points. Vertical dashed line marked the right entrance. Vertical dotted line marked the left entrance.

At time point 2 (figure 4.20 black dashed line, figure 4.21 (c)), the inward I_{cm} at the channel entrance reaches its maximum value, and the Na^+ channels inside microchannel near to the channel entrance also start to open, leading to stronger I_{ex}.

At time point 3 (figure 4.20 black dash-dotted line, figure 4.21 (d)), due to the fast-delayed-rectifier channel (K_F) opening, as well as the Nav inactivation, the I_{cm} outside the microchannel, near to the proximal entrance starts to flow outwardly, resulting in negative-phase of I_{ex} entering the microchannel. Thus, I_{ex} can not increase further, resulting in V_{rec} reaching its positive peak (diamond marker in figure 4.20 (a)).

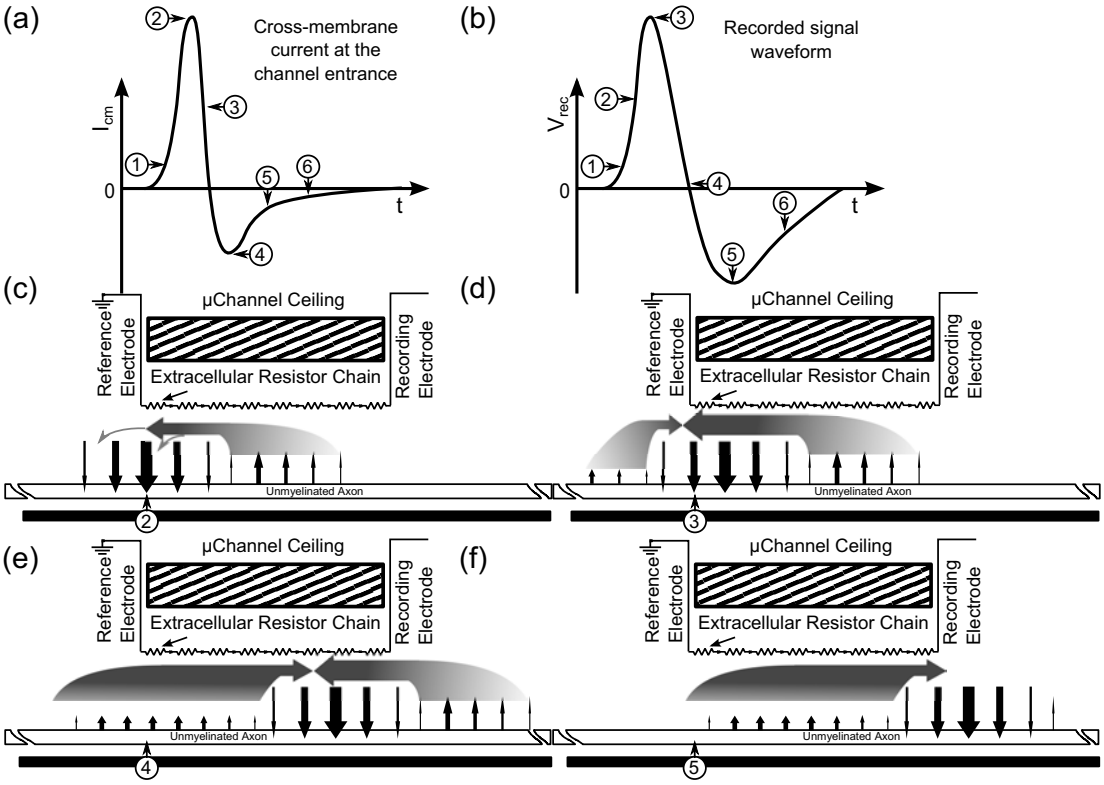

Figure 4.21. The origin of the signal waveform II. This scheme illustrated the relationship among the transmembrane current (I_{cm}, vertical black arrows), the extracellular current (I_{ex}, horizontal grey arrows) and the recorded signal waveform V_{rec}.

At time point 4 (figure 4.20 black dotted line, figure 4.21 (e)), due to voltage-dependent potassium channels (Kvs) at the compartments located in proximal (left) arm of microchannel fully opening, the I_{cm} at proximal (left) arm of microchannel flows outwardly. Thus the negative phase of I_{ex} completely cancels out the positive phase of

I_{ex}, resulting in V_{rec} dropping to zero. As time goes by, more Kvs and less Navs open inside microchannel, producing a negative V_{rec} at the recording electrode.

At time point 5 (figure 4.20 grey dashed line, figure 4.21 (f)), due to the activation of most Kvs at the compartments located in distal (right) arm of microchannel, the I_{cm} at all the compartments inside microchannel flows outwardly. The membrane potential located at proximal (left) entrance almost return to the resting potential. This largely reduces the potassium driven potential eliminating the outward I_{cm} at the proximal (left) entrance, although 80% of K_F channel remains opening. Therefore the absolute value of I_{ex} cannot increase further, causing a negative peak of V_{rec}.

At time point 6 (figure 4.20 gray solid line), most of the K^+ channels entering inactivation state reduces the outward I_{cm} and then reduces the absolute value of V_{rec}. Hence the positive peak of V_{rec} is resulted from the Nav activation, the negative peak of V_{rec} is resulted from the Kv activation.

4.5.2 The differential effects of applying channel blocker at different compartments

Applying 4-AP in soma-well can eliminate the negative peak of V_{rec} which caused by the K^+ outflow. Interestingly applying 4-AP in distal-well results in reversed effect: enlarging the negative peak. Figure 4.22 shows the difference of simulated spatial distribution of ion channel conductances (g_{Na}, g_F, g_S), transmembrane currents (I_{cm}) and longitudinal extracellular current (I_{ex}) between normal condition, applying 4-AP in soma-well and applying 4-AP in distal-well.

After applying 4-AP in the distal-well (dash-dotted line in figure 4.22; figure 4.23 (a-e)), most of the K^+ channels inside microchannel and distal-well were blocked. Thus, at time point B (figure 4.22 (f), figure 4.23 (d)), most of the compartments inside the microchannel or near to the proximal (left) entrance still remain a very high membrane potential, attributed to the prolonged inward ion current caused by blocking K_F channels. However, the compartments near to the proximal entrance has a normal density of functional K_F channels (figure 4.22). This results in a enlarged and prolonged K^+ outflow at the compartments in soma-well near to the proximal entrance, which results in enlarged and prolonged rightward I_{ex} and the enlarged negative peak of V_{rec}.

On contrarily, there is no outward current at the proximal entrance (left entrance) when AP propagating through microchannel, after applying 4-AP inside the soma-

4. MICROCHANNEL ENHANCED ELECTROPHYSIOLOGY PLATFORM FOR FUNCTIONAL ION-CHANNEL PROFILING ON AXON COMPARTMENT

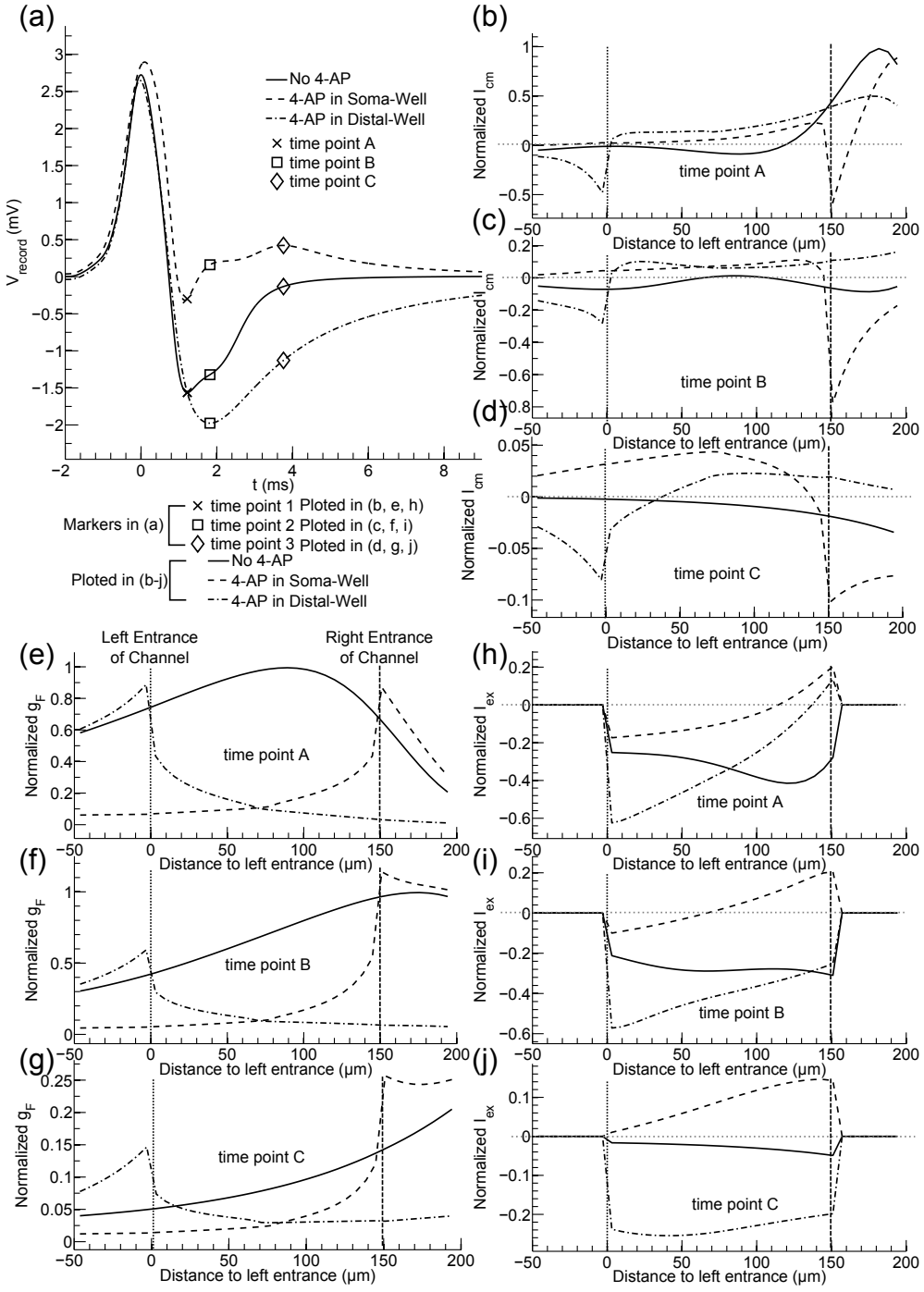

Figure 4.22. The origin of the signal-waveform variation caused by 4-AP I. The spatial distribution of transmembrane current (I_{cm}, inward is positive), longitudinal extracellular current (I_{ex}, leftward is positive), fast-delayed-rectifier potassium channels (g_F), at 3 different time points. The values of each parameter from 3 different conditions were compared: normal model without 4-AP, applying 4-AP in soma-well (dashed line), and applying 4-AP in distal-well (dash-dotted line). Vertical dashed line marked the distal entrance (left entrance). Vertical dotted line marked the proximal entrance (left entrance).

well (dashed line in figure 4.22; figure 4.23 (l-p)). The inactivation of Na^+ channels can reduce the V_{rec} to zero, but cannot form the normal negative peak. The normal V_{rec} density of functional K_F channels at the compartments near to the distal (right) entrance allows a big outward I_{cm} near to the distal entrance, causing a leftward I_{ex}. The leftward I_{ex} leads to a positive voltage on recording electrodes. At time point C, this leftward I_{ex} reaches its maximum value, forming a 2^{nd} positive peak.

4.5.3 On how the device distinguishes signals from different neurons

The signal is generated by the transmembrane current of the axon compartments inside the microchannel and within ∼100 μm of the channel entrances (the exact range depends on the conduction velocity of axons (CV)). Hence the soma distance to the channel entrance will not affect the signal waveform. There are several intrinsic criteria of axons do have significant impact on the signal waveform: the axon diameter, the axonal ion channel profile (ion-channel types, the proportion of the ion channels, the density of the ion channels) and myelination.

When the ion-channel profile is exactly the same, the transmembrane current density is constant in axons with different diameters. Then the transmembrane current strength is proportional to the membrane area per length of the axon. Thus, the bigger the axon diameter, the larger the membrane area per length, the higher the transmemebrane current strength, the larger the amplitudes.

The inward transmembrane current also depends on the voltage-dependent sodium channel density at axon: the higher the density, the larger the transmembrane current will be. Thus the higher the density of voltage-dependent sodium channels, the larger the positive signal amplitudes. Due to the similar reason, the negative signal amplitudes will depend on the potassium channel density.

The time course of signal waveform depends on the activation, inactivation kinetics of the ion channels, because the time course of transmembrane currents depends on them. The voltage-dependent potassium channel is responsible for the repolarization of the membrane. Therefore, the spatial distribution of the density and the proportion of different types of potassium channels also affect the time course of the signal waveform. The less the fast-delayed-rectifier ion channels, the wider the signal waveforms.

Hence, as long as the axon diameter or the axonal ion-channel profile is different, we can distinguish the signals from different axons by the spike waveforms. It is still

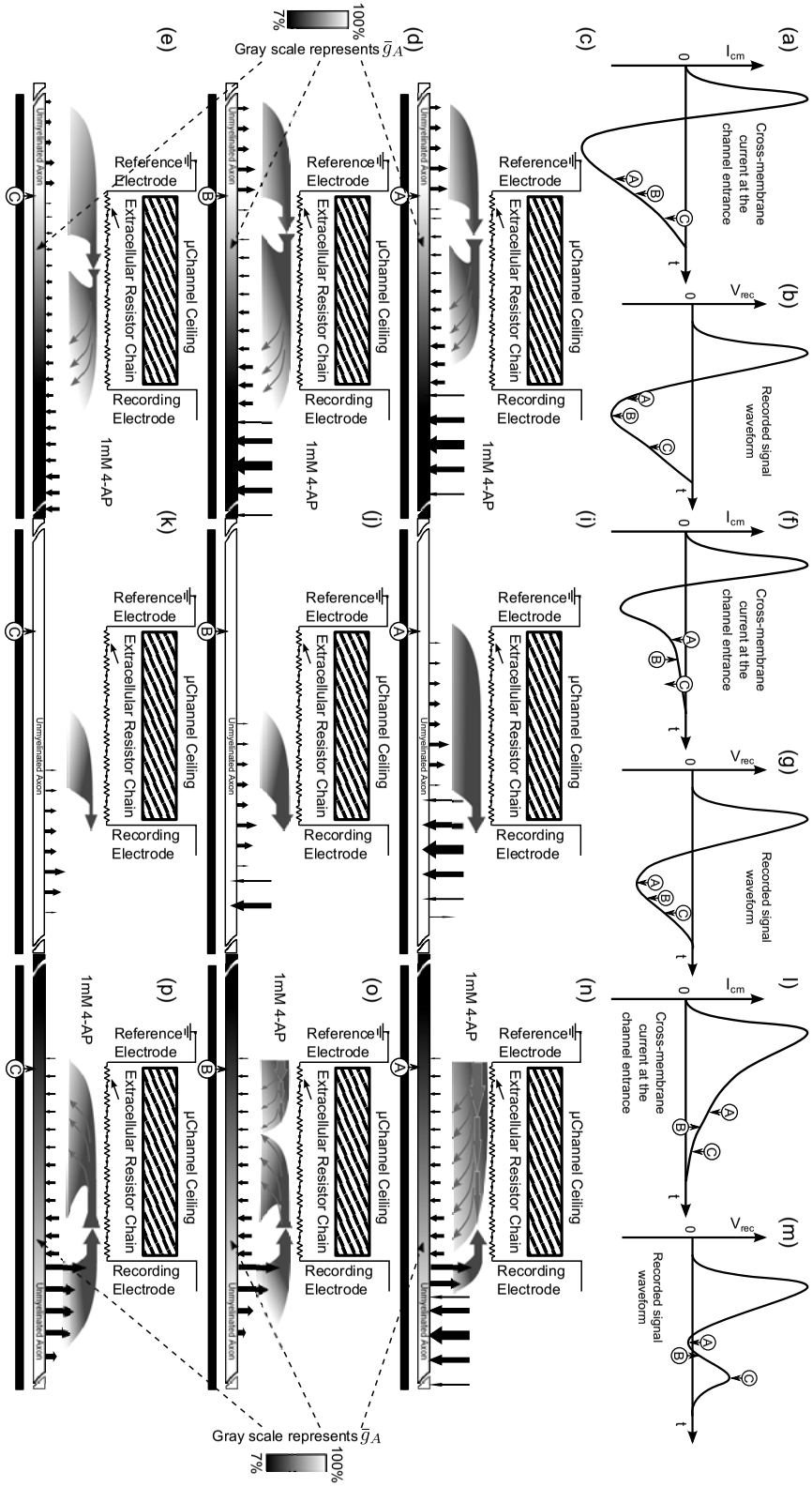

Figure 4.23. The origin of the signal-waveform variation caused by 4-AP II. This scheme illustrated the relationship among the transmembrane current (I_{cm}, vertical black arrows), the extracellular current (I_{ex}, horizontal grey arrows) and the recorded signal waveform V_{rec} under 3 different situations: no 4-AP at all (f-k), applying 4-AP in distal-well (a-e) and applying 4-AP in soma-well (l-p)

possible that some axons have similar axon diameters and ion-channel profiles which might generate similar signal waveforms, which cannot be distinguished like this. If there are two axons generate similar signal waveforms inside a microchannel, one would expect some overlapping of the similar spike units occasionally, especially during a burst activity. Because the minimum delay between the spikes propagated in different axons would not limited by the refractory period. However, we never observed such a phenomenon. This implies that, in most cases, the difference of the intrinsic criteria of axons in our experiments is big enough to generate distinguishable signal waveforms.

4.5.4 Proportion of a special ion current in total ion current

During the development [149, 151–153, 155] or due to pathological change of axons [131–134], there is a variation of the proportion of the axonal ion-channel types. The learning process may also require adjustment of this proportion [139, 148]. Hence it may provide important data in those research fields by monitoring the variation of the proportion of different ion currents in development model or memory formation model in vitro.

In our device, the less the density of an ion channel, the less effect of its blockade on the signal waveform. In extreme case, if there is no targeted ion channel in the axon compartments inside the microchannel, the signal waveform will remain the same after the blockade applying to the culture. Thus the variance of the signal waveform after applying the blockade can indicate the proportion of the target ion channel.

Figure 4.3 shows that there is a dependence of fast delayed-rectifier channel density and the variance of intergeneration of signal waveforms. If there is any chemical or physical stimulation can vary the proportion of the ion channels on axons in microchannels, we should be able to monitor a variation of the signal waveform and a change on the block effect of ion-channel blockades.

After the variance being normalized to the positive peaks, difference caused by the axon diameter can be reduced (figure 4.24). Thus comparing the ion current proportion between different axons or different neuron types is also possible.

4.5.5 Dosage response curve

The dosage response curve is important for the drug discovery, because it indicates the specificity and the efficiency of a potential therapeutic compound. The dosage response

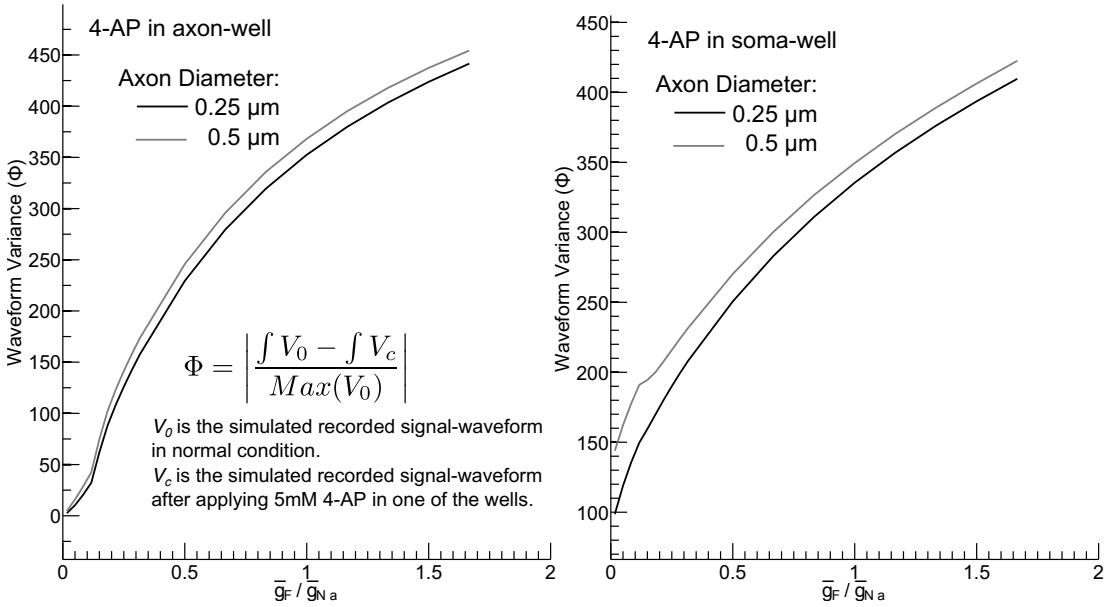

Figure 4.24. The dependence of simulated waveform variance induced by 5 mM 4-AP on the ratio of fast-delayed-rectifier channel (K_F) density ($\bar{g}_F$) to voltage-dependent sodium channel density ($\bar{g}_{Na}$). The dependence is a monotonic increasing function: the more the K_F the larger the variance. There is a small difference between the variance of waveforms obtained from the 0.25-μm-diameter axons and the 0.5-μm-diameter axons. (a) The 4-AP is applied into axon-well only. (b) The 4-AP is applied into soma-well only.

curve of known blockade can also facilitate to identify the type of ion channels in the axon membrane.

Due to lack of control on membrane potential, the response curve of the V_{rec} is far more complicate than voltage-clamp recording. For example, when the I_F gets blocked, the raising of membrane potential is much faster than normal condition, resulting in earlier inactivation of the voltage dependent sodium channel. Thus the total I_{Na} is smaller than normal condition. Due to the voltage potential drop more slowly, the total I_K is bigger than normal condition. Therefore, it is difficult to obtain the absolute g_F in our device by comparing the signal waveforms before and after applying 4-AP.

Hence, the Kd obtained by analyzing spike waveform variation may be difficult to compare with the Kd obtained by patch-clamp recording. For primary fast screening, the accuracy is already enough to determine which compound has smaller Kd than known compound or to tell whether the compound has enough specificity (figure 4.16).

However, there is a non-linear correlation between the block effect calculated from the variation of spike waveform and the theoretical block effect (figure 4.25), which reduces the accuracy of estimated Kd.

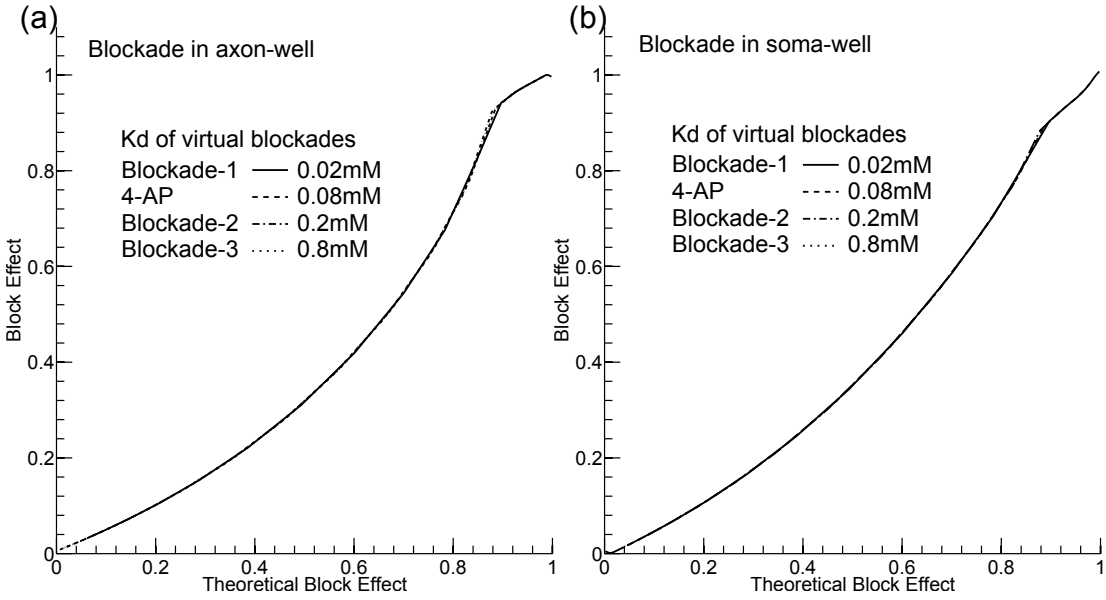

Figure 4.25. The nonlinear relationship between the block effects estimated from the waveform variance and the expected theoretical block effects of the 4 virtual blockades. The relationship is a monotonic increasing function. The simulation results show that the function does not affected by the Kds of the virtual blockades. There is a difference between the functions for the blockade in the axon-well (a) and in the soma-well (b).

Luckily, the relationship is monotonic. Hence mapping the spike waveform variation to the normal block effect of knowing compound may improve the accuracy of determining the Kd of an unknown compound. The variance of this relationship caused by axon diameters is also small. Figure 4.26 shows that the Kd-estimation accuracy of the model with 0.5-μm-diameter axons were improved by using the mapping function obtained in the model with 0.25-μm-diameter axons (figure 4.25).

4.5.6 Applying chemical compounds to different compartments

Another advantage of our device is allowing applying chemical compounds in different compartments. The chemical compounds affecting the ion-channel gating mechanisms, are usually excitatory or inhibitory to the network activity also. For example, the 4-AP will increase the firing rate of the whole network if applied to soma-well, i.e. increase the spike density during the burst activity. Combine with the widening effect on the

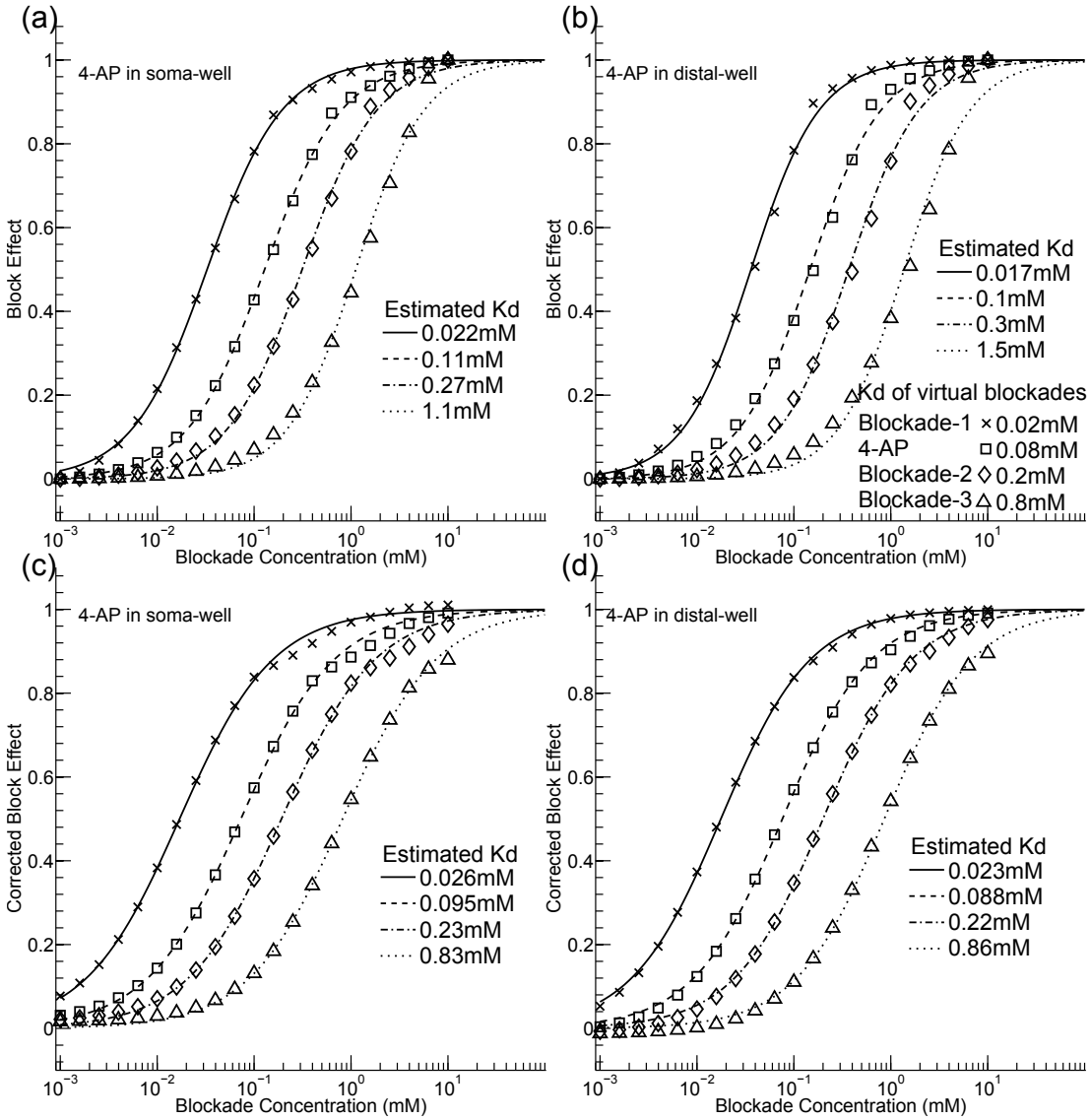

Figure 4.26. Correct the dosage response curves by mapping the estimated block effect to the theoretical block effect of the known blockade (4-AP). In this figure, the axon diameters of all the models are 0.5 μm. The block-effect-mapping function is obtained by spline-fitting of the data showed in the figure 4.25, which modelled with 0.25-μm-diameter axons. (a-b) The simulated dosage response curves of 4 different virtual blockades. (c-d). The simulated dosage response curves of 4 different virtual blockades after mapping the estimated block effect to the theoretical block effect of the known blockade (4-AP).

spike waveform, applying 4-AP in soma-well can result in severe overlapping of the spike units, increasing the difficulty in data analysis.

The TTX in soma-well can dramatically decrease the network activity, which usually silences most of the units inside the microchannel. However, applying them in distal-well will not affect the network activity, easing the analysis of the compound effect on spike waveforms. Although we only demonstrate two compartments version, it is not difficult to scale up to more compartments, via vertical superfusion channels. Multi-compartment devices may allow researchers study the dependence of the axonal ion-channel profile on the distance to the soma.

4.5.7 Fluid barrier effect of the spontaneous seal

Without any cell culture, the flow inside the microchannel is relatively fast (20-40 μm/s). The LY can fill up the microchannel within 1 min, when the liquid level of LY is about twice of the liquid level of NB. This flow also prevented the LY from entering the channels, when the liquid level of LY was lower than NB.

After cell tissue clogging the microchannels, the flow speed was dramatically reduced. Thus the diffusion became the dominant mass transfer mechanism inside the microchannel. The channel A_c (< 200 μm^2) is so small comparing to the A_c of culture wells (mm^2 range).

Hence the variation of the concentration in the wells due to the diffusion through the microchannel can be ignored within at least 1 hour after chemical compound applied in one of the wells. The microchannel therefore behaves as a fluid/chemical barrier between those two compartments. The chemical compound added into one of the wells can be regarded as applied exclusively to the microchannel and the targeted well if the experiment does not last longer than hours. For longer experiments, one might need to renew the medium every several hours (the exact exchange frequency depends on the microchannel geometry, culture well geometry and the diffusion coefficient of the compound), or use a superfusion device to exchange the medium continuously at a relatively low speed.

4. MICROCHANNEL ENHANCED ELECTROPHYSIOLOGY PLATFORM FOR FUNCTIONAL ION-CHANNEL PROFILING ON AXON COMPARTMENT

Chapter 5 Microwell-microchannel enhanced multi-electrode array for low-density dissociated hippocampal culture, part I: biophysics and optimal design

5.1 Abstract

We have previously described that the use of microchannels as substrate-integrated equivalents of micropipettes is a potentially high-throughput, low-cost alternative to conventional multi-electrode arrays with a moderate-to-low complexity of use. By studying the biophysics of the signal generation inside microchannels, we established the impact of the microchannel shape on the signal amplitude and SNR, while the microchannel is only grounded at one end and the signal is recorded at the other end. In this chapter we continue to explore the impact of the microchannel length and intrachannel-electrode position on the signal amplitude, when the microchannel is grounded at both ends and the signal is recorded by intrachannel electrodes. Via numerical simulations and experiments, we demonstrate that the longer the microchannel the larger the signal amplitude, and the largest signal amplitudes can be obtained from intrachannel electrodes located ∼70-140 μm to the microchannel entrances. The direction of the action potential propagation can also be determined by the signal delay on multiple electrodes. This renders microchannel as a promising enhancer of the multi-electrode array to record the network activity from multiple positions of the neural culture.

5.2 Introduction

To study information processing, synaptic plasticity and network formation of the small neuronal networks, it requires monitoring as many neurons as possible inside the network and as long as possible. With single electrode techniques such as patch clamp and intracellular recording, it is difficult to record more than 3-5 neurons . Due to the mechanical vibration and the wounds introduced by electrode-cell-membrane contact, they only allow recording from same neurons for a few hours. Thus, after introduced in 1970s [43–45], the multi-electrode array with micron-scale electrodes are

widely used in basic neuroscience research [7–13], drug screening [14, 15] and toxicology [27, 28], because of the capability of recording neural activity from multiple position simultaneously for several weeks.

From then, researchers are intensively labouring to improve the signal-to-noise ratio of MEAs. Most of the efforts are focused on providing better electrode materials [48–56] or micro-electrode shapes [57, 58]. Alternatively, we had already demonstrated that an optimized microchannel resembling suction electrode can provide stable AP waveforms with relatively high mean SNR (101±76 chapter 3), even comparable to the maximum SNR obtained with CNT-coated electrodes (∼135 [54]) or Si-NWFET (∼210 [55] and ∼120 [56]). Comparing to most contemporary modifications to MEAs, the microchannel is easy to fabricate with relatively low costs. Another advantage of the microchannel is that the AP propagation direction can be simply determined by the signal delay on multiple electrodes in the same microchannel (chapter 4), which may facilitate the connectivity analysis of the neuronal network.

Utilizing the microchannel as a signal enhancer for an MEA requires embedding as many microchannels as possible in the cell-culture area on the MEA, and recording the signals from intro-channel electrodes. After the axon growing into a microchannel, one would expect a high SNR signal as we demonstrated with microchannel-macrowell configurations (chapter 3).

Two classes of designs are possible (figure 5.1) for embedding microchannel into MEAs. One is to create blind-channels on MEA (figure 5.1 (a)). In this design, the microchannel is only electrically grounded at the open end and the signal is recorded at the dead end, which resemble our microchannel-macrowell configurations in the previous work (chapter 3). Thus the impact of the microchannel geometry on SNR should follow the same rule as described in previous work (chapter 3): the best channel length is about 100-200 μm.

However, because the axon will grow into a blind-channel, the recorded axon may not participate in modulating the network activity. The other design (figure 5.1 (b)) is to integrate through-channels which allow axons to grow through the channel and reach neurons located at the other end of the channel to form functional connections. In this case, the microchannel is electrically grounded at both ends. The dependence of the signal amplitudes on the electrode position and the microchannel length in this design

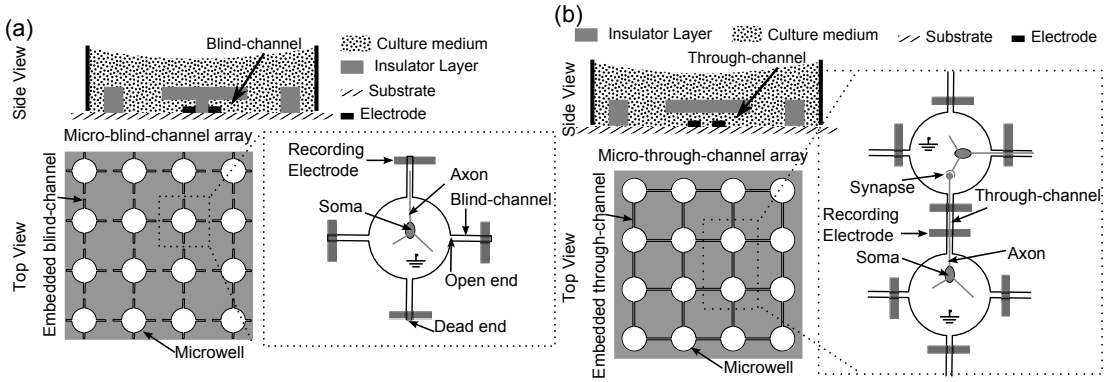

Figure 5.1. The scheme of two types of embedded microchannel arrays. (a) The embedded microchannels are blind-channels. Only the open ends (located in the microwells) are grounded. Recording electrodes are placed at the dead ends of microchannels. (b) The embedded microchannels are through-channels, of which both ends are grounded. The recording electrodes are placed inside the microchannels. Unlike the blind-channel version, the monitored axon can grow through the microchannel and form synapses with neurons in another well.

may be different from the configurations used in the previous work, in which only one channel end is grounded.

To optimize the microchannel length and the intrachannel electrode position, in this present work, we study the dependence of the intrachannel signal amplitudes and waveform shapes on microchannel lengths and electrode positions, when reference electrodes are placed in both soma and distal wells. Based on this study, we proposed an optimal channel length of 0.3 mm and the optimal intrachannel electrode position of 0.1 mm to the nearest channel entrance.

5.3 Methods

5.3.1 Device fabrication

The polymer microchannel devices were fabricated via previously established procedures (chapter 3). Briefly, a 5-mm-thick slab of PDMS was cured onto the master, peeled off, and punched to form two culture wells (6 mm in diameter).

The MEAs were also fabricated according to the previously described method (chapter 3). A 100-nm-thick ITO layer on the glass substrate was etched to form 40-μm-wide electrodes with 60-μm separation. Before culturing, the MEA was cleaned using oxygen plasma for 15 mins in a PDC-002 plasma oven (Harrick Scientific) to enhance

hydrophilicity.

5.3.2 Cell culture and electrophysiology

Dissociated cultures of mouse hippocampus neurons were prepared as described previously (chapter 3). Before plating, the MEA was coated with 0.1% poly-L-lysine overnight and then resined and dried under laminar flow. MEAs with neurons at 14 day in vitro (DIV) were recorded in a dry incubator (37°C, 5% CO_2) as described previously (chapter 3).

The data were analyzed according to previously described procedures (chapter 3) to detect and sort the spikes.

5.3.3 Numerical simulation of compartment models

Table 5.1: Parameters of modelled compartments. [a]

	Length (μm)	Diameter (μm)	C_m ($\mu F/cm^2$)	$\bar{g}_{Na}$ (mS/cm^2)	$\bar{g}_F$ (mS/cm^2)	$\bar{g}_K$ (mS/cm^2)
Soma	20	20	0.75	60	5	2.4
Axon initial segment	10	2	0.75	600	24	2.4
Myelinated axonal segments	100	0.25	0.4[b]	60	24	2.4
Nodes	1	0.25	0.75	180	24	2.4

[a] Values are based on previous reports of pyramidal neurons [159, 163].
[b] This value was adapted to fit the full width of half maximum of the positive peak of recorded signals.

Models were written in M script language and computed using MATLAB. Table 5.1 describes the detail of the model used in this chapter. By default, a neuron model consists of a 20-µm-long soma with a diameter of 20 µm, a 10-µm-long axon initial segment (AIS) with a diameter of 2 µm, a 3000-µm-long axon with a diameter of 0.25 µm and a 300-µm-long microchannel with a cross-section area (A_c) of 5 μm^2. The soma is placed $\sim$ 50 µm from the microchannel entrance.

The parameters for myelination, passive parameters and ion-channel kinetics (table 5.2, 5.3) are all based on previous reports of pyramidal neurons [159, 163]. Briefly, 3 populations of voltage-dependent ion channels were modelled in this chapter, a fast

delayed rectifier g_F and a slow delayed rectifier g_S and a voltage-dependent sodium conductance g_{Na}.

Table 5.2: Hodgkin - Huxley model parameters I

Passive components			
Extracellular resistivity		$\rho_{ex} = \begin{cases} 2.55\Omega \cdot m;\ L_x \leq 200\mu m \\ 1.04\Omega \cdot m;\ L_x > 200\mu m \end{cases}$	
Intracellular resistivity	$\rho_i = 0.7\Omega \cdot m$	Leak membrane conductance density	$g_L = 0.7S/m^2$
Membrane capacity	$C_m = 0.0075F/m^2$	Leak Nernst potential	$E_L = -57mV$
Active components[a]			
Voltage-dependent Na^+ channel		$g_{Na} = \bar{g}_{Na} \cdot m^3 \cdot h \cdot s$	
Fast delayed rectifier K^+ channel		$g_F = \bar{g}_F \cdot n^4$	
Slow delayed rectifier K^+ channel		$g_S = \bar{g}_S \cdot u^2$	
Na^+ Nernst potential	$E_{Na} = 55mV$	K^+ Nernst potential	$E_K = -85.7mV$

[a] The m, h, s, n, u are the ion-channel kinetic parameters in pyramidal neurons (Adapted from [163]).

Table 5.3: Hodgkin - Huxley model parameters II.

Kinetic parameters[a]	
For all parameters	$\tau_x(V) \cdot \frac{dx(V,t)}{dt} = x_\infty(V) - x(V,t); \quad x \in [m,\ h,\ s,\ n,\ u];$
m	$\tau_m(V) = \frac{1}{2.5(\alpha_m(V)+\beta_m(V))};$ If $\tau_m(V) < 0.02$ then $\tau_m(V) = 0.02;$ $m_\infty(V) = \frac{\alpha_m(V)}{\alpha_m(V)+\beta_m(V)};$ $\alpha_m(V) = \frac{0.4(V+30)}{1-e^{-\frac{V+30}{7.2}}};\ \beta_m(V) = \frac{-0.124(V+30)}{1-e^{\frac{V+30}{7.2}}}$
h	$\tau_h(V) = \frac{1}{2.5(\alpha_h(V)+\beta_h(V))};$ If $\tau_h(V) < 0.5$ then $\tau_h(V) = 0.5;$ $h_\infty(V) = \frac{1}{1+e^{\frac{V+50}{4}}};$ $\alpha_h(V) = \frac{0.03(V+45)}{1-e^{-\frac{V+45}{1.5}}};\ \beta_h(V) = \frac{-0.01(V+45)}{1-e^{\frac{V+45}{1.5}}}$
s	$\tau_s(V) = \frac{\beta_s(V)}{0.0003(\alpha_s(V)+1)};$ If $\tau_s(V) < 10$ then $\tau_s(V) = 10;$ $s_\infty(V) = 1;\ \alpha_s(V) = e^{\frac{139.24V+60}{310.15}};\ \beta_s(V) = e^{\frac{27.85V+60}{310.15}}$
n	$\tau_n(V) = 0.1 + \frac{0.5}{1+e^{\frac{V+27}{15}}};\quad n_\infty(V) = \frac{1}{1+e^{-\frac{V+35}{10}}};$
u	$\tau_u(V) = \frac{3}{9.5(\alpha_u(V)+\beta_u(V))};\quad u_\infty(V) = \frac{\alpha_u(V)}{\alpha_u(V)+\beta_u(V)};$ $\alpha_u(V) = \frac{0.016}{1-e^{-\frac{V+52.7}{23}}};\ \beta_u(V) = \frac{0.016}{1-e^{\frac{V+52.7}{18.8}}}$

[a] The m, h, s, n, u are the ion-channel kinetic parameters in pyramidal neurons. (Adapted from [163])

5.4 Results

Unlike macrowell-microchannel devices recording signal from one of the 2 wells, microwell-microchannel devices are submerged in culture-medium, leading to electrical shortcuts between all the wells. Thus only intrachannel recording is possible for the microwell device. The blind-channel configuration (only one end was located inside the well) is equivalent to macrowell-microchannel devices with reference electrode only in soma-well, studied previously (chapter 3). The simulated dependence of signal amplitudes on intrachannel-electrode positions are showed in figure 5.2.

Because, in the through-channel configuration, the two ends of the microchannel are shortcut by the culture-medium, the dependence of the intrachannel signal amplitude and waveform shape can be different. Therefore, in following sections we focus on the through-channel configuration which has reference electrodes in both wells.

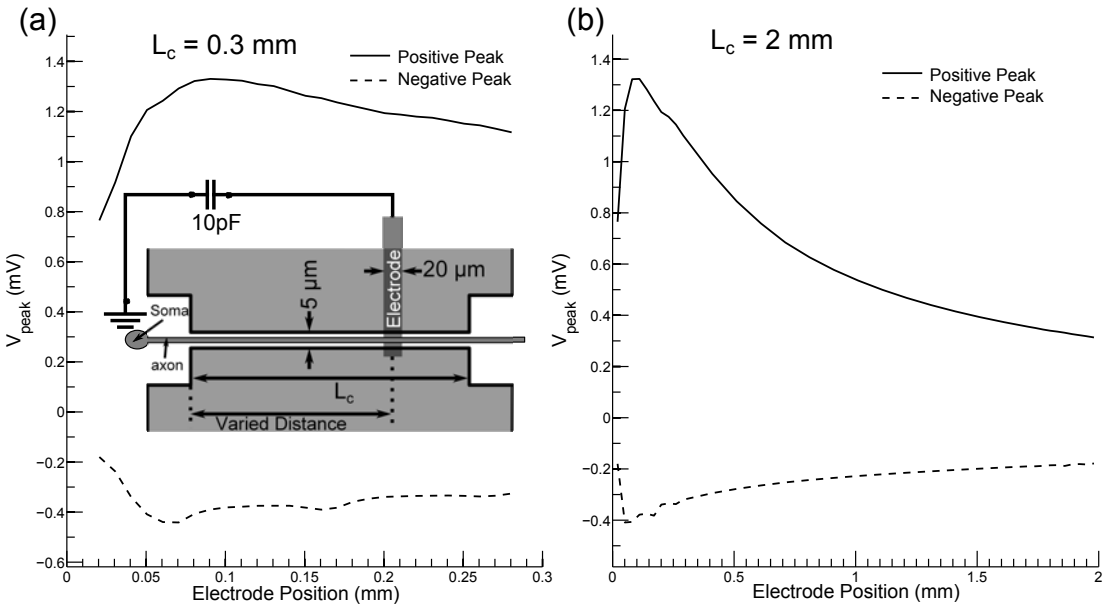

Figure 5.2. The simulated dependence of signal positive amplitudes (solid line) and negative amplitudes (dashed line) on electrode positions in 0.3-mm-long (a) and 2-mm-long (b) microchannels, with the reference electrodes only placed in soma-wells. Inset illustrates the model configuration: a channel cross-section area of 5 μm^2, 10pF stray capacitance, 20-µm-wide electrode. The soma is 0.05 mm to the soma-side channel entrance. The myelinated axon is 3-mm-long.

5.4.1 The optimal position for intrachannel electrodes

To understand the impact of position of the intrachannel electrode (ICE) on the signal amplitude, a series of numerical simulations with different distance (0.02 - 0.28 mm for 0.3-mm-long microchannel and 0.02 - 1.98 mm for 2-mm-long microchannel) between the ICE and soma-side channel entrance (proximal entrance) were performed. The models contain: a soma 0.05 mm to the proximal entrance, a 3-mm-long myelinated axon, a 0.3-mm-long or 2-mm-long, 1-μm-high and 5-μm-wide microchannel, a 10-pF stray capacitance, and reference electrodes in both soma and distal wells (Figure 5.3 (a) inset).

Figure 5.3 (a, c) show that the dependence of signal amplitudes on electrode positions in the 2-mm-long microchannel and 0.3-mm-long microchannel are similar. The positive amplitude reaches its maximum value when the centre of the electrode is located at ∼80 μm to the proximal entrance in both cases. The negative amplitude reaches its maximum value when the centre of electrode is located at ∼70 μm to the distal-side entrance (distal entrance) for the 0.3-mm-long microchannel (Figure 5.3 (a)) or at ∼140 μm to the distal entrance for the 2-mm-long microchannel (Figure 5.3 (c)). Interestingly, when the electrodes are located near to the distal entrance, the simulations predict a negative-peak-dominating waveform, although it is still positive leading (Figure 5.3 (b, d)).

In the 2-mm-long microchannel, placing reference electrodes in both wells and just placing reference electrode in the soma-well (Figure 5.2 (b)) will lead to similar maximum value of the positive amplitude. However, in the 0.3-mm-long microchannel, placing reference electrodes in both wells will lead to ∼30% smaller maximum value of the positive amplitudes than placing reference electrode in soma-well only (Figure 5.2 (a)).

To verify the simulation result, the intrachannel extracellular potentials at different locations in a 3.7-μm-high, 25-μm-wide, 1.0-mm-long microchannel, and in a 3.7-μm-high, 25-μm-wide, 1.6-mm-long microchannel were recorded by ITO electrode. All average signal waveforms were plotted in figure 5.4 and figure 5.5.

As predicted by the simulation result, figure 5.6 (a-b) show that the dependence of positive amplitudes of all the units follow the positive-skewed bell curve. 8 out of 9 units reach their maximum amplitudes at the 2nd electrode (∼120 μm from centre to

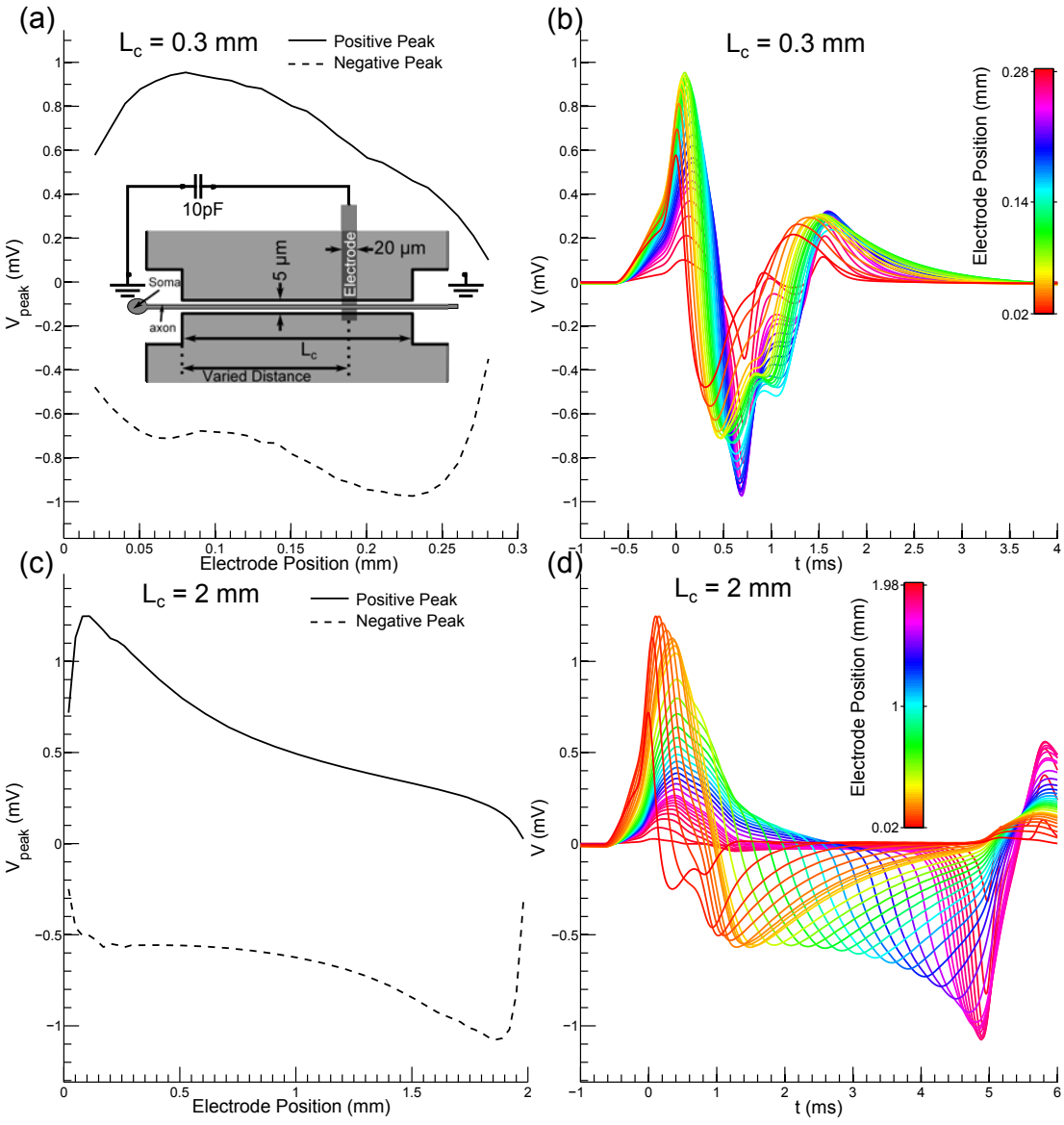

Figure 5.3. The simulated impact of electrode positions on signal amplitudes (a, c) and waveforms (c, d) in 0.3-mm-long (a-b) and 2-mm-long (c-d) microchannels, with the reference electrodes placed in both wells. Inset illustrates the model configuration: a channel cross-section area of 5 μm^2, 10pF stray capacitance, and 20-µm-wide electrode. The soma is 0.05 mm to the proximal entrance. The myelinated axon is 3-mm-long.

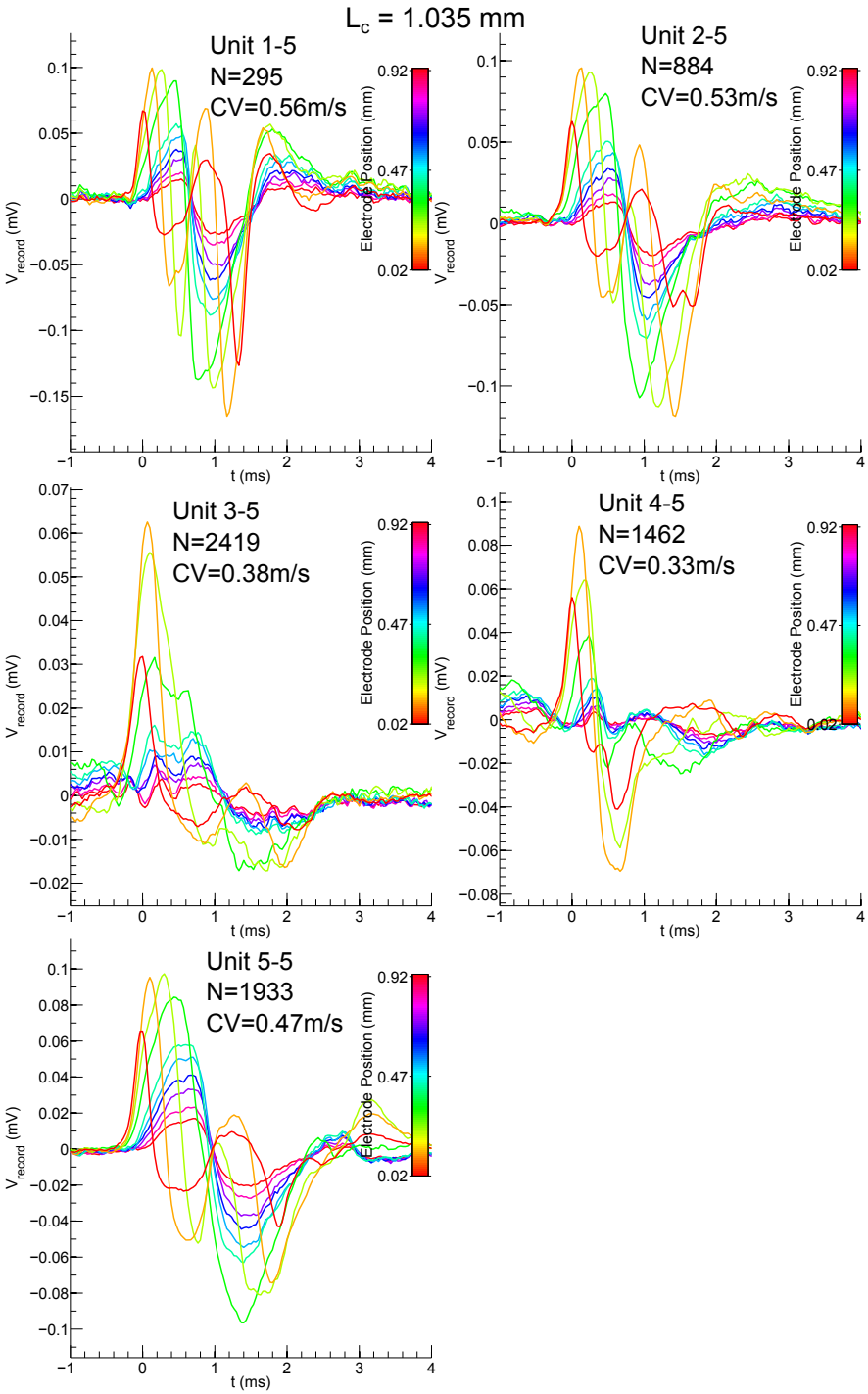

Figure 5.4. The impact of electrode positions on average signal waveforms of all 5 units recorded from a 3.7-μm-high, 25-μm-wide, 1.0-mm-long microchannel with reference electrodes in both wells at 14 Day in vitro. The colours identify the electrode positions. The conduction velocities (CV) are from 0.33 to 0.56 m/s. The number of spikes per unit is from 295 to 1933.

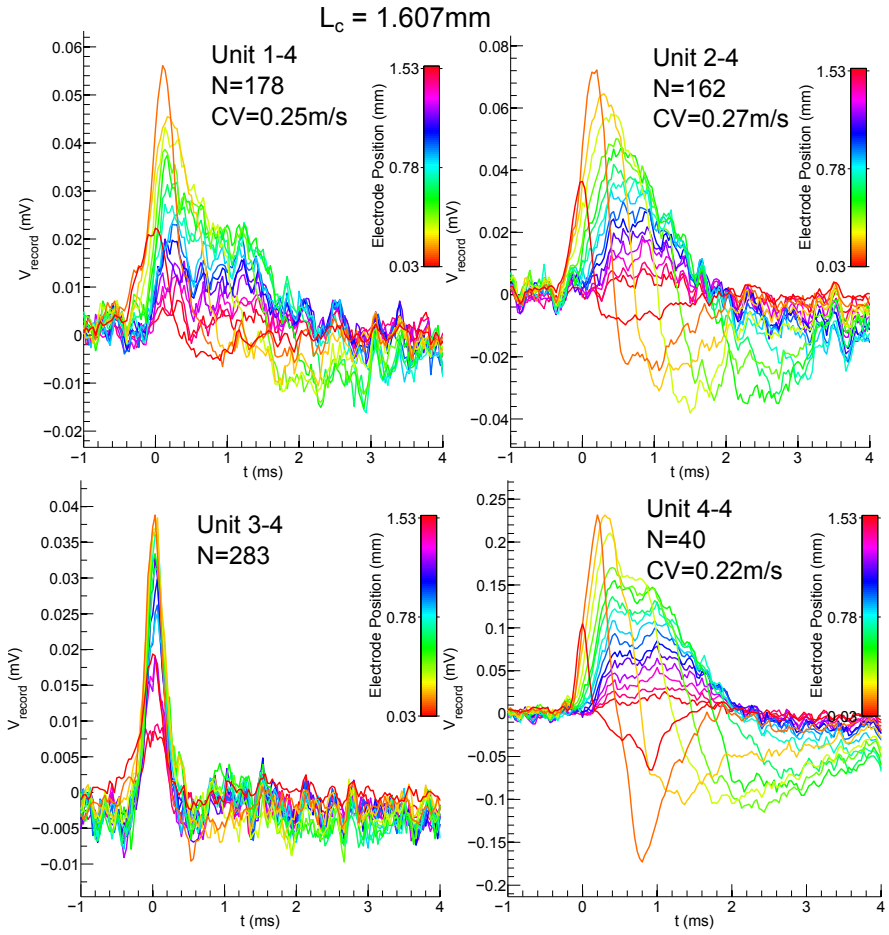

Figure 5.5. The impact of electrode positions on average signal waveforms of all 4 units recorded from a 3.7-μm-high, 25-μm-wide, 1.6-mm-long microchannel with reference electrodes in both wells at 14 Day in vitro. The colours identify the electrode positions. The conduction velocities (CV) are from 0.22 to 0.27 m/s. The number of spikes per unit is from 40 to 283. Because the unit 3-4 does not have obvious delay on different electrodes that it is impossible to calculate CV.

the proximal entrance). 1 unit (figure 5.6, unit 5-5) reaches its maximum amplitudes at the 3rd electrode (∼220 µm from centre to the proximal entrance). However, the amplitude of this unit on 2nd electrode is only 2% smaller than the amplitude on 3rd electrode.

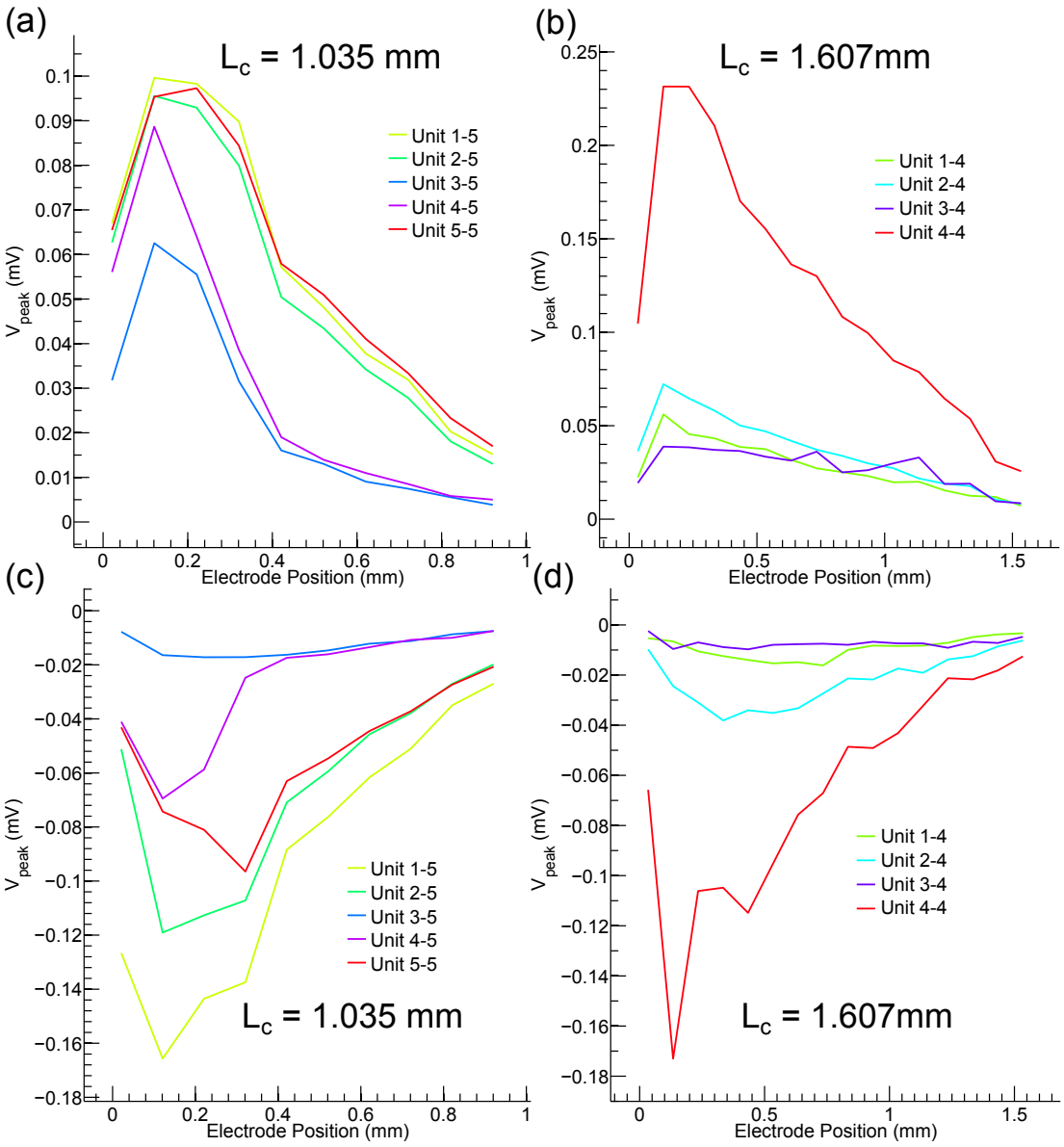

Figure 5.6. The impact of electrode positions on signal positive amplitudes (a-b) and negative amplitudes (c-d) in 1.0-mm-long (a, c) and 1.6-mm-long (b, d) microchannels (3.7-µm-high, 25-µm-wide), with the reference electrodes placed in both wells.

In real device the somata can be placed in both sides. Thus, to optimize the signal amplitudes whereas the neuronal somata are located, we designed two electrodes for each microchannel, with a 100-μm distance from electrode centre to the nearest channel entrance. Another advantage of two electrodes per microchannel is that the AP propagation direction can be revealed by the delay between those two electrodes. If the AP is propagating from electrode A to electrode B, the signal on electrode B will have a positive delay related to the signal on the electrode A, vice versa.

5.4.2 The optimal microchannel length

To find the optimal microchannel length (L_c), a series of numerical simulations were performed with varied L_c. The models (Figure 5.7 inset) are similar to those in the previous section, but with several differences: two 20-μm-wide electrodes with minimum 100 μm to microchannel entrances, and 10-pF stray capacitance for each electrode.

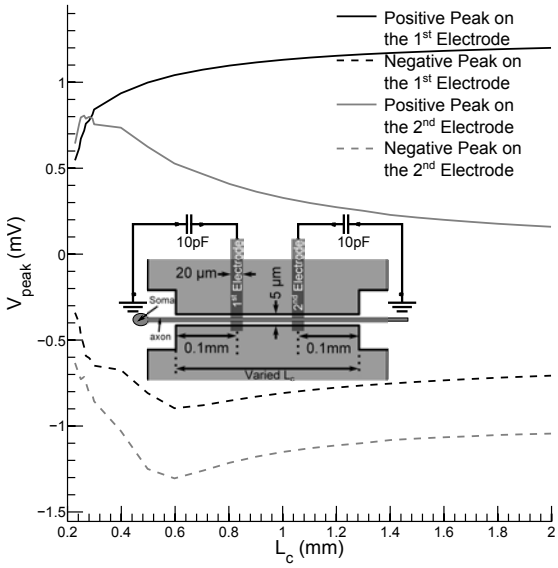

Figure 5.7. The simulated impact of channel length (L_c) on signal positive amplitudes (solid line) and negative amplitudes (dashed line). Inset illustrates the model configuration: a channel cross-section area of 5 μm^2, 10pF stray capacitance, and two 20-μm-wide electrodes with 0.1-mm distance to the nearest channel entrance. The soma is 0.05 mm to the proximal entrance. The myelinated axon is 3-mm-long.

The positive amplitude (Figure 5.7 black solid line) on the 1st electrode increases with increasing L_c. The slope decreases with increasing L_c. At L_c = 0.3 mm, the positive amplitude is already 70% of the amplitude at L_c = 2 mm. The dependence of the positive amplitude on the 2nd electrode (Figure 5.7 grey solid line) however is

not monotonic. The amplitude reaches maximum when L_c is ∼260 μm. The negative amplitudes (Figure 5.7 dashed lines) on both electrodes reach their maximum absolute value when L_c is ∼600 μm.

To make all 4 amplitudes as large as possible ($>$ 70% of the maximum value), the L_c should be from 0.3 mm to 0.5 mm. However the longer the channel the higher the defective rate during the fabrication. Thus, there is a trade-off between signal amplitudes and defective rate. Hence, 0.3-mm-long microchannel was chosen in this presented work.

5.4.3 Predict the variation of the signal waveform during long term recording

Numerical simulations show that the recorded signal waveform also depends on the length of the axon inside a microchannel (Figure 5.8). The models (Figure 5.8 (a)) are the same as in the previous section with following differences: the varied axon length, and fixed microchannel length (0.3 mm).

The positive amplitude on each electrode will reach its maximum value after the axon crossing the corresponding electrode and extending 50-μm further. The positive amplitudes on the 2nd electrode are always smaller than on the 1st electrode.

The negative amplitude on the 1st electrode will keep increasing with increasing axon length until the axon goes through the microchannel. The negative amplitude on the 2nd electrode will keep increasing with increasing axon length until the axon extending ∼150 μm beyond the distal entrance. The absolute value of negative amplitudes on the 2nd electrode usually are also smaller than on the 1st electrode, before the axon growing through the entire microchannel.

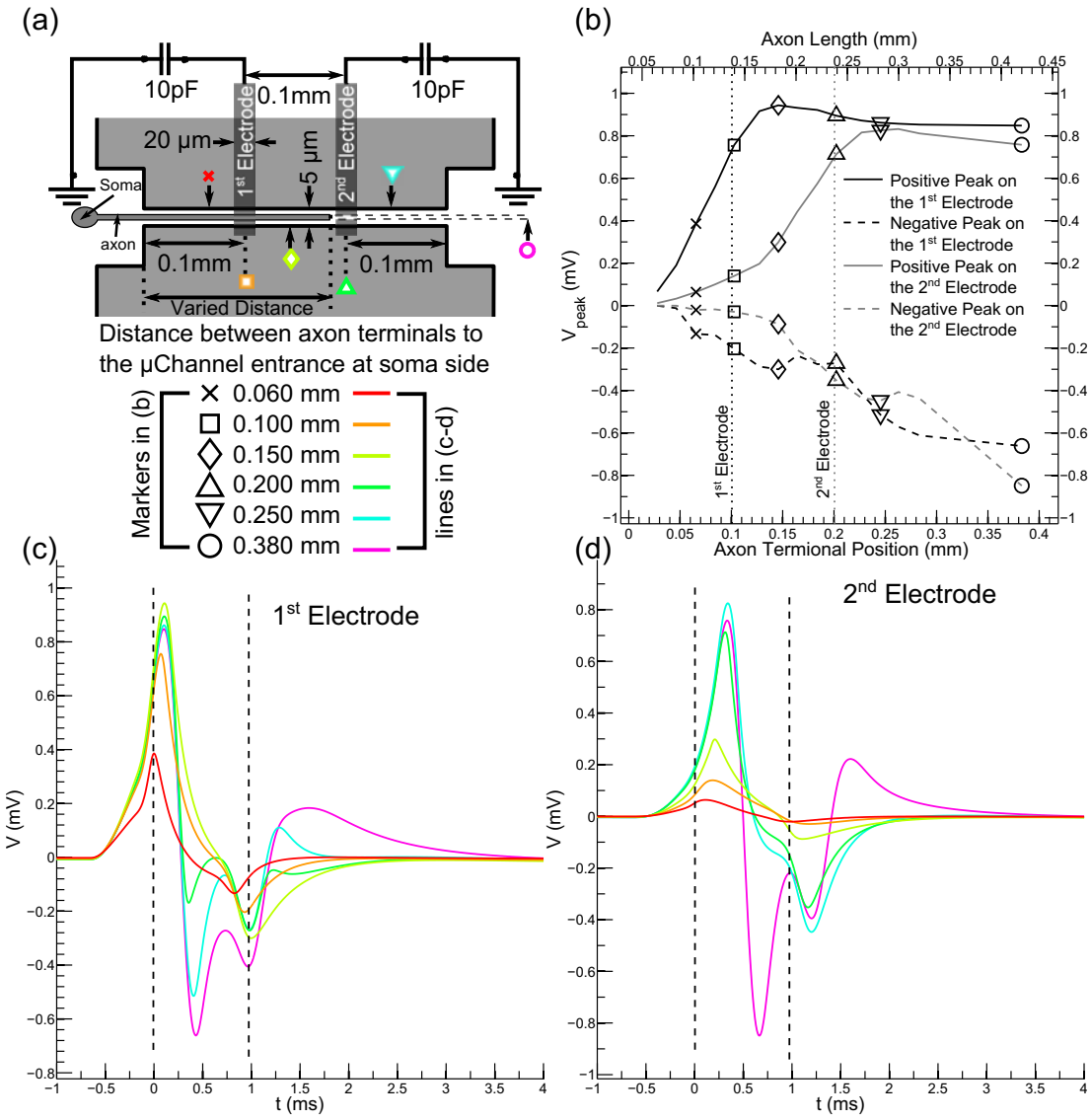

Figure 5.8. The simulated impact of the axon terminal position on signal amplitudes (b) and waveforms (c, d). (a) illustrates the model configuration: a 0.3-mm-long microchannel with a channel cross-section area of 5 µm^2, 10pF stray capacitance, and two 20-µm-wide electrodes with 0.1-mm distance to the nearest channel entrance. The soma is 0.05 mm to the proximal entrance. The myelinated axon length is varied. Coloured markers illustrate positions of the myelinated axon terminal. Marker shapes are correlated to the panel b. Marker colours are correlated to the line colours in panel c-d. (b) The signal positive amplitudes (solid lines) and negative amplitudes (dashed lines) on two different electrodes. The dotted lines identify the electrode positions. (c) The waveforms recorded from the 1st electrode. (d) The waveforms recorded from the 2nd electrode.

5.5 Discussion and conclusions

By simulation and experiments we demonstrated that it is possible to utilize embedded micro through-channels and intrachannel electrodes as signal amplitude enhancers for multi-electrode arrays (MEAs).

Both simulation and experiments show that the optimal intrachannel electrode position is ∼0.07-0.14 mm to the nearest channel entrances. The simulation data show that the longer the channel length the larger the signal amplitudes. However, the longer the channel the lower the yield rate of the microfabrication process. A compromise length of 0.3 mm, whose signal amplitude is around 70% of the signal amplitude in the 2-mm-long microchannel, is chosen.

Thus we propose a prototype of microwell-microchannel enhanced MEA (MWMC-MEA) with 1-μm-high, 5-μm-wide, 0.3-mm-long microchannels connecting micro culture wells, and 2 intrachannel electrodes with a distance of ∼0.7-0.1 mm to the nearest microchannel entrance.

While the axon grows into the microchannel, the signal waveform on both electrodes will vary. Before the axon terminal passes the first electrode inside a microchannel, the signal delay on two electrodes can be ignored. But once the axon passes the first electrode the signal delay can be used to determine the signal propagation directions, which is another advantage of such a device additional to the high SNR.

We fabricated such a prototype by PDMS and ITO-glass substrates. The signal amplitude is relatively large, from 13 up to 142 (figure 5.9). Interestingly, it is rare to see the huge negative peaks as we predicted in the model. This may be attributed to the axon not growing through the microchannel yet or imply that the ion-channel distribution is not a constant value along the axon, or the axon diameter becomes very thin in the distal axonal segments. This deserves future study by MWMC-MEAs.

The choice of microwell sizes, the choice of insulation layer materials and fabrication details, will be discussed in next chapter.

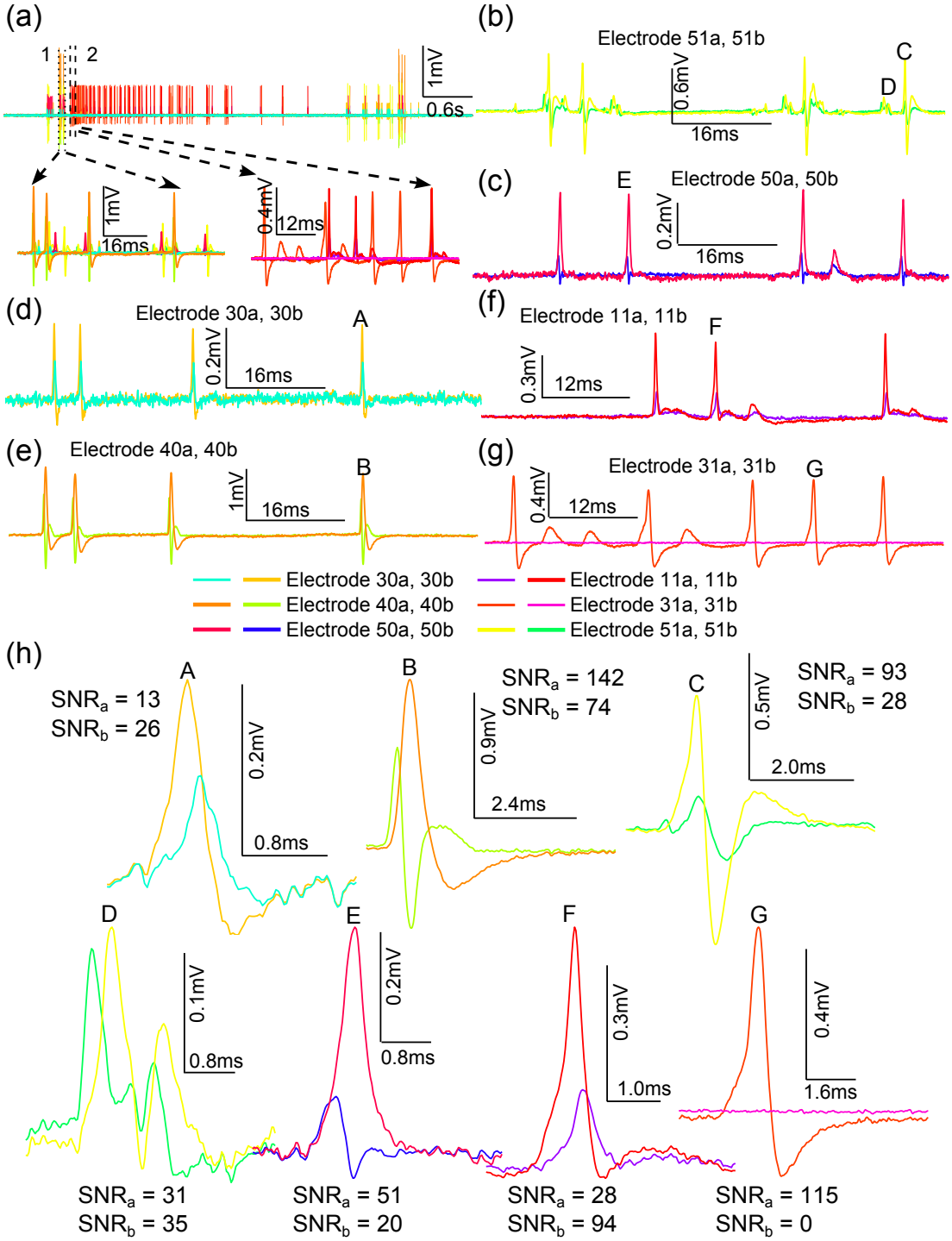

Figure 5.9. The raw signal traces from low-density dissociated hippocampal culture at 14 DIV. In each 1-μm-high, 5-μm-wide and 0.3-mm-long microchannel, two signals were recorded by two intrachannel electrodes. The electrodes are labelled by number in form of 'NMa/b'. The NM is the serial number of microchannels. The letter (a or b) identify the two electrodes in the same microchannel.

5. MICROWELL-MICROCHANNEL ENHANCED MULTI-ELECTRODE ARRAY FOR LOW-DENSITY DISSOCIATED HIPPOCAMPAL CULTURE, PART I: BIOPHYSICS AND OPTIMAL DESIGN

Chapter 6 Microwell-microchannel enhanced multi-electrode array for low-density dissociated hippocampal culture, part II: fabrication and recordings

6.1 Abstract

We have previously described the feasibility of utilizing microchannel arrays to enhance the signal amplitude of multi-electrode arrays (MEAs). An optimal channel length of 0.3 mm and the optimal intrachannel electrode position of 0.1 mm to the nearest channel entrance had been proposed based on numerical simulation and experiment results. In the present work, we demonstrated a prototype of microwell-microchannel enhanced MEA (MWMC-MEA), whose through-hole feature of Polydimethylsiloxane film (PDMS) was fabricated by reactive-ion etching (RIE) with the CHF_3/O_2 plasma. The low-density culture (57 neurons/mm^2) were survived on the MWMC-MEAs for at least 14 days, from which the neuronal signal with the maximum SNR of 142 was obtained.

6.2 Introduction

6.2.1 Microstructure enhanced MEAs

One of the foci of contemporary neuroscience is to explore the computational capability of in vitro neuronal circuits. Studying their connection development and long-term plasticity may elucidate the mechanisms of the learning, memory and pattern recognition in human brains [59, 164]. Facilitated by multi-electrode arrays (MEAs), there are emerging evidences show even the in vitro neuronal cultures are capable of learning, memory [10, 11], and pattern recognition [12, 13].

However the mechanisms behind those complex behaviours are only partially understood. One of the main reasons is that only a small fraction, on the order of 1%, of neurons are monitored at unclear sites on the MEA [47, 59]. The soma need to be within ~5 μm of a micro-electrode [60, 61] to generate recordable extracellular signals.

Moreover, the cells tend to migrate, leading to unstable electrode-neuron interfacing [62]. To overcome these limitations, many efforts focus on increasing ratio of number of distinguishable units to number of neurons in the network.

Most straightforward research line is to increase electrode density, bringing the spatial resolution to sub-cellular scale. Hence, a neuron can generate recordable signals whereas the soma is located. Due to the wiring difficulty and high impedance of thin leads from electrodes to amplifiers, these MEAs usually require integrated on-chip pre-amplifiers, fabricated on the silicon wafer [63, 64]. That not only increases the fabrication costs and complexity, but also restricts the optical access to on-chip neuronal cultures due to the opacity of the substrates.

Others resort to physically or chemically anchor neurons onto electrodes. Microwells etched in bulk silicon [65], polyimide picket fences [66], SU-8 microwells [67], parylene cages [47], and agarose microwells [68, 69] were successfully applied on MEAs to anchor neurons. Bioactive molecules were usually patterned on to MEA surface by laser ablation [70], photolithography [71], or microcontact printing [72, 73] as chemical cue to confine neuron growth and migration. Recently a dried 1-μm-high agarose layer were also used as efficient neuron-repelling cue to anchor the neurons onto electrodes [74]. These physical features (e.g. microchannels) or chemical cues are also used to confine the neurite growth, expected to define the connections between neurons [165].

Besides functioning as physical confinement of axon growth [67–69], the optimized microchannel can boost the signal amplitudes to millivolt range (chapter 3). We also demonstrate the feasibility of utilizing the microchannel as signal enhancer on MEAs (chapter 5). To increase the ratio of number of distinguishable units to number of neurons in the network, in the present work, we propose a microwell-microchannel enhanced MEA (MWMC-MEA). It has microwells to confine the soma growth in the low-density hippocampal culture, connected by embedded microchannels, which will not only confine the axon growth but also boost the signal amplitudes on intrachannel electrodes.

6.2.2 Microwell fabrication

Microwells on MEA are usually directly micromachined by photo-lithography on bulk silicon wafer [65] or photoresist [67]. However, the costs and complexity of fabricating embedded channels with those methods are much higher than soft-lithography of PDMS.

Moreover the micromachined PDMS film can be attached to any planar MEA to form a MWMC-MEA.

Using PDMS to fabricate the microstructure layer require forming through-holes on PDMS film. Several etching and etchingless methods were developed to generate through-holes in thin PDMS membranes. With etchingless methods, the through-hole can be fabricated using an SU-8 mould pressed against a flat surface during curing [166] or spinning PDMS lower than the tallest feature height [73, 167].

However, these methods are not suitable for high-throughput fabrication, because usually there is thin PDMS film over the SU-8 feature requiring manual removal. Laser ablation of PDMS was also reported [168]. Precision wet chemical etching of PDMS has proven difficult and resulted in high surface roughness [169]. Although precision structures can be obtained by reactive-ion etching (RIE) with CF_4/O_2 plasma [169, 170] or SiF_6/O_2 plasma [171], the etching effect on PDMS of another common gas combination CHF_3/O_2 has not been reported yet. The biocompatibility of laser ablated or RIE machined PDMS surface also remains unknown.

In the present work, 2 different fabrication methods (femtosecond laser milling and RIE with CHF_3/O_2) were tested. The biocompatibility of micromachined PDMS surfaces was assayed with the dissociated hippocampal culture. An optimal microwell diameter of 120 µm for low-density culture was determined experimentally. The RIE method was chosen to fabricate microwell layer for MWMC-MEA. A prototype of MWMC-MEA was successfully assembled, through which the neuron activity with the maximum SNR of 142 was obtained.

6.3 Methods

6.3.1 Fabrication of SU-8 insulated MEA with microchannels

A 100-nm-thick ITO layer on the glass substrate protected by a photo-patterned photoresist layer (SPR220-1.2) was etched at 50°C with mixed acids (HCl: 14.5%, HNO_3: 6.3%) to form electrodes. (figure 6.1 (a-c))

Then SU-8 2000.5 was spun onto the patterned ITO layer at 2000 rpm, resulting in a 1-µm-thick insulation layer (figure 6.1 (d)). This insulation layer was photo-patterned in a mask aligner (MJB4, SUSS Microtec) under chrome masks to form microchannels and 20-µm-by-20-µm recording sites of ITO electrodes (figure 6.1 (e-h)).

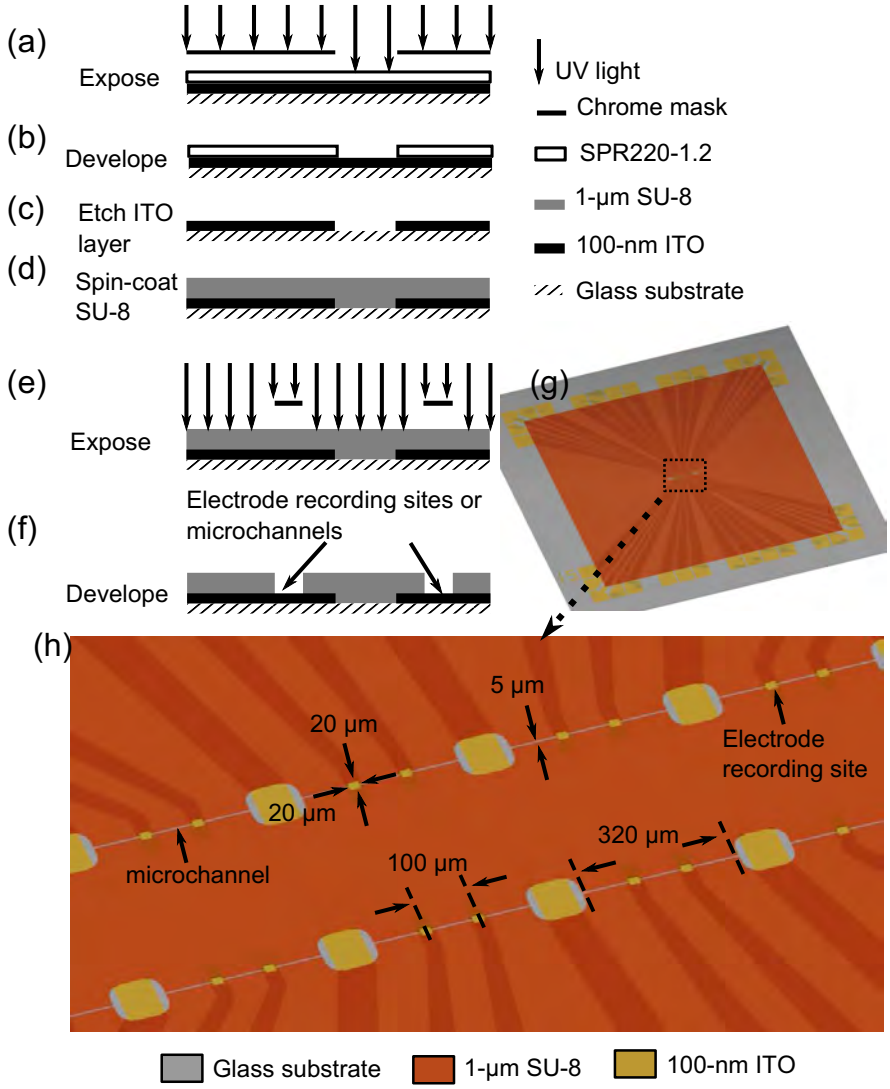

Figure 6.1. Fabrication of SU-8 insulated MEA with microchannels. (a-b) Photoresist (SPR220) was photo-patterned. (c) After forming ITO electrodes and leads by etching, photoresist was removed (d) 1-μm-thick SU-8 was spun onto the patterned surface (e-f) The electrode recording sites and microchannels were formed by photo-patterning SU-8 layer. (g) The resulted MEA. (h) Magnified central area of the MEA.

Before culturing, the MEA was cleaned using oxygen plasma for 15 mins in a PDC-002 plasma oven (Harrick Scientific) to enhance hydrophilicity.

6.3.2 PDMS mixture preparation

The PDMS mixture was prepared by mixing the curing agent and the elastomer (Sylgard 184 elastomer) in a ratio of 10:1 by weight of elastomer:curing agent.

6.3.3 Reactive-ion etch rate optimizing

The fresh PDMS mixture was spun onto glass slides at 3000 rpm and cured at 80°C for 2 hour to form 40-µm-thick PDMS film. A 1-mm-thick PDMS slab was cut into small pieces around 3-mm-by-6-mm. The small pieces was stick to the thin PDMS film to protect the area underneath from RIE (figure 6.2 (a)).

Each sample was etched in Plasmalab 80 (Oxford Instruments) at a power of 250 W, 300 mTorr of pressure, varied CHF_3 and O_2 flow for 10 mins (figure 6.2 (a-b)). Then the surface topography was characterized with an optical profiler (Wyko NT1100, Veeco), after the protection pieces were removed from the PDMS film (figure 6.2 (c)).

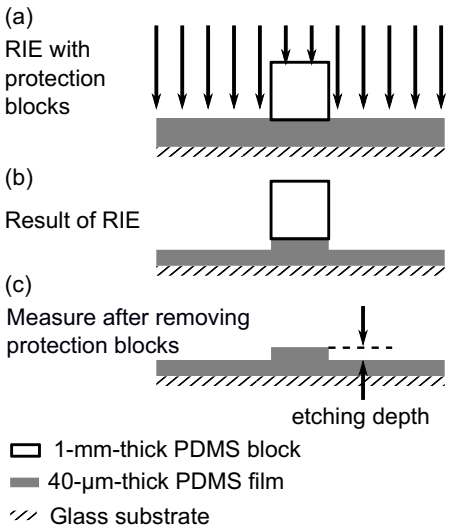

Figure 6.2. Etch rate evaluation procedure. (a) The thin 40-µm-thick PDMS film is etched in RF plasma. Random chosen areas are protected by 1-mm-thick PDMS blocks. (b-c) After 10 mins RIE, the protection blocks are removed. The etch depth can then be analyzed.

6.3.4 Fabrication of through-holes in the PDMS film

6.3.4.1 Laser drilling

45-μm-diameter and 95-μm-diameter through-hole array with 200-μm-pitch was laser-drilled on the 50-μm-thick PDMS film by commercial laser-micromachining services (Laser Micromachining Limited, OpTIC Technium, UK)

6.3.4.2 Soft-lithography combined with RIE

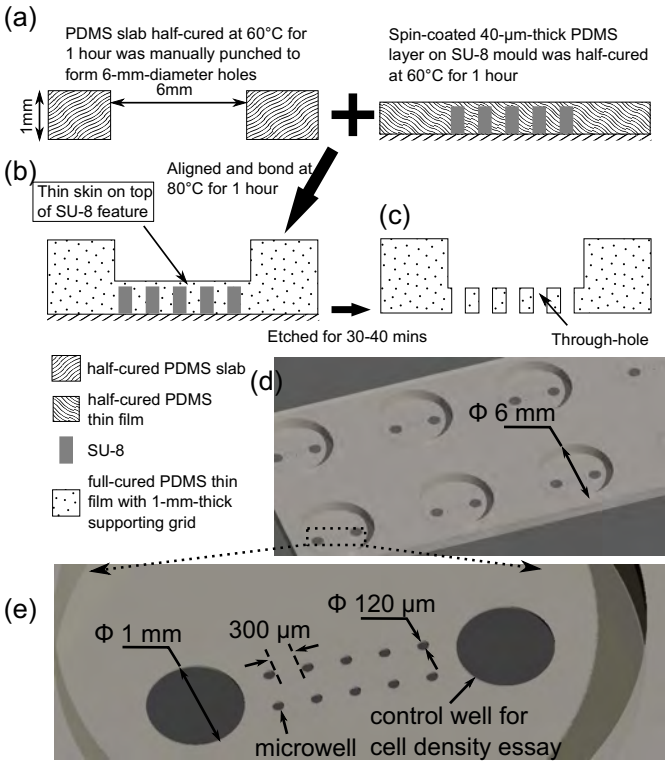

Figure 6.3. The through-hole fabrication by soft lithography combined with RIE. (a) A half-cured PDMS slab is punched to form the array of 6-mm-diameter holes. This slab is aligned to the half-cured thin film as a mechanic supporting grid. (b) The structure is cured at 80°C for 1 hour to bind the supporting grid and thin film. (c) The thin skin on top of SU-8 features is removed by RIE to create through-holes. (d) The resulted PDMS structure. (e) The magnified dashed area in (d).

40-μm-thick SU-8 layer spin-coated onto glass substrates were photo-patterned to form PDMS mould. Thicknesses and SU-8 feature geometry were then confirmed with an optical profiler (Wyko NT1100, Veeco) in vertical scanning interferometry (VSI) mode.

The fresh PDMS mixture was spun onto the SU-8 mould at 3000 rpm. Then half-cured at 60°C for 1 hour to form the thin PDMS film (figure 6.3 (a)). Another portion of PDMS mixture was poured onto a flat surface and half-cured at 60°C for 1 hour, then punched manually to form 6-mm-diameter through-hole array on a 2-mm-thick PDMS slab (figure 6.3 (a)). Then this half-cured PDMS slab as a supporting grid was aligned and bonded to the half-cured thin PDMS film on the mould by curing at 80°C for 1 hour to ease the mould-release and sequential manipulations (figure 6.3 (b)).

The PDMS film with supporting grid was then etched for 30-40 mins to remove the thin skin on top of the SU-8 features to create through-holes (figure 6.3 (c-e)).

6.3.5 Assembling of microwell-microchannel enhanced MEA (MWMC-MEA)

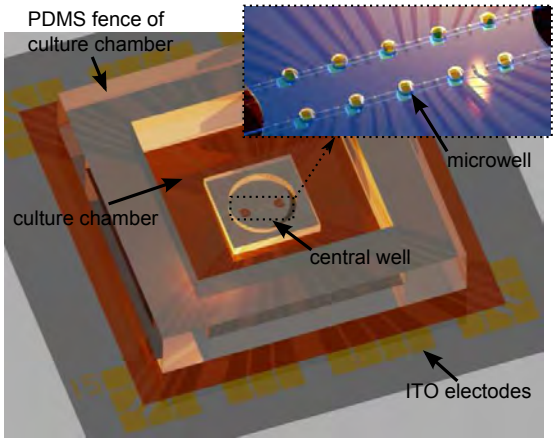

Figure 6.4. 3D schematic illustration of an assembled MWMC-MEA

The etched PDMS film with supporting grid was cut into 1-cm-by-1-cm chips. Each chip contains a through-hole array within a 6-mm-diameter central well (figure 6.4). All chips were autoclaved for 45 mins and dried under laminar flow for 2 hours.

Assembling method I:

The autoclaved and dried PDMS chips were aligned to the MEAs cleaned using oxygen plasma. After the microchannels are primed by CO_2. The entire MEA are coated with 0.1% poly-L-lysine (PLL) solution for 12 hours. After the MEAs being resined and dried under laminar flow, they were stored in 4°C for future usage.

Assembling method II:

Before assembling, the MEAs were cleaned using oxygen plasma and coated with 0.1% poly-L-lysine (PLL) solution for 12 hours. After the MEAs were rinsed and dried under laminar flow, the autoclaved and dried PDMS chips were aligned to the MEAs.

Before cell plating, an autoclaved 7-mm-high PDMS fence was attached to either version of MWMC-MEAs to form culture chamber on the MEA (figure 6.4).

6.3.6 Cell culture and electrophysiology

Dissociated cultures of mouse hippocampus neurons were prepared as described previously [106].

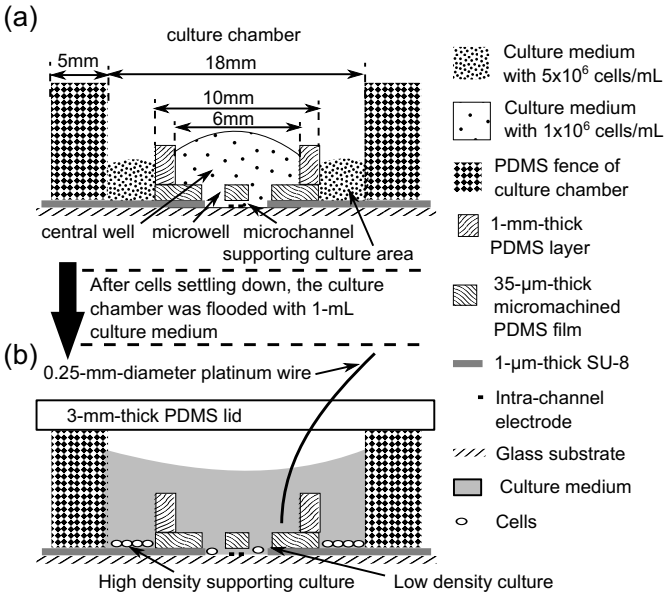

Figure 6.5. Cell plating procedure. (a) A drop (from 7 to 20 µL) of medium with low cell concentration (1×10^6 cells/mL) is plated in the 6-mm-diameter, 1-mm-high central well; 0.1 mL of medium with high cell concentration (5×10^6 cells/mL) is plated outside the central well (supporting culture area). (b) After the cells settling down, the culture chamber is flooded with 1 mL culture medium. A 3-mm-thick PDMS lid seals the culture chamber to slow down the water evaporation. A platinum wire sticks through the PDMS lid as a reference electrode.

After the microwells and microchannels (if there is any) being filled with culture medium by the CO_2 priming (chapter 2), a drop (from 7 to 20 µL) of medium with low cell concentration (1×10^6 cells/mL) were plated in the 6-mm-diameter, 1-mm-high central well; 0.1 mL of medium with high cell concentration (5×10^6 cells/mL) was plated outside the central well (supporting culture area). All manipulations should be gentle

to avoid connecting the liquid in central well and the liquid in supporting culture area (figure 6.5 (a)).

The devices rested in humidified incubator (37°C, 5% CO_2) for 6-8 hours to allow the cells to settle down. Then the culture chamber was flooded with 1 mL culture medium. A 3-mm-thick PDMS lid sealed the culture chamber to slow down the water evaporation. A platinum wire stuck through the PDMS lid contacting with culture medium to provide electrical reference. After 5 days in the humidified incubator, 1 µL of 1 mM Ara-C was applied into the culture medium, resulting in around 1 µM Ara-C concentration to suppress the glial proliferation. (figure 6.5 (b))

MEAs were loaded into multichannel amplifier (Multichannel Systems, MEA1060-Inv-BC) and recorded in a dry incubator (37°C, 5% CO_2).The data were analyzed according to previously described procedures (chapter 3) to detect and sort the spikes. SNR was calculated via dividing the positive peak value by the RMS noise.

6.3.7 Immunohistochemistry

Cells cultured on MEAs were fixed at room temperature for 30 mins with 4% formaldehyde + 4% sucrose in PBS, permeabilized with 0.1% Triton-X (Sigma; 23472-9) in PBS, and blocked with 1% goat serum (Invitrogen; PCN5000) in PBS for 1-2 hours. The cells were incubated in the primary antibodies overnight and then in the secondary antibodies for 6 hours. Following each incubation step, samples were washed with PBS for 6 hours to reduce non-specific labelling. The following primary antibodies were used: mouse anti-β-III-isoform-tubulin monoclonal (1:500; Millipore; MAB1637), rabbit anti-MAP2 polyclonal (1:500; Millipore; AB5622). As secondary antibodies, we used: anti-mouse-IgG conjugated Alexa Fluor 488 (Invitrogen; A21202) and anti-rabbit-IgG conjugated Alexa Fluor 555 (Invitrogen; A31572).

After mounting with Fluoramount (F4680 Sigma), the cells were imaged under a Leica SP1 confocal microscope, with excitation wavelengths of 488nm and 543nm, and emission filters: BP 500-548nm for Alexa 488 and BP 561-618nm for Alexa 555.

6.4 Results

6.4.1 Laser-micromachining results of the PDMS film

45-µm-diameter, 200-µm-pitch through-hole arrays and 95-µm-diameter, 200-µm-pitch through-hole arrays were fabricated by the femtosecond laser on 50-µm-thick PDMS

films. Unlike soft lithography and reactive ion etching, there is no fabrication of mould or protection layer involved in direct laser drilling. Thus it can provide a much faster prototyping speed with descent geometry accuracy. However, the debris induced by the laser ablating accumulated around fabricated holes on the PDMS surface, compromising the optical transparency of PDMS film (figure 6.6). The debris contamination is more serious in 95-μm-diameter-hole samples than in 45-μm-diameter-hole samples. This may attributed to that more materials need to be ablated for 95-μm-diameter holes.

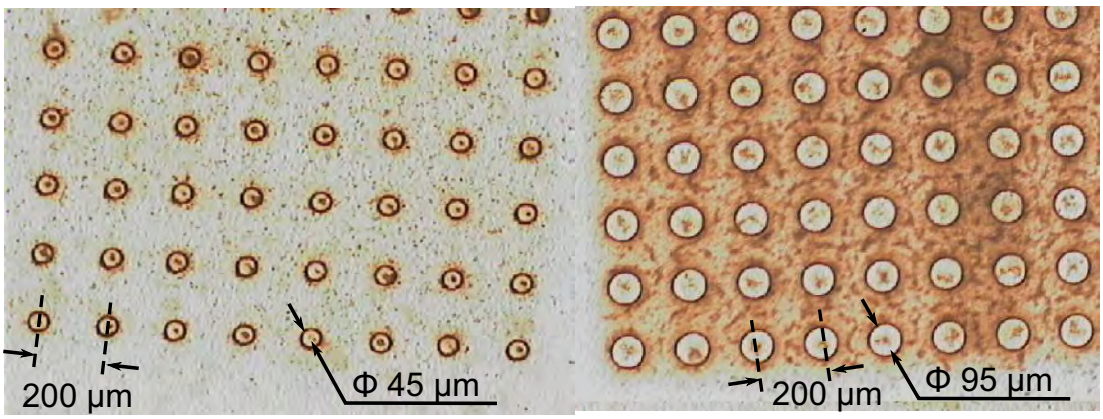

Figure 6.6. Laser-drilled through-hole array on the PDMS film. Much more debris adhered onto the PDMS surface after drilling 95-μm-diameter holes (b) than after drilling 45-μm-diameter holes (a).

6.4.2 Fabricate through holes on the PDMS film by soft lithography combined with the reactive ion etching (RIE)

Although using soft lithography combined with reactive ion etching is more complicated than the laser milling, the high-throughput potency and lower cost per device of this technique is attractive for fabricating dispensable cell culture devices. Using CF_4/O_2 plasma or SiF_6/O_2 plasma to etch PDMS has been reported. However, the etch speed and etched surface quality of another common gas combination, CHF_3/O_2 plasma, has not been explored yet. The bio-compatibility of PDMS surface machined by RIE also remains unknown. In this present work we report that CHF_3/O_2 plasma can etch the PDMS 18 μm/hour (table 6.2), with relatively smooth resulted surface and hospitable to growing neurons.

6.4.2.1 Soft lithography of PDMS films

At low spinning speed (1500-2000 rpm), the thicknesses of coated PDMS films are larger than the feature height and almost homogeneous over the entire SU-8 structure

(figure 6.7 (a)). At faster spinning speed (2400-3000 rpm) the thicknesses of PDMS films are smaller than the feature height; and the thickness of the PDMS skin on top of SU-8 pillars depends on the feature size (figure 6.7 (b), table 6.1). The skin is usually thicker on 1-mm-diameter pillars than on 0.12-mm-diameter pillars.

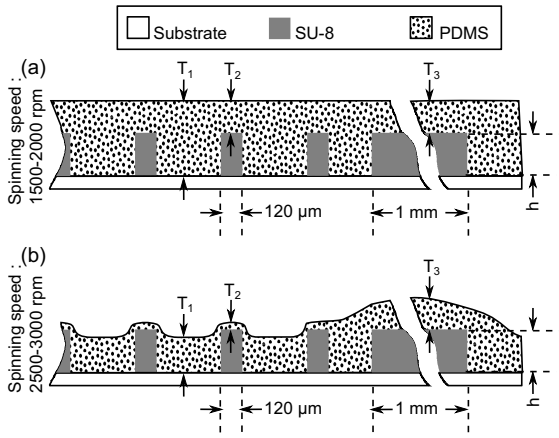

Figure 6.7. Illustration of the vertical profile of PDMS film spun onto the SU-8 master. h represents SU-8 feature height (40-41.3 µm). T_1 is the PDMS thickness where is no SU-8 feature. T_2 is the PDMS skin thickness on top of 120-µm-diameter pillars. T_3 is the thickness on top of 1-mm-diameter pillars. T_1, T_2 and T_3 were reported in table 6.1. (a) Spin-coating PDMS at low speed (1500-2000 rpm) results in a homogeneous distribution of thickness over the SU-8 structures. (b) Spin-coating PDMS at high speed (2500-3000 rpm) results in an inhomogeneous distribution of thickness over the SU-8 structures. The skin covering large SU-8 features is thicker than covering small features.

Table 6.1: The dependence of film thickness at different locations on spinning speed.

Spinning speed (rpm)	T_1 [a] (µm)	T_2 [b] (µm)	T_3 [c] (µm)
1500	94.6-97.1	54.6-55.1	54.4-56.1
2000	69.2-71.0	31.5-32.3	32-33
2500	38.2-39.5	12.8-14.8	16.0-17.5
3000	36.1-38.3	4.7-8.1	11-17

[a] T_1 is the PDMS thickness where is no SU-8 feature.
[b] T_2 is the PDMS skin thickness on top of 120-µm-diameter pillars.
[c] T_3 is the PDMS skin thickness on top of 1-mm-diameter feature.

Both the skin thickness and the PDMS film thickness decreased with increasing spinning speed. Considering the trade-off between the required etching depth and the film thickness, 3000-rpm spinning speed was chosen for the microwell fabrication.

6.4.2.2 RIE of the PDMS film

Table 6.2: The etch rates of PDMS when etched with various ratios of CHF_3 to O_2 flow.

CHF_3 flow rate (sccm)	O_2 flow rate (sccm)	Etch rate (μm/min)
25	13	0.18-0.19
13	25	0.16-0.23
25	25	0.24-0.31

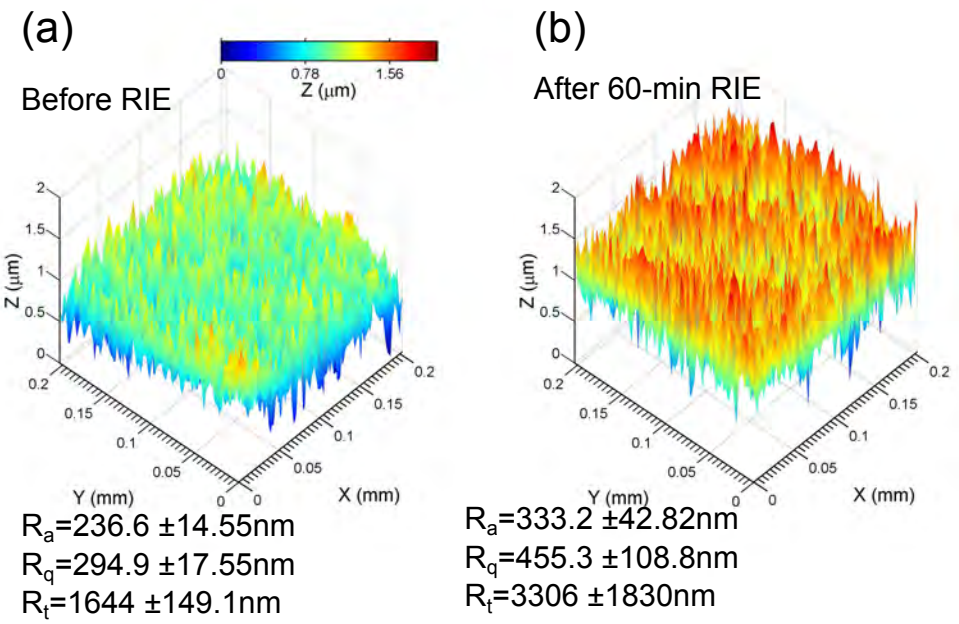

Figure 6.8. The surface topography and roughness of the reactive-ion-etched PDMS. Colours represent the heights (Z). 3 parameters were used to report the surface roughness: the arithmetic average of absolute values (R_a), root mean squared value (R_q), and the maximum height of the profile (R_t). (a) Before reactive-ion etching (RIE). (b) After 60-min RIE, the surface roughness increased.

To optimize the etch rate, 3 different combinations of CHF_3 flow and O_2 flow were assayed (table 6.2). The combination of 25 sccm CHF_3 and 25 sccm O_2 yield the highest

etch rate of 0.24-0.31 μm/min, which is similar to the etch rate with CF_4/O_2 plasma [170]. If not mentioned in following paragraphs, the gas flow is always 25 sccm CHF_3 plus 25 sccm O_2.

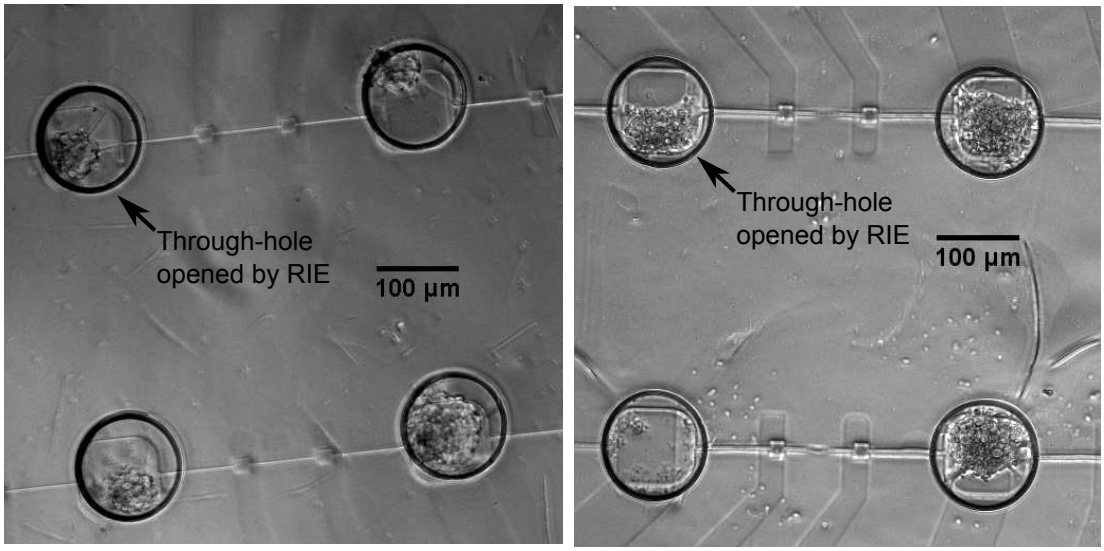

Figure 6.9. Neuronal culture in through-holes opened by RIE. The PDMS surface and the microwell orifice are much smoother than the laser-milled one.

Figure 6.8 compared the surface roughness before and after 60 mins RIE. After 30 mins RIE, the surface roughness did not show obvious difference to the unetched PDMS surface. Although 60 mins RIE led to ∼40% increase in the arithmetic average of surface roughness (R_a), there is no obvious deterioration in the optical transparency of PDMS films (figure 6.9), in contrast to the laser-drilled one (figure 6.6 and 6.11).

After 15 mins RIE, less than 50% of holes were opened (figure (a)). After 30 mins RIE, more than 90% of holes were opened; and the film thickness remained around 30 μm (figure (b)). After 60 mins RIE, more holes were opened, but the film thickness was reduced to less than 30 μm. To confine the cell growth, the thicker film the better. Thus 30-min etching time was chosen to balance the film thickness and the yield rate.

6.4.3 Cell viability assay of low density culture in microwells

The native PDMS film show strong cytotoxicity: almost no living neuron can survived in microwells (figure 6.11 (a)), when plated at 20×10^3 cells per device (709 cells/mm^2). This may be attributed to the platinum catalyst contained in native cured PDMS [172,

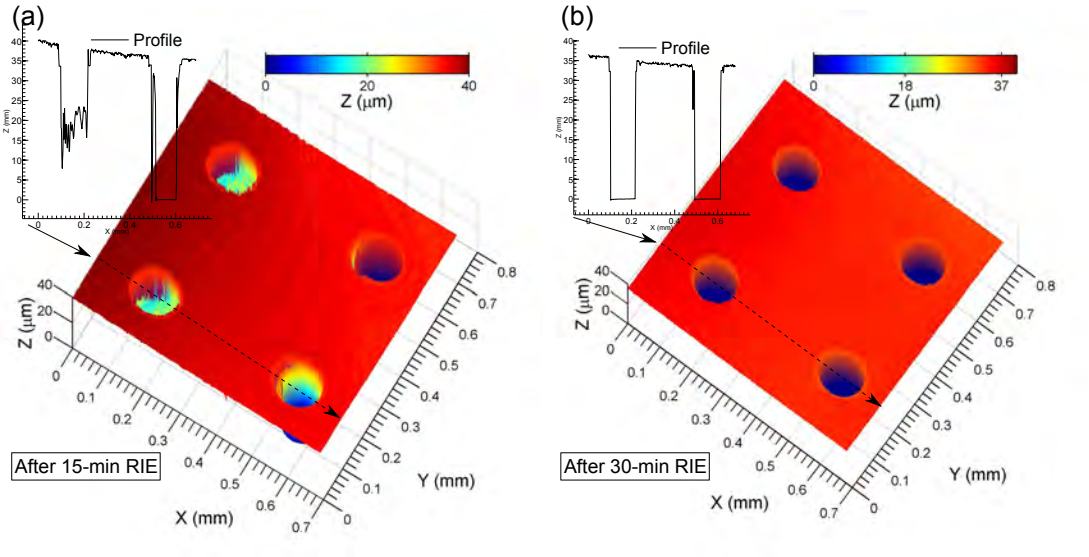

Figure 6.10. The surface topography of reactive-ion-etched PDMS film moulded with SU-8 pillars. Colours represent the heights relative to the substrate surface. Insets are the profiles along the dashed arrows. (a) A film was etched for 15 mins. Only two holes were opened. Due to the curvature of the thin skin covering the blind holes, the heights of these skins are measured 10-20 μm lower than the top surface. (b) A film was etched for 30 mins. Because all holes were opened that there was no skin covering any hole.

173]. Autoclaving process was reported to be effective for removing platinum from PDMS. Thus in following viability assays, all PDMS devices were autoclaved for 45-60 mins.

To assay the viability of neurons in microwells of autoclaved PDMS films, dissociated mouse hippocampal neurons were plated at 7×10^3 cells per device (248 cells/mm^2, or 1.76 cells/microwell). The results are summarized in table 6.3.

On the PLL coated polystyrene surface, there were respectively 114 neurons/mm^2 and 157 neurons/mm^2 (averagely 135 neurons/mm^2) survived in 1-mm-diameter wells in 2 different test rounds, after 1 week in humidified incubator. The average viability is about 54.4%. The 95-μm-diameter microwells contained 0-6 neurons/well, averagely 1.04 neurons/well. The average viability is about 59.1%, similar to the viability estimated from the 1-mm-diameter wells. There were 37% microwells and 40% microwells containing living neurons. However living cells in 45-μm-diameter wells were too rare to be observed (figure 6.11 (b)).

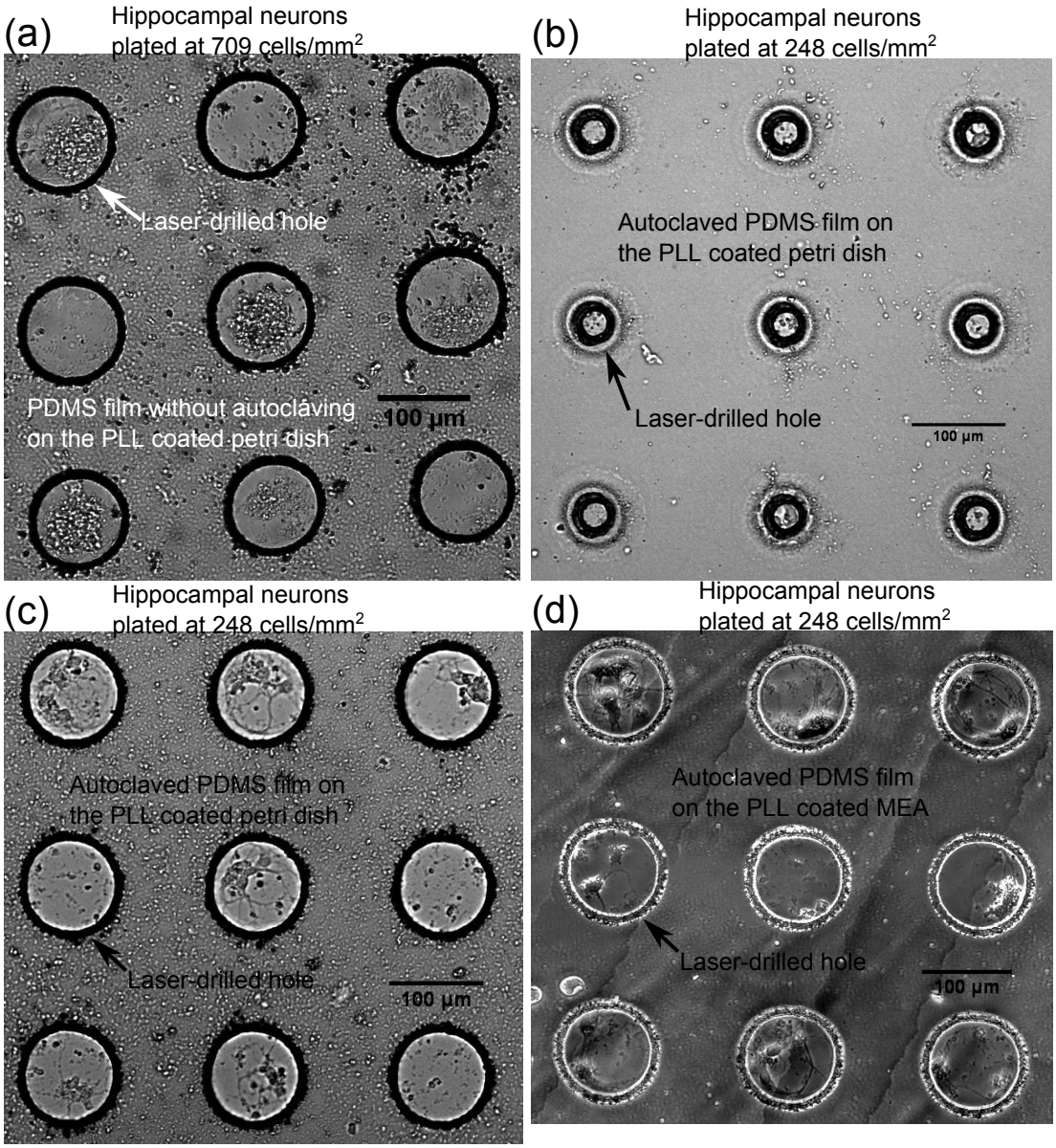

Figure 6.11. Viability assay of neuron growth in microwells of PDMS film on polystyrene Petri dishes and MEAs. Only autoclaved PDMS film with large microwells (95-µm diameter) can support the neuron growth.

Table 6.3: Neuronal viability tests of the low-density hippocampal culture plated at 248 cells/mm^2.

Substrate	Viability	Viable cells/well
45-μm-diameter microwell on Petri dish	0%	0
95-μm-diameter microwell on Petri dish	59.1%	1.04
120-μm-diameter microwell on MEA	29.0%	0.8
Petri dish surface	54.4%	-
MEA surface (SiO_2, SU-8 and ITO)	30.1%	-
Dry etched PDMS surface	23.0%	-

The neuron viability of 30.1% on the PLL coated MEA surface, was lower than that on polystyrene surface: there were 66-82 neurons/mm^2 averagely 74.7 neurons/mm^2 (N = 3, SD = 7.8) survived after 1 week. On the PLL coated MEA surface, the cells intend to aggregate. Thus it is difficult to determine how many neurons survived in 95-μm-diameter microwells (figure 6.11 (d)). Averagely 0.53 neurons/microwell can be estimated from the viability obtained in 1-mm-diameter wells. Hence, to achieve similar number of living neurons per microwell on MEAs as on Petri dishes, a larger diameter from 120-130 μm is required (0.85-1 neurons/microwell).

6.4.4 Neuronal culture on PDMS surface machined by RIE

To assay the bio-compatibility of the reactive-ion-etched PDMS surface, the PDMS film moulded by SU-8 master (spun at 3000 rpm and cured at 80°C) was etched for 30 mins to open through holes. Then the autoclaved PDMS film was coated by 0.1% poly-L-lysine (pH = 8.5, at 4°C overnight). Dissociated mouse hippocampus neurons were plated at 248 cells/mm^2. After 14 days, the neurons were identified by anti-β-III-tubulin (green in figure 6.12) and anti-MAP2 (red in figure 6.12) antibodies.

There were 57 neurons/mm^2 survived on the PDMS surface machined by RIE. Although the viability of 23% is lower than the average viability of 54.4% on the polystyrene surface, it is still comparable to the average viability of 30.1% on the MEA surface. Hence the RIE process is compatible with the low-density neuronal culture. Even higher viability can be expected if cytotoxins in native PDMS, e.g. uncrosslinked oligomers, are extracted through soaking/swelling PDMS in a series of organic solvent [173] or the

Sylgard 184 PDMS is replaced by other medical grade PDMS.

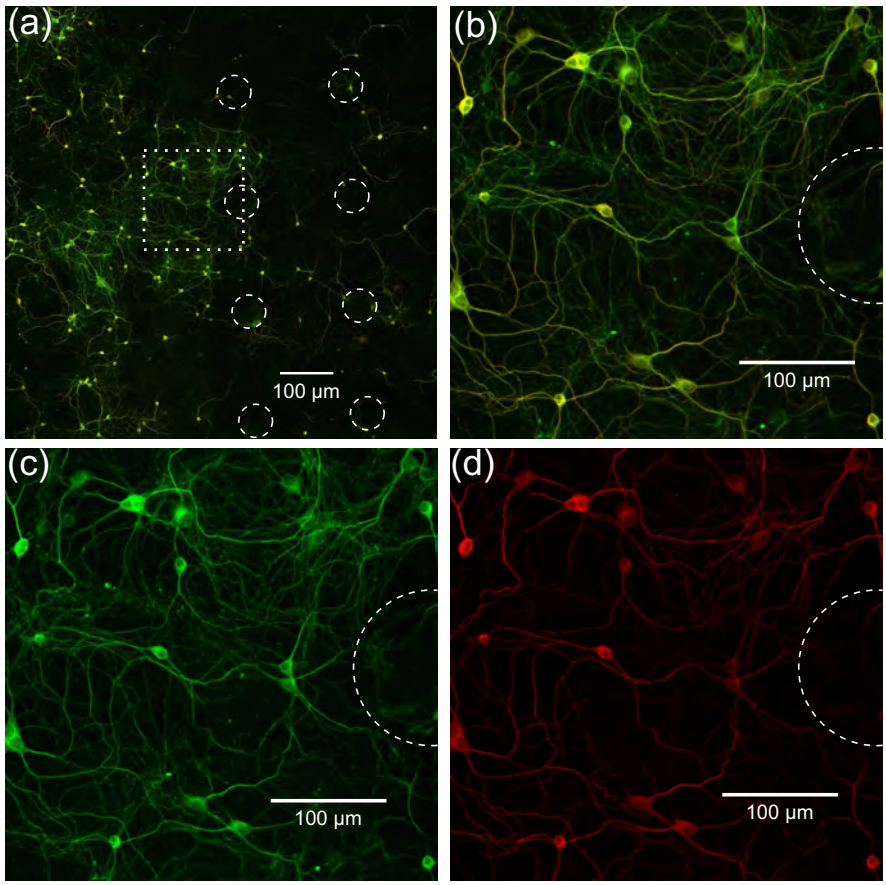

Figure 6.12. Neuron growth on the PDMS surface reactive-ion etched for 30 mins. The dashed lines show the orifices of the microwells. (a) Neurons were labelled by anti-MAP2 (red) and anti-β-III-tubulin (green) antibodies. The dendrites were identified by anti-MAP2 antibodies (red). (b) Magnification of dotted area in (a). (c-d) Split colour channels in (b).

6.4.5 Recordings of MWMC-MEA with poly-L-lysine (PLL) coating on PDMS

In this section the MWMC-MEA is assembled by method I: the poly-L-lysine was applied onto the MEA after PDMS layer aligned to electrodes. Thus there are PLL layer on the PDMS surface, which can support cell growth. The dissociated mouse hippocampus neurons were plated at 248 cells/mm^2. At 5 DIV, 1 µM (final concentration) Ara-C was applied into cell cultures to suppress glia proliferation.

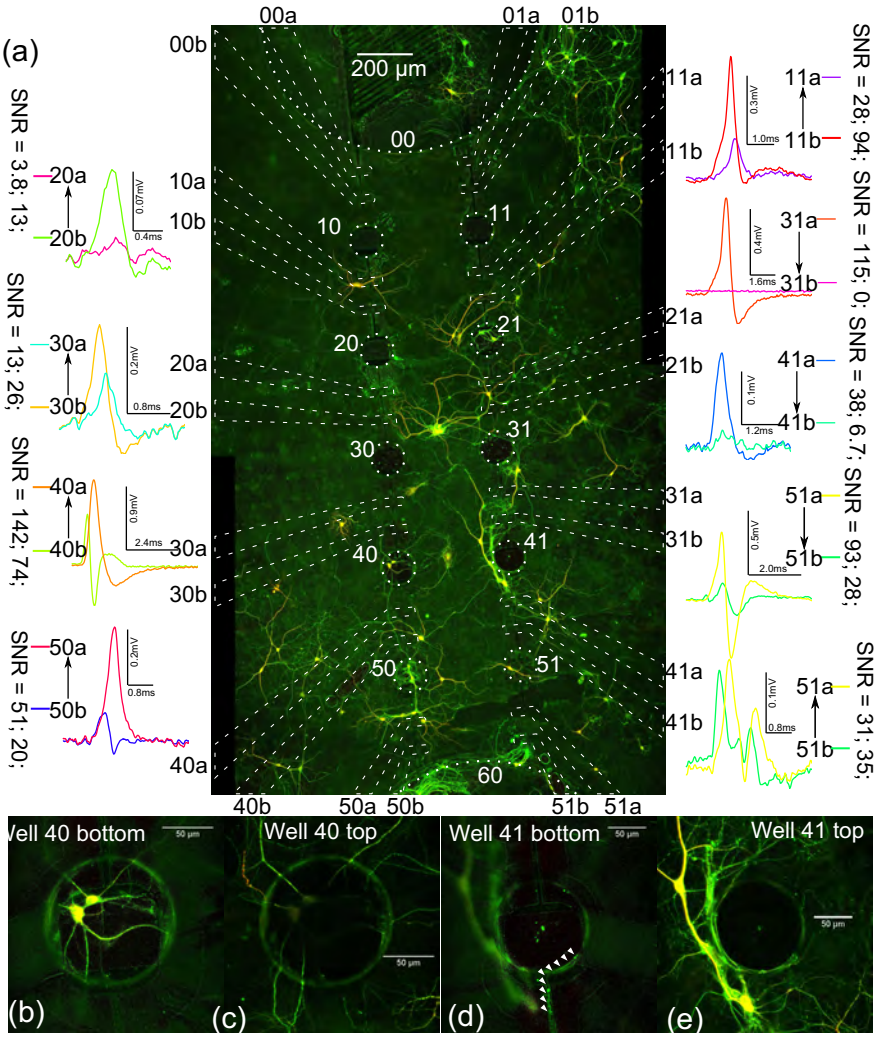

Figure 6.13. (a) Maximum projection of the confocal images and example raw signal traces of low-density dissociate hippocampal culture on MWMC-MEA with poly-L-lysine (PLL) coated PDMS surface at 14 DIV. The dotted lines show the positions of microwell orifices. The dashed lines show the position of ITO electrodes. Neurons were labelled by anti-MAP2 (red) and anti-β-III-tubulin (green) antibodies. The wells are labelled by number in form of 'NM'. N (0-6) is the row number; M (0-1) is the column number. The intrachannel electrodes are labelled by number in form of 'nms': n (0-5) is the row number of microchannels; m (0-1) is the column number of microchannels; s (a or b) identifies each electrode in each microchannel. The colours in raw signal traces identify the electrodes. The arrow between electrode labels show s the signal propagation direction. Bottom panels (b-e) are magnified image of well 40 and well 41. Optical slices with height from 0 to 25 µm were maximum projected to generate the bottom view; optical slices with height from 25-60 µm were maximum projected to generate the top view. (d) A MAP2-negative, β-III-tubulin-positive neurite was identified by arrow heads.

After 14 days, there are 14 viable neurons/mm^2 in the microwell area (the entire area in figure 6.13 (a)). In total 32 neurons were identified within 0.3 mm of microwells. 8 cells were inside microwells, 0.8 neurons/well, which is very close to the viability of 0.85 neurons/well for 0.12-mm-diameter microwells estimated in previous viability assay. 4 wells contain neuronal somata: well 21 (2 somata), well 40 (2 somata), well 50 (3 somata), and well 51 (1 soma). Axons projected from neurons outside the microwells were also observed in some microchannels, e.g. well 41 (figure 6.13 (d) the arrowed green neurite in the magnification of well 41 bottom).

Figure 6.13 (a) also shows the raw signal traces (without any digital filtering or averaging) obtained from the intrachannel electrodes. Each spike was recorded by 2 electrodes in the same microchannel, one with larger amplitude and the other with smaller amplitude. The signal delay on those two electrodes indicates the direction of the AP propagation. For example, one of the two units in channel 51 showed in figure 6.13, has positive time delay from electrode a to electrode b, indicating this unit propagating from well 51 to well 60. The other unit in channel 51 propagated in the opposite direction. The RMS noise on intrachannel electrodes is typically 5 μV, similar to the classic planar MEA (2-3 μV). As expected, the SNR from 13 to 142, averagely 67, was obtained from this MWMC-MEA, relatively large comparing to classic planar MEA.

8 out of 12 microchannels have distinguishable spike units. At least 7 different units originated from microwells were recorded, about 22% neurons within 0.3 mm range of microwells (the units from 50b→50a and 51b→51a do not account, because they are originated in the 1-mm-diameter control well). Conceivably, higher ratio of number of distinguishable units to number of neurons can be expected, if the cell growth on the PDMS surface were suppressed.

6.4.6 Recordings of MWMC-MEA without poly-L-lysine (PLL) coating on PDMS

To suppress the cell growth on the PDMS surface, a MWMC-MEA was assembled by method II: the micromachined PDMS film were aligned to the MEA already coated with PLL. The dissociated mouse hippocampus neurons were plated at 742 cells/mm^2. In 1-mm-diameter control well, 962 cells/mm^2 were counted, about 11 cells/microwell. At 5 DIV, 1 μM (final concentration) Ara-C was applied into cell cultures to suppress glia proliferation. After 14 days, no viable glia or neuron was observed on the PDMS surface (figure 6.14 (b)).

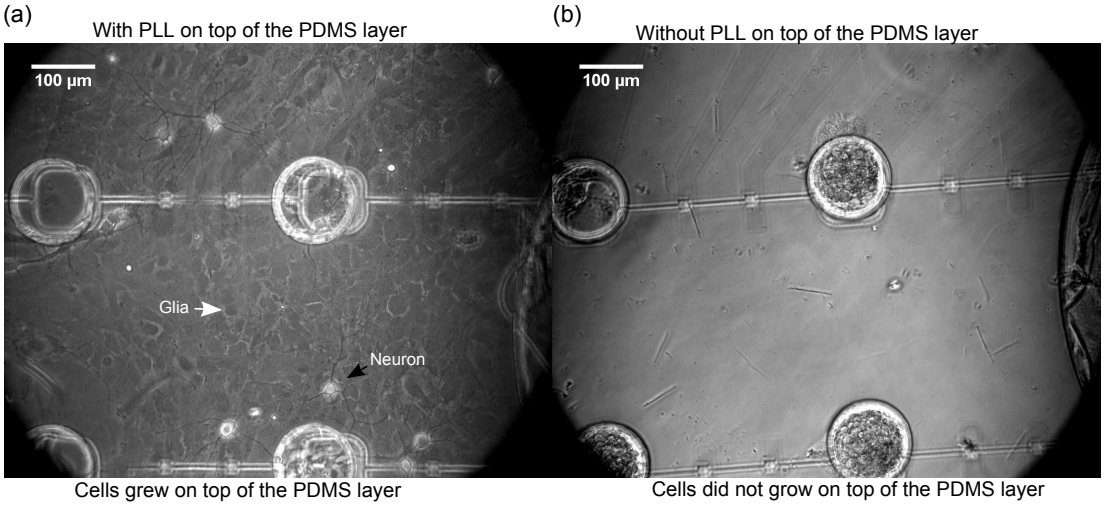

Figure 6.14. The cell growth on top of the PDMS layer. The poly-L-lysine (PLL) coating on the PDMS surface can support glial (white arrow) and neuronal (black arrow) growth. The uncoated PDMS surface cannot. 1 µM Ara-C was applied in both cultures at 5 DIV to suppress glial proliferation.

Figure 6.15 shows the raw traces (without any digital filtering or averaging) obtained from the intrachannel electrodes at 10 DIV. The SNR was from 9.7 to 112, averagely 45.

11 out of 12 microchannels have distinguishable spike units. At least 20 different units originated from microwells were recorded. It is difficult to determine how many viable neurons in each microwell. But an average value of 3.3 neurons/microwell was estimated from the viability of 30% obtained in the previous viability assay section. Thus the ratio of number of distinguishable units to number of neurons is around 61%.

6.5 Discussion and conclusions

In the present work, a prototype designed based on previously obtained dependence of signal amplitudes on channel geometry and intrachannel electrode position (part I). In this prototype, ten 120-µm-diameter microwells were connected by 0.3-mm-long, 5-µm-wide, 1-µm-high microchannels; for each microchannel, two 20-µm-wide ITO electrodes were placed 0.1 mm to the nearest channel entrance. ITO electrodes were formed by etching the ITO layer on the glass substrate and insulated by a 1-µm-thick SU-8 layer. Microchannels were created by photolithography of this SU-8 insulation layer on the MEA. A piece of 30-µm-thick PDMS film with 120-µm-diameter through-holes was aligned to the MEA to form microwells and the ceiling of microchannels.

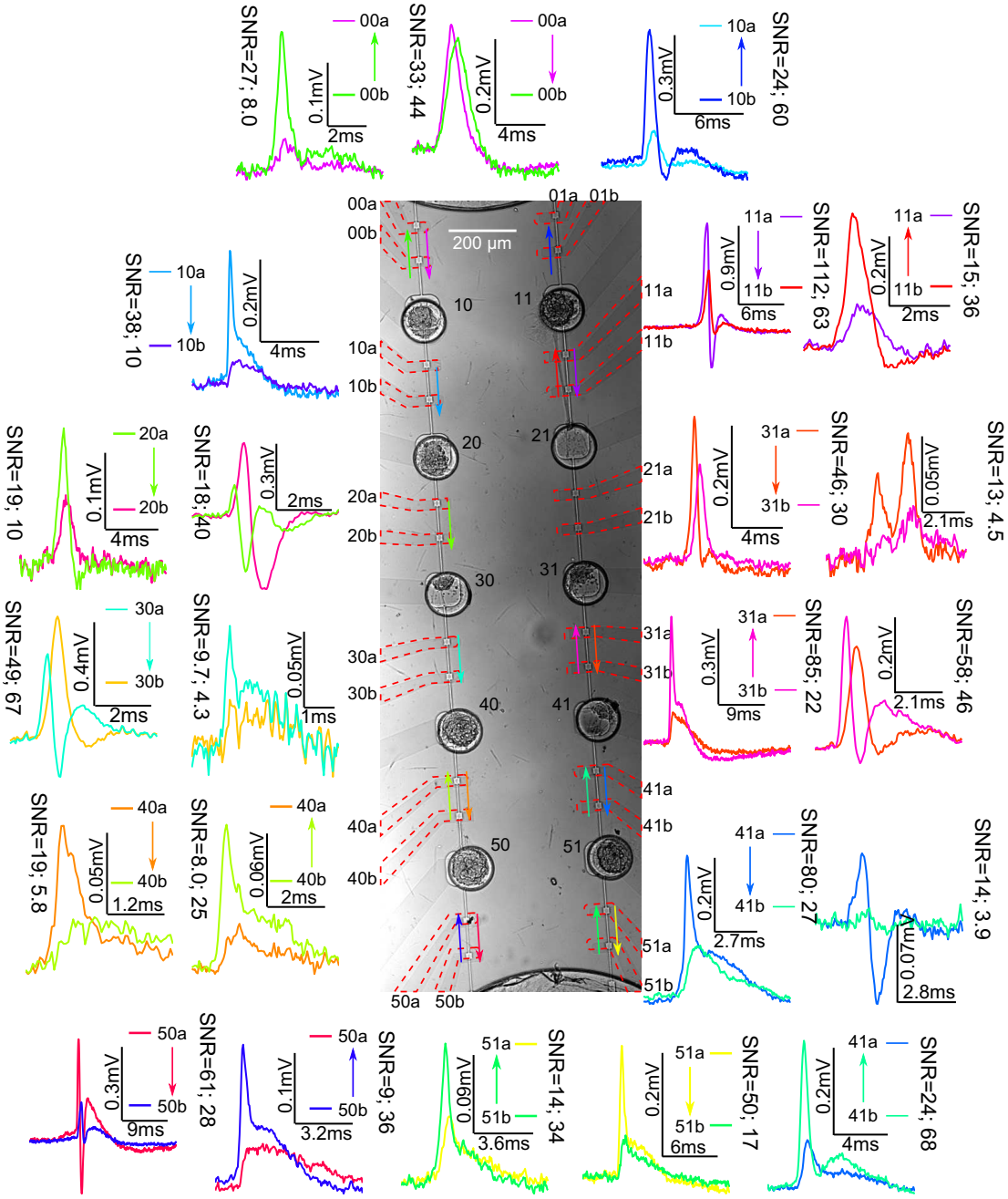

Figure 6.15. (a) Phase-contrast images and example raw signal traces of low-density dissociate hippocampal culture at 10 DIV, on MWMC-MEA without poly-L-lysine coating on PDMS. The dashed lines show the position of ITO electrodes. The wells are labelled by number in form of 'NM': N (0-6) is the row number; M (0-1) is the column number. The intrachannel electrodes are labelled by number in form of 'nms': n (0-5) is the row number of microchannels; m (0-1) is the column number of microchannels; s (a or b) identifies each electrode in each microchannel. The colours in raw signal traces identify the electrodes. The coloured arrow between each pair of electrode labels shows the signal propagation direction. The coloured arrows on phase-contrast images summarise the signal propagation direction of signals recorded from each microchannel.

6. MICROWELL-MICROCHANNEL ENHANCED MULTI-ELECTRODE ARRAY FOR LOW-DENSITY DISSOCIATED HIPPOCAMPAL CULTURE, PART II: FABRICATION AND RECORDINGS

Two methods were examined for fabricating through-holes in the PDMS film: laser ablation and soft-lithography combined with RIE of the CHF_3/O_2 plasma. For large holes (diameter $\geq$ 95 μm), the laser ablation compromises the optical transparency of the PDMS film, although it can provide a much faster prototyping speed. Thus it is not suitable for MWMC-MEA fabrication, comparing to soft-lithography combined with RIE. An etch rate of 0.3 μm/min can be achieved with 25 sccm CHF_3 and 25 sccm O_2. There is no obvious deterioration of the optical transparency after 60 mins RIE. After autoclaving, the reactive-ion etched PDMS surface was proved to be compatible with the hippocampal-neuron growth.

The low-density culture (57 neurons/mm^2) were survived on the MWMC-MEA s for at least 14 days, from which the neuronal signal with the maximum SNR of 142 was obtained. With Ara-C, the cell growth on the PDMS surface without PLL coating can be suppressed. The neurons and neurites can be confined in microwells and microchannels, resulting a relatively high ratio (61%) of number of distinguishable units to number of neurons in neuronal network.

Without Ara-C, after 5-7 days the glial cell can eventually grow onto the PDMS surface even without PLL coating. This glial layer can then facilitate neuron migration and growth of neurites on the PDMS surface. Thus a better cell repelling method should be implemented in the future work. For example a dried agarose layer can be deposit on top of the PDMS layer to suppress the cell growth on the PDMS surface, only allowing the cell to grow on the bottom MEA surface.

As we described previously (chapter 3), the high resistance caused by glial tissue clogging the microchannel is the key factor to obtain the high SNR. Thus higher SNR can be expected, if the glial proliferation is not suppressed in the microwells and microchannels. Hence a better cell repelling modification of PDMS surface allowing low-density neuronal culture without Ara-C may also improve the SNR further.

The present work is just a proof of MWMC-MEA concept. The potential of this device is beyond this demonstration. In the future work, the 1-mm-diameter control well for assaying the cell viability can be removed. More microwells and more microchannels can be added to scale up the network size without reducing the ratio of number of distinguishable units to number of neurons inside the network. Stimulation electrodes can be implemented in the microwell to control the activity of the individual neuron cluster in each microwell. More complicated inter-well connection can be defined by

placing more microchannels between microwells. Hence we conclude that the MWMC-MEA is promising for monitoring large portion of neurons in the network to facilitate understanding the mechanism of information processing in small neuronal networks in vitro.

6. MICROWELL-MICROCHANNEL ENHANCED MULTI-ELECTRODE ARRAY FOR LOW-DENSITY DISSOCIATED HIPPOCAMPAL CULTURE, PART II: FABRICATION AND RECORDINGS

Chapter 7 Conclusions

7.1 Summary of results

The PDMS microchannel can be fabricated by soft lithography with relatively **low complexity and costs** (chapter 2). To meet specific substrate requirements of different experiments or different types of neurons, the microchannel device can be attached to many kinds of flat neural culture substrates such as polystyrene Petri dish, glass coverslips, commercial or customized MEAs to form neuron-electrode interface for electrical activity monitoring.

To optimize the signal strength, we further explored the biophysics of the signal generation in the microchannel devices. Our results show that **the recorded signals are mainly caused by the transmembrane current of the membrane patches located inside the microchannel and within ~100 μm to the microchannel entrances**. A fraction of this transmembrane current flow through the high-resistivity extracellular intrachannel pathway generates a recordable voltage drop along the microchannel. The glial and neural tissue threading microchannels can increase the resistivity of the intrachannel space, thereby amplifying the signal amplitudes. Shrinking down the cross-section area of the microchannel also increases the resistance per unit length, leading to an increase of the signal amplitudes (chapter 3).

In macrowell-microchannel devices where only soma-wells are grounded, the dependence of signal amplitude on microchannel length is not monotonic, due to the phase-cancelling effect and low-pass filtering effect (chapter 3, section 3.5). For microchannels shorter than the transition length (~200-300 μm for microchannels with A_c = ~100 μm^2), the amplitude increases with increasing channel length. After the microchannel length increases beyond this transition length, the amplitude decreases with increasing channel length.

The optimal channel length for hippocampal neurons is from ~70-300 μm. **Channels with a length of ≤ 200 μm and channel cross section of ≤ 12 μm² yielded spike sizes in the millivolt range. Despite the low degree of complexity involved in their fabrication and use, microchannel devices provided a single-unit mean SNR of 101±76, which compares favourably with the SNR obtained from recent developments employing CNT-coated electrodes and Si-NWFETs.**

However, the dependence of the signal amplitudes on the channel length in embedded microchannel MEA, where the both entrances of each microchannel are grounded, is different (chapter 5, section 5.4.2): the longer the channel the stronger the signal. Considering the trade-off between fabrication yield rate and signal amplitudes, a compromise length of 300 μm was chosen to fabricate MWMC-MEAs.

The optimal position of intrachannel electrodes are 70-140 μm for hippocampal neurons (chapter 5, section 5.4.1). These optimal parameters may be different for a different type of neurons especially which have very different conduction velocity, axon diameter or ion-channel distributions, such as spinal neurons.

We demonstrate that the MWMC-MEAs can provide high SNR (maximum 142) and high ratio (~61%) of distinguishable units to total number of neurons in the network. Another advantage of MWMC-MEA is capable of determine signal propagation direction from the delay on different electrodes in the same microchannel, which may facilitate the connectivity analysis of the neuronal network.

Moreover, we also demonstrated that the microchannel threaded by glial and neural tissue can function as fluid/chemical barrier (chapter 4), because the diffusion is the dominant mass transfer mechanism in microchannels. **Chemical compounds can be applied to different subcellular compartments exclusively.** This renders it as a promising technique for high-throughput automatic ion channel screening at subcellular level. This subcellular ion channel profile can provide important information about demyelination disorders such as MS, and even learning/memory disorders.

7.2 Future work

To future improve those non-fluorescence imaging technique for neural activity, one would expect to record both the electrical and optical signals from monitored neurons

simultaneously. It is difficult to perform this on typical MEAs, because it is difficult to determine the location of the electrical signal source by typical MEAs. The origin of the electrical signals from a microchannel device is mainly the neurites inside the microchannel. That allows simultaneous optical and electrical monitoring. Because of the high flexibility in selection of culture substrate, electrode and insulation materials, it can offer many options for optical monitoring. Unlike conventional electrical interfaces, it does not contain moving parts reducing the optical noise induced by the mechanical vibration. Hence this microchannel enhanced neuron-electrode interface can also facilitate improving the non-fluorescence optical neuron-computer interfacing.

To automate and scale up the neural activity monitoring, in the future, more microchannels per culture well and a microfluidic cell-plating mechanism should be integrated. To automate and scale up the chemical compound delivering, an on-chip superfusion system can be implemented and integrated together with the microchannel devices. The microevironment sensors such as temperature, pH and osmolarity sensors can also be integrated to reduce the size of the entire system.

Publications and presentations

.1 Journal publications

- Ling Wang, Michael Riss, Jennifer Olmos Buitrago and Enric Claverol-Tinturé. Biophysics of microchannel-enabled neuron-electrode interfaces. J Neural Eng, 2011; submitted

- Ricardo Morales, Michael Riss, Ling Wang, Rosalina Gavín, Jose Antonio Del Río, Ramon Alcubilla, and Enric Claverol-Tinturé. Integrating multi-unit electrophysiology and plastic culture dishes for network neuroscience. Lab Chip, 8 (11):1896–1905, Nov 2008.

.2 Conference presentations

- Ling Wang, Michael Riss, and Enric Claverol-Tinturé. Optimizing cross-section of micro-channel for high-throughput electrophysiology 3rd IBEC Symposium on Bioengineering and Nanomedicine. 1st and 2nd of June, 2010. Flash presentation and poster.

- Ling Wang, Michael Riss, and Enric Claverol-Tinturé. Subcellular superfusing system. 2nd IBEC Symposium on Biomaterials in Regenerative Medicine. Barcelona, Spain. 14th-15th April, 2009. Flash presentation and poster.

.3 Patents

- Enric Claverol-Tinturé, Ling Wang. Procedimiento para monitorizar la evaporación de un cultivo celular. Spanish Patent Application P201000818; filed on Aug. 18, 2010.

References

[1] E.R. Kandel, J.H. Schwartz, and T.M. Jessell. *Principles of neural science*. McGraw-Hill, Health Professions Division, 2000. ISBN 9780838577011. URL http://books.google.com/books?id=yMtpAAAAMAAJ. 1

[2] B. T. Priest, A. M. Swensen, and O. B. McManus. Automated electrophysiology in drug discovery. *Curr Pharm Des*, 13(23):2325–2337, 2007. ISSN 1381-6128. 2

[3] G. Q. Bi and M. M. Poo. Synaptic modifications in cultured hippocampal neurons: dependence on spike timing, synaptic strength, and postsynaptic cell type. *J Neurosci*, 18(24):10464–10472, Dec 1998. 2

[4] Frédéric Duflo, Yong Zhang, and James C Eisenach. Electrical field stimulation to study inhibitory mechanisms in individual sensory neurons in culture. *Anesthesiology*, 100(3):740–743, Mar 2004.

[5] T. A. Good, D. O. Smith, and R. M. Murphy. Beta-amyloid peptide blocks the fast-inactivating k+ current in rat hippocampal neurons. *Biophys J*, 70(1):296–304, Jan 1996. doi: 10.1016/S0006-3495(96)79570-X. URL http://dx.doi.org/10.1016/S0006-3495(96)79570-X.

[6] Fernando Mesquita, José F Aguiar, José A Oliveira, Norberto Garcia-Cairasco, and Wamberto A Varanda. Electrophysiological properties of cultured hippocampal neurons from wistar audiogenic rats. *Brain Res Bull*, 65(2):177–183, Mar 2005. doi: 10.1016/j.brainresbull.2005.01.003. URL http://dx.doi.org/10.1016/j.brainresbull.2005.01.003.

[7] Itay Baruchi and Eshel Ben-Jacob. Functional holography of recorded neuronal networks activity. *Neuroinformatics*, 2(3):333–352, 2004. doi: 10.1385/NI:2:3:333. URL http://dx.doi.org/10.1385/NI:2:3:333. 23, 24, 92

[8] Daniel A Wagenaar, Jerome Pine, and Steve M Potter. An extremely rich repertoire of bursting patterns during the development of cortical cul-

tures. *BMC neurosci*, 7:11, 2006. doi: 10.1186/1471-2202-7-11. URL http://dx.doi.org/10.1186/1471-2202-7-11.

[9] Radhika Madhavan, Zenas C Chao, and Steve M Potter. Plasticity of recurring spatiotemporal activity patterns in cortical networks. *Phys Biol*, 4(3):181–193, Sep 2007. doi: 10.1088/1478-3975/4/3/005. URL http://dx.doi.org/10.1088/1478-3975/4/3/005. 24

[10] Daniel A Wagenaar, Radhika Madhavan, Jerome Pine, and Steve M Potter. Controlling bursting in cortical cultures with closed-loop multi-electrode stimulation. *J Neurosci*, 25(3):680–688, Jan 2005. doi: 10.1523/JNEUROSCI.4209-04.2005. URL http://dx.doi.org/10.1523/JNEUROSCI.4209-04.2005. 24, 109

[11] Douglas J Bakkum, Zenas C Chao, and Steve M Potter. Spatio-temporal electrical stimuli shape behavior of an embodied cortical network in a goal-directed learning task. *J Neural Eng*, 5(3):310–323, Sep 2008. doi: 10.1088/1741-2560/5/3/004. URL http://dx.doi.org/10.1088/1741-2560/5/3/004. 24, 109

[12] Maria Elisabetta Ruaro, Paolo Bonifazi, and Vincent Torre. Toward the neurocomputer: image processing and pattern recognition with neuronal cultures. *IEEE T Bio-Med Eng*, 52(3):371–383, Mar 2005. doi: 10.1109/TBME.2004.842975. URL http://dx.doi.org/10.1109/TBME.2004.842975. 24, 109

[13] Paolo Bonifazi, Maria Elisabetta Ruaro, and Vincent Torre. Statistical properties of information processing in neuronal networks. *Eur J Neurosci*, 22 (11):2953–2964, Dec 2005. doi: 10.1111/j.1460-9568.2005.04464.x. URL http://dx.doi.org/10.1111/j.1460-9568.2005.04464.x. 2, 24, 92, 109

[14] Sabnam O Rijal and Guenter W Gross. Dissociation constants for gaba(a) receptor antagonists determined with neuronal networks on microelectrode arrays. *J Neurosci Methods*, 173(2):183–192, Aug 2008. doi: 10.1016/j.jneumeth.2008.05.025. URL http://dx.doi.org/10.1016/j.jneumeth.2008.05.025. 2, 24, 92

[15] C. K. Yeung, F. Sommerhage, G. Wrobel, A. Offenhäusser, M. Chan, and S. Ingebrandt. Drug profiling using planar microelectrode arrays. *Anal Bioanal Chem*, 387(8):2673–2680, Apr 2007. doi: 10.1007/s00216-007-1172-8. URL http://dx.doi.org/10.1007/s00216-007-1172-8. 23, 24, 92

[16] Carolina García-Martinez, Marc Humet, Rosa Planells-Cases, Ana Gomis, Marco Caprini, Felix Viana, Elvira De La Pena, Francisco Sanchez-Baeza,

Teresa Carbonell, Carmen De Felipe, Enrique Pérez-Paya, Carlos Belmonte, Angel Messeguer, and Antonio Ferrer-Montiel. Attenuation of thermal nociception and hyperalgesia by vr1 blockers. *Proc Natl Acad Sci U S A*, 99(4):2374–2379, Feb 2002. doi: 10.1073/pnas.022285899. URL http://dx.doi.org/10.1073/pnas.022285899.

[17] Robert H. Kraus, Jr., Michelle A. Espy, Petr L. Volegov, Andrei N. Matlachov, John C. Mosher, Algis V. Urbaitis, and Vadim S. Zotev. Toward squid-based direct measurement of neural currents by nuclear magnetic resonance. *IEEE T Appl Supercon*, 17(2, Part 1):854–857, JUN 2007. ISSN 1051-8223. doi: 10.1109/TASC.2007.897724. Applied Superconductivity Conference 2006, Seattle, WA, AUG 27-SEP 01, 2006.

[18] Stephen P Arneric, Mark Holladay, and Michael Williams. Neuronal nicotinic receptors: a perspective on two decades of drug discovery research. *Biochem Pharmacol*, 74(8):1092–1101, Oct 2007. doi: 10.1016/j.bcp.2007.06.033. URL http://dx.doi.org/10.1016/j.bcp.2007.06.033.

[19] Daniel P Walker, Donn G Wishka, David W Piotrowski, Shaojuan Jia, Steven C Reitz, Karen M Yates, Jason K Myers, Tatiana N Vetman, Brandon J Margolis, E. Jon Jacobsen, Brad A Acker, Vincent E Groppi, Mark L Wolfe, Bruce A Thornburgh, Paula M Tinholt, Luz A Cortes-Burgos, Rodney R Walters, Matthew R Hester, Eric P Seest, Lester A Dolak, Fusen Han, Barbara A Olson, Laura Fitzgerald, Brian A Staton, Thomas J Raub, Mihaly Hajos, William E Hoffmann, Kai S Li, Nicole R Higdon, Theron M Wall, Raymond S Hurst, Erik H F Wong, and Bruce N Rogers. Design, synthesis, structure-activity relationship, and in vivo activity of azabicyclic aryl amides as alpha7 nicotinic acetylcholine receptor agonists. *Bioorg Med Chem*, 14(24):8219–8248, Dec 2006. doi: 10.1016/j.bmc.2006.09.019. URL http://dx.doi.org/10.1016/j.bmc.2006.09.019. 2

[20] C. Hamani, J. N. Nobrega, and A. M. Lozano. Deep brain stimulation in clinical practice and in animal models. *Clin Pharmacol Ther*, 88(4):559–562, Oct 2010. doi: 10.1038/clpt.2010.133. URL http://dx.doi.org/10.1038/clpt.2010.133. 2, 23

[21] Peter Konrad and Todd Shanks. Implantable brain computer interface: challenges to neurotechnology translation. *Neurobiol Dis*, 38(3):369–375, Jun 2010. doi: 10.1016/j.nbd.2009.12.007. URL http://dx.doi.org/10.1016/j.nbd.2009.12.007. 23, 24

[22] Douglas Yanai, James D Weiland, Manjunatha Mahadevappa, Robert J Greenberg, Ione Fine, and Mark S Humayun. Visual performance using a retinal prosthesis in three subjects with retinitis pigmentosa. *Am J Ophthalmol*, 143(5):820–827, May 2007. doi: 10.1016/j.ajo.2007.01.027. URL http://dx.doi.org/10.1016/j.ajo.2007.01.027. 23

[23] Chris Sekirnjak, Pawel Hottowy, Alexander Sher, Wladyslaw Dabrowski, Alan M Litke, and E. J. Chichilnisky. High-resolution electrical stimulation of primate retina for epiretinal implant design. *J Neurosci*, 28 (17):4446–4456, Apr 2008. doi: 10.1523/JNEUROSCI.5138-07.2008. URL http://dx.doi.org/10.1523/JNEUROSCI.5138-07.2008. 23

[24] P. Limousin, P. Pollak, A. Benazzouz, D. Hoffmann, J. F. Le Bas, E. Broussolle, J. E. Perret, and A. L. Benabid. Effect of parkinsonian signs and symptoms of bilateral subthalamic nucleus stimulation. *Lancet*, 345(8942):91–95, Jan 1995. 23

[25] R. A. Normann, E. M. Maynard, P. J. Rousche, and D. J. Warren. A neural interface for a cortical vision prosthesis. *Vision Res*, 39(15):2577–2587, Jul 1999. 23

[26] E. Fernández, F. Pelayo, S. Romero, M. Bongard, C. Marin, A. Alfaro, and L. Merabet. Development of a cortical visual neuroprosthesis for the blind: the relevance of neuroplasticity. *J Neural Eng*, 2(4):R1–12, Dec 2005. doi: 10.1088/1741-2560/2/4/R01. URL http://dx.doi.org/10.1088/1741-2560/2/4/R01. 2, 23

[27] JJ Pancrazio, PP Bey, DS Cuttino, JK Kusel, DA Borkholder, KM Shaffer, GTA Kovacs, and DA Stenger. Portable cell-based biosensor system for toxin detection. *SENSORS AND ACTUATORS B-CHEMICAL*, 53(3):179–185, DEC 10 1998. ISSN 0925-4005. 2, 23, 24, 92

[28] A. Gramowski, D. Schiffmann, and G. W. Gross. Quantification of acute neurotoxic effects of trimethyltin using neuronal networks cultured on microelectrode arrays. *Neurotoxicology*, 21(3):331–342, Jun 2000. 2, 23, 24, 92

[29] J. O'Kusky and M. Colonnier. A laminar analysis of the number of neurons, glia, and synapses in the adult cortex (area 17) of adult macaque monkeys. *J Comp Neurol*, 210(3):278–290, Sep 1982. doi: 10.1002/cne.902100307. URL http://dx.doi.org/10.1002/cne.902100307. 2

[30] G. Leuba and L. J. Garey. Comparison of neuronal and glial numerical density in primary and secondary visual cortex of man. *Exp Brain Res*, 77(1):31–38, 1989. 2

[31] B. Sakmann and E. Neher. *Single-channel recording*. Plenum Press, 1983. ISBN 9780306414190. URL http://books.google.com/books?id=VGnwAAAAMAAJ. 2

[32] M. Estacion, J. S. Choi, E. M. Eastman, Z. Lin, Y. Li, L. Tyrrell, Y. Yang, S. D. Dib-Hajj, and S. G. Waxman. Can robots patch-clamp as well as humans? characterization of a novel sodium channel mutation. *J Physiol*, 588(Pt 11):1915–1927, Jun 2010. doi: 10.1113/jphysiol.2009.186114. URL http://dx.doi.org/10.1113/jphysiol.2009.186114. 3

[33] D. Vasilyev, T. Merrill, A. Iwanow, J. Dunlop, and M. Bowlby. A novel method for patch-clamp automation. *Pflugers Arch*, 452(2):240–247, May 2006. doi: 10.1007/s00424-005-0029-2. URL http://dx.doi.org/10.1007/s00424-005-0029-2.

[34] Dmitry V Vasilyev, Thomas L Merrill, and Mark R Bowlby. Development of a novel automated ion channel recording method using "inside-out" whole-cell membranes. *J Biomol Screen*, 10(8):806–813, Dec 2005. doi: 10.1177/1087057105279481. URL http://dx.doi.org/10.1177/1087057105279481.

[35] Margit Asmild, Nicholas Oswald, Karen M Krzywkowski, Søren Friis, Rasmus B Jacobsen, Dirk Reuter, Rafael Taboryski, Jonathan Kutchinsky, Ras K Vestergaard, Rikke L Schrøder, Claus B Sørensen, Morten Bech, Mads P G Korsgaard, and Niels J Willumsen. Upscaling and automation of electrophysiology: toward high throughput screening in ion channel drug discovery. *Receptors Channels*, 9 (1):49–58, 2003. 3

[36] Niels Fertig, Robert H Blick, and Jan C Behrends. Whole cell patch clamp recording performed on a planar glass chip. *Biophys J*, 82 (6):3056–3062, Jun 2002. doi: 10.1016/S0006-3495(02)75646-4. URL http://dx.doi.org/10.1016/S0006-3495(02)75646-4. 3, 8

[37] Wee-Liat Ong, Kum-Cheong Tang, Ajay Agarwal, Ranganathan Nagarajan, Lian-Wee Luo, and Levent Yobas. Microfluidic integration of substantially round glass capillaries for lateral patch clamping on chip. *Lab Chip*, 7(10):1357–1366, Oct 2007. doi: 10.1039/b707439e. URL http://dx.doi.org/10.1039/b707439e. 3

[38] Kathryn G Klemic, James F Klemic, and Fred J Sigworth. An air-molding technique for fabricating pdms planar patch-clamp electrodes. *Pflugers Arch*, 449(6):564–572, Mar 2005. doi: 10.1007/s00424-004-1360-8. URL http://dx.doi.org/10.1007/s00424-004-1360-8. 3

[39] Jian Chen and Jie Tian. Rapid multi-modality preregistration based on sift descriptor. In *Proc. 28th Annual Int. Conf. of the IEEE Engineering in Medicine and Biology Society EMBS '06*, pages 1437–1440, 2006. doi: 10.1109/IEMBS.2006.260599. 3

[40] Thomas Sordel, Stéphanie Garnier-Raveaud, Fabien Sauter, Catherine Pudda, Frédérique Marcel, Michel De Waard, Christophe Arnoult, Michel Vivaudou, François Chatelain, and Nathalie Picollet-D'hahan. Hourglass sio2 coating increases the performance of planar patch-clamp. *J Biotechnol*, 125(1):142–154, Aug 2006. doi: 10.1016/j.jbiotec.2006.02.008. URL http://dx.doi.org/10.1016/j.jbiotec.2006.02.008. 3

[41] Jonatan Kutchinsky, Søren Friis, Margit Asmild, Rafael Taboryski, Simon Pedersen, Ras K Vestergaard, Rasmus B Jacobsen, Karen Krzywkowski, Rikke L Schrøder, Trine Ljungstrøm, Nathalie Hélix, Claus B Sørensen, Morten Bech, and Niels J Willumsen. Characterization of potassium channel modulators with qpatch automated patch-clamp technology: system characteristics and performance. *Assay Drug Dev Technol*, 1(5):685–693, Oct 2003. doi: 10.1089/154065803770381048. URL http://dx.doi.org/10.1089/154065803770381048. 3

[42] Kirk Schroeder, Brad Neagle, Derek J Trezise, and Jennings Worley. Ionworks ht: a new high-throughput electrophysiology measurement platform. *J Biomol Screen*, 8(1):50–64, Feb 2003. doi: 10.1177/1087057102239667. URL http://dx.doi.org/10.1177/1087057102239667. 3, 8

[43] C. A. Thomas, P. A. Springer, G. E. Loeb, Y. Berwald-Netter, and L. M. Okun. A miniature microelectrode array to monitor the bioelectric activity of cultured cells. *Exp Cell Res*, 74(1):61–66, Sep 1972. 3, 91

[44] G. W. Gross. Simultaneous single unit recording in vitro with a photoetched laser deinsulated gold multimicroelectrode surface. *IEEE T Bio-Med Eng*, 26(5):273–279, May 1979. 20

[45] J PINE. Recording action-potentials from cultured neurons with extracellular micro-circuit electrodes. *J Neurosci Methods*, 2(1):19–31, 1980. ISSN 0165-0270. 3, 91

[46] Michael Serra, Amy Chan, Maya Dubey, Vladimir Gilman, and Thomas Shea. A low-cost interface for multi-electrode array data acquisition systems. *BioTechniques*, 45(4):451–456, Oct 2008. doi: 10.2144/000112911. URL http://dx.doi.org/10.2144/000112911. 3, 25, 43

[47] Jonathan Erickson, Angela Tooker, Y-C. Tai, and Jerome Pine. Caged neuron mea: a system for long-term investigation of cultured neural network connectivity. *J Neurosci Methods*, 175(1):1–16, Oct 2008. doi: 10.1016/j.jneumeth.2008.07.023. URL http://dx.doi.org/10.1016/j.jneumeth.2008.07.023. 3, 4, 25, 43, 109, 110

[48] Karen A Moxon, Steve C Leiser, Greg A Gerhardt, Kenneth A Barbee, and John K Chapin. Ceramic-based multisite electrode arrays for chronic single-neuron recording. *IEEE T Bio-Med Eng*, 51(4):647–656, Apr 2004. doi: 10.1109/TBME.2003.821037. URL http://dx.doi.org/10.1109/TBME.2003.821037. 3, 24, 92

[49] G. W. Gross, W. Y. Wen, and J. W. Lin. Transparent indium-tin oxide electrode patterns for extracellular, multisite recording in neuronal cultures. *J Neurosci Methods*, 15(3):243–252, 1985. 24

[50] Ju-Hyun Kim, Gyumin Kang, Yoonkey Nam, and Yang-Kyu Choi. Surface-modified microelectrode array with flake nanostructure for neural recording and stimulation. *Nanotechnology*, 21(8):85303, Feb 2010. doi: 10.1088/0957-4484/21/8/085303. URL http://dx.doi.org/10.1088/0957-4484/21/8/085303. 24

[51] Erkin Seker, Yevgeny Berdichevsky, Matthew R Begley, Michael L Reed, Kevin J Staley, and Martin L Yarmush. The fabrication of low-impedance nanoporous gold multiple-electrode arrays for neural electrophysiology studies. *Nanotechnology*, 21(12):125504, Mar 2010. doi: 10.1088/0957-4484/21/12/125504. URL http://dx.doi.org/10.1088/0957-4484/21/12/125504. 24

[52] Mohammad Reza Abidian and David C Martin. Experimental and theoretical characterization of implantable neural microelectrodes modified with conducting polymer nanotubes. *Biomaterials*, 29(9):1273–1283, Mar 2008. doi: 10.1016/j.biomaterials.2007.11.022. URL http://dx.doi.org/10.1016/j.biomaterials.2007.11.022. 24

[53] M. Hughes, M.S.P. Shaffer, A.C. Renouf, C. Singh, G.Z. Chen, D.J. Fray, and A.H. Windle. Electrochemical capacitance of nanocomposite films formed by coating aligned arrays of carbon nanotubes with polypyrrole. *Adv Mater*, 14(5):382–385, 2002. ISSN 1521-4095. URL http://dx.doi.org/10.1002/1521-4095(20020304)14:5<382::AID-ADMA382>3.0.CO;2-Y. 24

[54] Tamir Gabay, Moti Ben-David, Itshak Kalifa, Raya Sorkin, Ze'ev R Abrams, Eshel Ben-Jacob, and Yael Hanein. Electro-chemical and biological properties of carbon nanotube based multi-electrode arrays. *Nanotechnology*, 18(3):035201, Jan 2007. doi: 10.1088/0957-4484/18/3/035201. URL http://dx.doi.org/10.1088/0957-4484/18/3/035201. 24, 25, 43, 52, 92

[55] Fernando Patolsky, Brian P Timko, Guihua Yu, Ying Fang, Andrew B Greytak, Gengfeng Zheng, and Charles M Lieber. Detection, stimulation, and inhibition of neuronal signals with high-density nanowire transistor arrays. *Science*, 313(5790):1100–1104, Aug 2006. doi: 10.1126/science.1128640. URL http://dx.doi.org/10.1126/science.1128640. 24, 25, 43, 52, 92

[56] Tzahi Cohen-Karni, Brian P Timko, Lucien E Weiss, and Charles M Lieber. Flexible electrical recording from cells using nanowire transistor arrays. *Proc Natl Acad Sci U S A*, 106(18):7309–7313, May 2009. doi: 10.1073/pnas.0902752106. URL http://dx.doi.org/10.1073/pnas.0902752106. 3, 24, 25, 43, 52, 92

[57] Marc Olivier Heuschkel, Michael Fejtl, Mario Raggenbass, Daniel Bertrand, and Philippe Renaud. A three-dimensional multi-electrode array for multi-site stimulation and recording in acute brain slices. *J Neurosci Methods*, 114(2):135–148, Mar 2002. 3, 24, 92

[58] Aviad Hai, Joseph Shappir, and Micha E Spira. In-cell recordings by extracellular microelectrodes. *Nat Methods*, 7(3):200–202, Mar 2010. doi: 10.1038/nmeth.1420. URL http://dx.doi.org/10.1038/nmeth.1420. 3, 24, 92

[59] Shimon Marom and Goded Shahaf. Development, learning and memory in large random networks of cortical neurons: lessons beyond anatomy. *Q Rev Biophys*, 35(1):63–87, Feb 2002. 4, 109

[60] Enric Claverol-Tinture and Jerome Pine. Extracellular potentials in low-density dissociated neuronal cultures. *J Neurosci Methods*, 117(1):13–21, May 2002. 4, 52, 109

[61] Carl Gold, Darrell A Henze, Christof Koch, and György Buzsáki. On the origin of the extracellular action potential waveform: A modeling study. *J Neurophysiol*, 95(5):3113–3128, May 2006. doi: 10.1152/jn.00979.2005. URL http://dx.doi.org/10.1152/jn.00979.2005. 4, 52, 109

[62] Ronen Segev, Morris Benveniste, Yoash Shapira, and Eshel Ben-Jacob. Formation of electrically active clusterized neural networks. *Phys Rev Lett*, 90(16):168101, Apr 2003. 4, 110

[63] Luca Berdondini, Kilian Imfeld, Alessandro Maccione, Mariateresa Tedesco, Simon Neukom, Milena Koudelka-Hep, and Sergio Martinoia. Active pixel sensor array for high spatio-temporal resolution electrophysiological recordings from single cell to large scale neuronal networks. *Lab Chip*, 9(18):2644–2651, Sep 2009. doi: 10.1039/b907394a. URL http://dx.doi.org/10.1039/b907394a. 4, 110

[64] M. Hutzler, A. Lambacher, B. Eversmann, M. Jenkner, R. Thewes, and P. Fromherz. High-resolution multitransistor array recording of electrical field potentials in cultured brain slices. *J Neurophysiol*, 96(3):1638–1645, Sep 2006. doi: 10.1152/jn.00347.2006. URL http://dx.doi.org/10.1152/jn.00347.2006. 4, 110

[65] M. P. Maher, J. Pine, J. Wright, and Y. C. Tai. The neurochip: a new multi-electrode device for stimulating and recording from cultured neurons. *J Neurosci Methods*, 87(1):45–56, Feb 1999. 4, 110

[66] G. Zeck and P. Fromherz. Noninvasive neuroelectronic interfacing with synaptically connected snail neurons immobilized on a semiconductor chip. *Proc Natl Acad Sci U S A*, 98(18):10457–10462, Aug 2001. doi: 10.1073/pnas.181348698. URL http://dx.doi.org/10.1073/pnas.181348698. 110

[67] M. Merz and P. Fromherz. Silicon chip interfaced with a geometrically defined net of snail neurons. *Adv Funct Mater*, 15(5):739–744, 2005. ISSN 1616-3028. doi: 10.1002/adfm.200400316. URL http://dx.doi.org/10.1002/adfm.200400316. 110

[68] I. Suzuki, Y. Sugio, H. Moriguchi, A. Hattori, K. Yasuda, and Y. Jimbo. Pattern modification of a neuronal network for individual-cell-based electrophysiological measurement using photothermal etching of an agarose architecture with a multielectrode array. *IEE Proc Nanobiotechnol*, 151(3):116–21, June 2004. 110

[69] Ikurou Suzuki, Yoshihiro Sugio, Yasuhiko Jimbo, and Kenji Yasuda. Stepwise pattern modification of neuronal network in photo-thermally-etched agarose architecture on multi-electrode array chip for individual-cell-based electrophysiological measurement. *Lab Chip*, 5(3):241–247, Mar 2005. doi: 10.1039/b406885h. URL http://dx.doi.org/10.1039/b406885h. 8, 110

[70] J. M. Corey, B. C. Wheeler, and G. J. Brewer. Compliance of hippocampal neurons to patterned substrate networks. *J Neurosci Res*, 30(2):300–307, Oct 1991. doi: 10.1002/jnr.490300204. URL http://dx.doi.org/10.1002/jnr.490300204. 110

[71] Helga Sorribas, Celestino Padeste, and Louis Tiefenauer. Photolithographic generation of protein micropatterns for neuron culture applications. *Biomaterials*, 23 (3):893–900, Feb 2002. 110

[72] John C Chang, Gregory J Brewer, and Bruce C Wheeler. A modified microstamping technique enhances polylysine transfer and neuronal cell patterning. *Biomaterials*, 24(17):2863–2870, Aug 2003. 110

[73] Yoonkey Nam, Katherine Musick, and Bruce C Wheeler. Application of a pdms microstencil as a replaceable insulator toward a single-use planar microelectrode array. *Biomed Microdevices*, 8(4):375–381, Dec 2006. doi: 10.1007/s10544-006-9145-9. URL http://dx.doi.org/10.1007/s10544-006-9145-9. 110, 111

[74] Gyumin Kang, Ji-Hye Lee, Chang-Soo Lee, and Yoonkey Nam. Agarose microwell based neuronal micro-circuit arrays on microelectrode arrays for high throughput drug testing. *Lab Chip*, 9(22):3236–3242, Nov 2009. doi: 10.1039/b910738j. URL http://dx.doi.org/10.1039/b910738j. 4, 110

[75] Alan Jasanoff. Bloodless fmri. *Trends Neurosci*, 30(11): 603–610, Nov 2007. doi: 10.1016/j.tins.2007.08.002. URL http://dx.doi.org/10.1016/j.tins.2007.08.002. 4

[76] Helene Benveniste and Stephen J Blackband. Translational neuroscience and magnetic-resonance microscopy. *Lancet Neurol*, 5(6): 536–544, Jun 2006. doi: 10.1016/S1474-4422(06)70472-0. URL http://dx.doi.org/10.1016/S1474-4422(06)70472-0. 4

[77] Alan Jasanoff and Phillip Z Sun. In vivo magnetic resonance microscopy of brain structure in unanesthetized flies. *J Magn Reson*, 158(1-2):79–85, 2002. 4

[78] Thomas Knöpfel, Javier Díez-García, and Walther Akemann. Optical probing of neuronal circuit dynamics: genetically encoded versus classical fluorescent sensors. *Trends Neurosci*, 29(3):160–166, Mar 2006. doi: 10.1016/j.tins.2006.01.004. URL http://dx.doi.org/10.1016/j.tins.2006.01.004. 4

[79] Alison L Barth. Visualizing circuits and systems using transgenic reporters of neural activity. *Curr Opin Neurobiol*, 17(5):567–571, Oct 2007. doi: 10.1016/j.conb.2007.10.003. URL http://dx.doi.org/10.1016/j.conb.2007.10.003.

[80] De-Lai Qiu, Walther Akemann, Chun-Ping Chu, Rikita Araki, and Thomas Knöpfel. Targeted optical probing of neuronal circuit dynamics using fluorescent protein sensors. *Neurosignals*, 16(4):289–299, 2008. doi: 10.1159/000123039. URL http://dx.doi.org/10.1159/000123039.

[81] B. J. Baker, H. Mutoh, D. Dimitrov, W. Akemann, A. Perron, Y. Iwamoto, L. Jin, L. B. Cohen, E. Y. Isacoff, V. A. Pieribone, T. Hughes, and T. Knöpfel. Genetically encoded fluorescent sensors of membrane potential. *Brain Cell Biol*, 36(1-4):53–67, Aug 2008. doi: 10.1007/s11068-008-9026-7. URL http://dx.doi.org/10.1007/s11068-008-9026-7.

[82] Walther Akemann, Alicia Lundby, Hiroki Mutoh, and Thomas Knöpfel. Effect of voltage sensitive fluorescent proteins on neuronal excitability. *Biophys J*, 96(10):3959–3976, May 2009. doi: 10.1016/j.bpj.2009.02.046. URL http://dx.doi.org/10.1016/j.bpj.2009.02.046. 4

[83] Sunita Ghimire Gautam, Amelie Perron, Hiroki Mutoh, and Thomas Knöpfel. Exploration of fluorescent protein voltage probes based on circularly permuted fluorescent proteins. *Front Neuroeng*, 2:14, 2009. doi: 10.3389/neuro.16.014.2009. URL http://dx.doi.org/10.3389/neuro.16.014.2009. 4

[84] Dejan Zecevic, Maja Djurisic, Lawrence B Cohen, Srdjan Antic, Matt Wachowiak, Chun X Falk, and Michal R Zochowski. Imaging nervous system activity with voltage-sensitive dyes. *Curr Protoc Neurosci*, Chapter 6:Unit 6.17, Aug 2003. doi: 10.1002/0471142301.ns0617s23. URL http://dx.doi.org/10.1002/0471142301.ns0617s23. 4

[85] Ryota Homma, Bradley J Baker, Lei Jin, Olga Garaschuk, Arthur Konnerth, Lawrence B Cohen, Chun X Bleau, Marco Canepari, Maja Djurisic, and Dejan Zecevic. Wide-field and two-photon imaging of

brain activity with voltage- and calcium-sensitive dyes. *Methods Mol Biol*, 489:43–79, 2009. doi: 10.1007/978-1-59745-543-5_3. URL http://dx.doi.org/10.1007/978-1-59745-543-5_3. 4

[86] Bin Shen, Zheng Xiang, Barbara Miller, Gordon Louie, Wenyuan Wang, Joseph P Noel, Fred H Gage, and Lei Wang. Genetically encoding unnatural amino acids in neural stem cells and optically reporting voltage-sensitive domain changes in differentiated neurons. *Stem Cells*, 29(8):1231–1240, Aug 2011. doi: 10.1002/stem.679. URL http://dx.doi.org/10.1002/stem.679. 4

[87] Joel M Kralj, Daniel R Hochbaum, Adam D Douglass, and Adam E Cohen. Electrical spiking in escherichia coli probed with a fluorescent voltage-indicating protein. *Science*, 333(6040):345–348, Jul 2011. doi: 10.1126/science.1204763. URL http://dx.doi.org/10.1126/science.1204763. 4

[88] Wenjun Jin, Ren-Ji Zhang, and Jian young Wu. Voltage-sensitive dye imaging of population neuronal activity in cortical tissue. *J Neurosci Methods*, 115(1):13–27, Mar 2002. 5

[89] P. Y. Chang and M. B. Jackson. Interpretation and optimization of absorbance and fluorescence signals from voltage-sensitive dyes. *J Membr Biol*, 196(2):105–116, Nov 2003. doi: 10.1007/s00232-003-0629-8. URL http://dx.doi.org/10.1007/s00232-003-0629-8.

[90] T. Surrey, M. B. Elowitz, P. E. Wolf, F. Yang, F. Nédélec, K. Shokat, and S. Leibler. Chromophore-assisted light inactivation and self-organization of microtubules and motors. *Proc Natl Acad Sci U S A*, 95(8):4293–4298, Apr 1998. 5

[91] D. K. HILL. The effect of stimulation on the opacity of a crustacean nerve trunk and its relation to fibre diameter. *J Physiol*, 111(3-4):283–303, Oct 1950. 5

[92] Kathleen M Carter, John S George, and David M Rector. Simultaneous birefringence and scattered light measurements reveal anatomical features in isolated crustacean nerve. *J Neurosci Methods*, 135 (1-2):9–16, May 2004. doi: 10.1016/j.jneumeth.2003.11.010. URL http://dx.doi.org/10.1016/j.jneumeth.2003.11.010. 5

[93] Leonardo Sacconi, Jonathan Mapelli, Daniela Gandolfi, Jacopo Lotti, Rodney P O'Connor, Egidio D'Angelo, and Francesco S Pavone. Optical recording of elec-

trical activity in intact neuronal networks with random access second-harmonic generation microscopy. *Opt Express*, 16(19):14910–14921, Sep 2008. 5

[94] Jiang Jiang and Rafael Yuste. Second-harmonic generation imaging of membrane potential with photon counting. *Microsc Microanal*, 14(6):526–531, Dec 2008. doi: 10.1017/S1431927608080811. URL http://dx.doi.org/10.1017/S1431927608080811. 5

[95] K. V. Gopal, B. R. Miller, and G. W. Gross. Acute and sub-chronic functional neurotoxicity of methylphenidate on neural networks in vitro. *J Neural Transm*, 114(11):1365–1375, 2007. doi: 10.1007/s00702-007-0759-8. URL http://dx.doi.org/10.1007/s00702-007-0759-8. 8

[96] Jelena Ban, Paolo Bonifazi, Giulietta Pinato, Frederic D Broccard, Lorenz Studer, Vincent Torre, and Maria Elisabetta Ruaro. Embryonic stem cell-derived neurons form functional networks in vitro. *Stem Cells*, 25(3):738–749, Mar 2007. doi: 10.1634/stemcells.2006-0246. URL http://dx.doi.org/10.1634/stemcells.2006-0246. 8

[97] Sanjay K Mistry, Edward W Keefer, Bruce A Cunningham, Gerald M Edelman, and Kathryn L Crossin. Cultured rat hippocampal neural progenitors generate spontaneously active neural networks. *Proc Natl Acad Sci U S A*, 99(3):1621–1626, Feb 2002. doi: 10.1073/pnas.022646599. URL http://dx.doi.org/10.1073/pnas.022646599. 8

[98] Walid V Soussou, Geoffrey J Yoon, Roberta Diaz Brinton, and Theodore W Berger. Neuronal network morphology and electrophysiologyof hippocampal neurons cultured on surface-treated multielectrode arrays. *IEEE T Bio-Med Eng*, 54(7):1309–1320, Jul 2007. doi: 10.1109/TBME.2006.889195. URL http://dx.doi.org/10.1109/TBME.2006.889195. 8, 17, 20

[99] Danny Eytan and Shimon Marom. Dynamics and effective topology underlying synchronization in networks of cortical neurons. *J Neurosci*, 26 (33):8465–8476, Aug 2006. doi: 10.1523/JNEUROSCI.1627-06.2006. URL http://dx.doi.org/10.1523/JNEUROSCI.1627-06.2006. 8

[100] Alfred Stett, Ulrich Egert, Elke Guenther, Frank Hofmann, Thomas Meyer, Wilfried Nisch, and Hugo Haemmerle. Biological application of microelectrode arrays in drug discovery and basic research. *Anal Bioanal*

Chem, 377(3):486–495, Oct 2003. doi: 10.1007/s00216-003-2149-x. URL http://dx.doi.org/10.1007/s00216-003-2149-x. 8

[101] Peter B Simpson and Keith A Wafford. New directions in kinetic high information content assays. *Drug Discov Today*, 11(5-6):237–244, Mar 2006. 8

[102] S. Hafizovic, F. Heer, T. Ugniwenko, U. Frey, A. Blau, C. Ziegler, and A. Hierlemann. A cmos-based microelectrode array for interaction with neuronal cultures. *J Neurosci Methods*, 164(1):93–106, Aug 2007. doi: 10.1016/j.jneumeth.2007.04.006. URL http://dx.doi.org/10.1016/j.jneumeth.2007.04.006. 8

[103] Laura Rowe, Mahmoud Almasri, Kil Lee, Nick Fogleman, Gregory J Brewer, Yoonkey Nam, Bruce C Wheeler, Jelena Vukasinovic, Ari Glezer, and A. Bruno Frazier. Active 3-d microscaffold system with fluid perfusion for culturing in vitro neuronal networks. *Lab Chip*, 7(4):475–482, Apr 2007. doi: 10.1039/b700795g. URL http://dx.doi.org/10.1039/b700795g. 8

[104] Joseph J Pancrazio, Samuel A Gray, Yura S Shubin, Nadezhda Kulagina, David S Cuttino, Kara M Shaffer, Kevin Eisemann, Anthony Curran, Bret Zim, Guenter W Gross, and Thomas J O'Shaughnessy. A portable microelectrode array recording system incorporating cultured neuronal networks for neurotoxin detection. *Biosens Bioelectron*, 18(11):1339–1347, Oct 2003. 8

[105] G. Banker and K. Goslin. *Culturing nerve cells*. Cellular and molecular neuroscience series. MIT Press, 2 edition, 1998. ISBN 9780262024389. URL http://books.google.com/books?id=yVAYQBt1gEIC. 8, 14

[106] Ricardo Morales, Michael Riss, Ling Wang, Rosalina Gavín, Jose Antonio Del Río, Ramon Alcubilla, and Enric Claverol-Tinturé. Integrating multi-unit electrophysiology and plastic culture dishes for network neuroscience. *Lab Chip*, 8(11):1896–1905, Nov 2008. doi: 10.1039/b802165a. URL http://dx.doi.org/10.1039/b802165a. 9, 12, 24, 25, 26, 28, 116

[107] C. Koch and I. Segev. *Methods in neuronal modeling: from ions to networks*. Computational neuroscience. MIT Press, 1998. ISBN 9780262112314. URL http://books.google.com/books?id=5GMV2onekvsC. 10

[108] Erwin van Vliet, Luc Stoppini, Maurizio Balestrino, Chantra Eskes, Claudius Griesinger, Tomasz Sobanski, Maurice Whelan, Thomas Hartung, and Sandra Coecke. Electrophysiological recording of re-aggregating brain cell cul-

tures on multi-electrode arrays to detect acute neurotoxic effects. *Neurotoxicology*, 28(6):1136–1146, Nov 2007. doi: 10.1016/j.neuro.2007.06.004. URL http://dx.doi.org/10.1016/j.neuro.2007.06.004. 10, 20

[109] Frauke Otto, Philipp Görtz, Wiebke Fleischer, and Mario Siebler. Cryopreserved rat cortical cells develop functional neuronal networks on microelectrode arrays. *J Neurosci Methods*, 128(1-2):173–181, Sep 2003. 14, 15

[110] Katherine L Perkins. Cell-attached voltage-clamp and current-clamp recording and stimulation techniques in brain slices. *J Neurosci Methods*, 154(1-2):1–18, Jun 2006. doi: 10.1016/j.jneumeth.2006.02.010. URL http://dx.doi.org/10.1016/j.jneumeth.2006.02.010. 20

[111] Kostas N Fountas, Eftychia Kapsalaki, and Georgios Hadjigeorgiou. Cerebellar stimulation in the management of medically intractable epilepsy: a systematic and critical review. *Neurosurg Focus*, 29(2):E8, Aug 2010. doi: 10.3171/2010.5.FOCUS10111. URL http://dx.doi.org/10.3171/2010.5.FOCUS10111. 23

[112] I. S. Cooper, I. Amin, M. Riklan, J. M. Waltz, and T. P. Poon. Chronic cerebellar stimulation in epilepsy. clinical and anatomical studies. *Arch Neurol*, 33(8):559–570, Aug 1976. 23

[113] Nicholas G Hatsopoulos and John P Donoghue. The science of neural interface systems. *Annu Rev Neurosci*, 32:249–266, 2009. doi: 10.1146/annurev.neuro.051508.135241. URL http://dx.doi.org/10.1146/annurev.neuro.051508.135241. 23

[114] Sridhar Sunderam, Bruce Gluckman, Davide Reato, and Marom Bikson. Toward rational design of electrical stimulation strategies for epilepsy control. *Epilepsy Behav*, 17(1):6–22, Jan 2010. doi: 10.1016/j.yebeh.2009.10.017. URL http://dx.doi.org/10.1016/j.yebeh.2009.10.017. 23

[115] Meel Velliste, Sagi Perel, M. Chance Spalding, Andrew S Whitford, and Andrew B Schwartz. Cortical control of a prosthetic arm for self-feeding. *Nature*, 453(7198):1098–1101, Jun 2008. doi: 10.1038/nature06996. URL http://dx.doi.org/10.1038/nature06996. 24

[116] Leigh R Hochberg, Mijail D Serruya, Gerhard M Friehs, Jon A Mukand, Maryam Saleh, Abraham H Caplan, Almut Branner, David Chen, Richard D Penn, and John P Donoghue. Neuronal ensemble control of prosthetic devices by a human

with tetraplegia. *Nature*, 442(7099):164–171, Jul 2006. doi: 10.1038/nature04970. URL http://dx.doi.org/10.1038/nature04970. 24

[117] Kevin Warwick, Mark Gasson, Benjamin Hutt, Iain Goodhew, Peter Kyberd, Brian Andrews, Peter Teddy, and Amjad Shad. The application of implant technology for cybernetic systems. *Arch Neurol*, 60 (10):1369–1373, Oct 2003. doi: 10.1001/archneur.60.10.1369. URL http://dx.doi.org/10.1001/archneur.60.10.1369. 24

[118] Stuart R. Cogan. Neural stimulation and recording electrodes. *Annu Rev Biomed Eng*, 10:275–309, 2008. ISSN 1523-9829. doi: 10.1146/annurev.bioeng.10.061807.160518. 24

[119] Viviana Lovat, Davide Pantarotto, Laura Lagostena, Barbara Cacciari, Micaela Grandolfo, Massimo Righi, Giampiero Spalluto, Maurizio Prato, and Laura Ballerini. Carbon nanotube substrates boost neuronal electrical signaling. *Nano Lett*, 5(6):1107–1110, Jun 2005. doi: 10.1021/nl050637m. URL http://dx.doi.org/10.1021/nl050637m. 24

[120] AM Taylor, M Blurton-Jones, SW Rhee, DH Cribbs, CW Cotman, and NL Jeon. A microfluidic culture platform for cns axonal injury, regeneration and transport. *Nat Methods*, 2(8):599–605, AUG 2005. ISSN 1548-7091. doi: 10.1038/NMETH777. 25, 33

[121] DL DONOHO. De-noising by soft-thresholding. *IEEE T Inform Theory*, 41(3): 613–627, MAY 1995. ISSN 0018-9448. 28

[122] N.R. Draper and H. Smith. *Applied regression analysis*. Number v. 1 in Wiley series in probability and statistics: Texts and references section. Wiley, 1998. ISBN 9780471170822. URL http://books.google.com/books?id=CJi2QgAACAAJ. 29

[123] A. L. HODGKIN and A. F. HUXLEY. A quantitative description of membrane current and its application to conduction and excitation in nerve. *J Physiol*, 117 (4):500–544, Aug 1952. 31

[124] Michael Mascagni. The backward euler method for numerical solution of the hodgkin-huxley equations of nerve conduction. *SIAM J Numer Anal*, 27(4):941–962, 1990. 32

[125] W. P. Bartlett and G. A. Banker. An electron microscopic study of the development of axons and dendrites by hippocampal neurons in culture. ii. synaptic relationships. *J Neurosci*, 4(8):1954–1965, Aug 1984. 37

[126] G. M. Shepherd and K. M. Harris. Three-dimensional structure and composition of ca3–>ca1 axons in rat hippocampal slices: implications for presynaptic connectivity and compartmentalization. *J Neurosci*, 18(20):8300–8310, Oct 1998.

[127] Shozo Jinno, Thomas Klausberger, Laszlo F Marton, Yannis Dalezios, J. David B Roberts, Pablo Fuentealba, Eric A Bushong, Darrell Henze, György Buzsáki, and Peter Somogyi. Neuronal diversity in gabaergic long-range projections from the hippocampus. *J Neurosci*, 27(33): 8790–8804, Aug 2007. doi: 10.1523/JNEUROSCI.1847-07.2007. URL http://dx.doi.org/10.1523/JNEUROSCI.1847-07.2007. 37

[128] B. FRANKENHAEUSER and B. WALTMAN. Membrane resistance and conduction velocity of large myelinated nerve fibres from xenopus laevis. *J Physiol*, 148: 677–682, Oct 1959. 45

[129] Julian P Meeks and Steven Mennerick. Action potential initiation and propagation in ca3 pyramidal axons. *J Neurophysiol*, 97(5):3460–3472, May 2007. doi: 10.1152/jn.01288.2006. URL http://dx.doi.org/10.1152/jn.01288.2006. 45, 75

[130] Jinhyun Kim and Dax A Hoffman. Potassium channels: newly found players in synaptic plasticity. *Neuroscientist*, 14(3):276–286, Jun 2008. doi: 10.1177/1073858408315041. URL http://dx.doi.org/10.1177/1073858408315041. 49

[131] Kenneth J Smith. Sodium channels and multiple sclerosis: roles in symptom production, damage and therapy. *Brain Pathol*, 17(2): 230–242, Apr 2007. doi: 10.1111/j.1750-3639.2007.00066.x. URL http://dx.doi.org/10.1111/j.1750-3639.2007.00066.x. 50, 85

[132] Karl Ng, James Howells, John D Pollard, and David Burke. Up-regulation of slow k(+) channels in peripheral motor axons: a transcriptional channelopathy in multiple sclerosis. *Brain*, 131(Pt 11):3062–3071, Nov 2008. doi: 10.1093/brain/awn180. URL http://dx.doi.org/10.1093/brain/awn180. 50

[133] Sven G Meuth, Tatjana Kanyshkov, Nico Melzer, Stefan Bittner, Bernd C Kieseier, Thomas Budde, and Heinz Wiendl. Altered neuronal expression of task1 and task3 potassium channels in rodent and human autoimmune cns inflammation.

Neurosci Lett, 446(2-3):133–138, Dec 2008. doi: 10.1016/j.neulet.2008.09.038. URL http://dx.doi.org/10.1016/j.neulet.2008.09.038. 50

[134] B. Kornek, M. K. Storch, J. Bauer, A. Djamshidian, R. Weissert, E. Wallstroem, A. Stefferl, F. Zimprich, T. Olsson, C. Linington, M. Schmidbauer, and H. Lassmann. Distribution of a calcium channel subunit in dystrophic axons in multiple sclerosis and experimental autoimmune encephalomyelitis. *Brain*, 124(Pt 6):1114–1124, Jun 2001. 50, 85

[135] Susan I V Judge, Jennifer M Lee, Christopher T Bever, and Paul M Hoffman. Voltage-gated potassium channels in multiple sclerosis: Overview and new implications for treatment of central nervous system inflammation and degeneration. *J Rehabil Res Dev*, 43(1):111–122, 2006. 50

[136] Zoltan Nusser. Variability in the subcellular distribution of ion channels increases neuronal diversity. *Trends Neurosci*, 32(5):267–274, May 2009. doi: 10.1016/j.tins.2009.01.003. URL http://dx.doi.org/10.1016/j.tins.2009.01.003. 50

[137] K. J. Rhodes, B. W. Strassle, M. M. Monaghan, Z. Bekele-Arcuri, M. F. Matos, and J. S. Trimmer. Association and colocalization of the kvbeta1 and kvbeta2 beta-subunits with kv1 alpha-subunits in mammalian brain k+ channel complexes. *J Neurosci*, 17(21):8246–8258, Nov 1997. 50

[138] D. A. Hoffman, J. C. Magee, C. M. Colbert, and D. Johnston. K+ channel regulation of signal propagation in dendrites of hippocampal pyramidal neurons. *Nature*, 387(6636):869–875, Jun 1997. doi: 10.1038/43119. URL http://dx.doi.org/10.1038/43119. 50

[139] G. J. Kress and S. Mennerick. Action potential initiation and propagation: upstream influences on neurotransmission. *Neuroscience*, 158 (1):211–222, Jan 2009. doi: 10.1016/j.neuroscience.2008.03.021. URL http://dx.doi.org/10.1016/j.neuroscience.2008.03.021. 50, 51, 85

[140] Dominique Debanne. Information processing in the axon. *Nat Rev Neurosci*, 5(4):304–316, April 2004. ISSN 1471-003X. URL http://dx.doi.org/10.1038/nrn1397. 50

[141] S. A. Baccus. Synaptic facilitation by reflected action potentials: enhancement of transmission when nerve impulses reverse direction at axon branch points. *Proc Natl Acad Sci U S A*, 95(14):8345–8350, Jul 1998. 50

[142] Geraldine J Kress, Margaret J Dowling, Lawrence N Eisenman, and Steven Mennerick. Axonal sodium channel distribution shapes the depolarized action potential threshold of dentate granule neurons. *Hippocampus*, 20(4):558–571, Apr 2010. doi: 10.1002/hipo.20667. URL http://dx.doi.org/10.1002/hipo.20667. 50, 51

[143] D. Debanne, N. C. Guérineau, B. H. Gähwiler, and S. M. Thompson. Action-potential propagation gated by an axonal i(a)-like k+ conductance in hippocampus. *Nature*, 389(6648):286–289, Sep 1997. doi: 10.1038/38502. URL http://dx.doi.org/10.1038/38502.

[144] D. Debanne, I. L. Kopysova, H. Bras, and N. Ferrand. Gating of action potential propagation by an axonal a-like potassium conductance in the hippocampus: a new type of non-synaptic plasticity. *J Physiol Paris*, 93(4):285–296, 1999. 50

[145] J. R. Geiger and P. Jonas. Dynamic control of presynaptic ca(2+) inflow by fast-inactivating k(+) channels in hippocampal mossy fiber boutons. *Neuron*, 28(3): 927–939, Dec 2000. 50

[146] Henrik Alle and Jörg R P Geiger. Combined analog and action potential coding in hippocampal mossy fibers. *Science*, 311(5765):1290–1293, Mar 2006. doi: 10.1126/science.1119055. URL http://dx.doi.org/10.1126/science.1119055. 50

[147] Yousheng Shu, Andrea Hasenstaub, Alvaro Duque, Yuguo Yu, and David A McCormick. Modulation of intracortical synaptic potentials by presynaptic somatic membrane potential. *Nature*, 441(7094):761–765, Jun 2006. doi: 10.1038/nature04720. URL http://dx.doi.org/10.1038/nature04720. 50

[148] Maarten H P Kole, Johannes J Letzkus, and Greg J Stuart. Axon initial segment kv1 channels control axonal action potential waveform and synaptic efficacy. *Neuron*, 55(4):633–647, Aug 2007. doi: 10.1016/j.neuron.2007.07.031. URL http://dx.doi.org/10.1016/j.neuron.2007.07.031. 51, 85

[149] M. Maletic-Savatic, N. J. Lenn, and J. S. Trimmer. Differential spatiotemporal expression of k+ channel polypeptides in rat hippocampal neurons developing in situ and in vitro. *J Neurosci*, 15(5 Pt 2):3840–3851, May 1995. 51, 85

[150] I. Vabnick, J. S. Trimmer, T. L. Schwarz, S. R. Levinson, D. Risal, and P. Shrager. Dynamic potassium channel distributions during axonal development prevent aberrant firing patterns. *J Neurosci*, 19(2):747–758, Jan 1999. 51

[151] A. Korngreen and B. Sakmann. Voltage-gated k+ channels in layer 5 neocortical pyramidal neurones from young rats: subtypes and gradients. *J Physiol*, 525 Pt 3:621–639, Jun 2000. 51, 54, 55, 85

[152] G. Grosse, A. Draguhn, L. Höhne, R. Tapp, R. W. Veh, and G. Ahnert-Hilger. Expression of kv1 potassium channels in mouse hippocampal primary cultures: development and activity-dependent regulation. *J Neurosci*, 20(5):1869–1882, Mar 2000.

[153] Harald Prüss, Gisela Grosse, Irene Brunk, Rüdiger W Veh, and Gudrun Ahnert-Hilger. Age-dependent axonal expression of potassium channel proteins during development in mouse hippocampus. *Histochem Cell Biol*, 133(3):301–312, Mar 2010. doi: 10.1007/s00418-009-0668-z. URL http://dx.doi.org/10.1007/s00418-009-0668-z. 51, 85

[154] M. Frotscher, A. Drakew, and B. Heimrich. Role of afferent innervation and neuronal activity in dendritic development and spine maturation of fascia dentata granule cells. *Cereb Cortex*, 10(10):946–951, Oct 2000. 51

[155] Helene Vacher, Durga P Mohapatra, and James S Trimmer. Localization and targeting of voltage-dependent ion channels in mammalian central neurons. *Physiol Rev*, 88(4):1407–1447, Oct 2008. doi: 10.1152/physrev.00002.2008. URL http://dx.doi.org/10.1152/physrev.00002.2008. 51, 85

[156] Josef Bischofberger, Dominique Engel, Liyi Li, Jörg R P Geiger, and Peter Jonas. Patch-clamp recording from mossy fiber terminals in hippocampal slices. *Nat Protoc*, 1(4):2075–2081, 2006. doi: 10.1038/nprot.2006.312. URL http://dx.doi.org/10.1038/nprot.2006.312.

[157] Costa M Colbert and Enhui Pan. Ion channel properties underlying axonal action potential initiation in pyramidal neurons. *Nat Neurosci*, 5(6):533–538, Jun 2002. doi: 10.1038/nn857. URL http://dx.doi.org/10.1038/nn857. 51

[158] Juan Martinez, Carlos Pedreira, Matias J Ison, and Rodrigo Quian Quiroga. Realistic simulation of extracellular recordings. *J Neurosci Methods*, 184 (2):285–293, Nov 2009. doi: 10.1016/j.jneumeth.2009.08.017. URL http://dx.doi.org/10.1016/j.jneumeth.2009.08.017. 52

[159] Z. F. Mainen, J. Joerges, J. R. Huguenard, and T. J. Sejnowski. A model of spike

initiation in neocortical pyramidal neurons. *Neuron*, 15(6):1427–1439, Dec 1995. 54, 55, 94

[160] Kamran Diba, Henry A Lester, and Christof Koch. Intrinsic noise in cultured hippocampal neurons: experiment and modeling. *J Neurosci*, 24 (43):9723–9733, Oct 2004. doi: 10.1523/JNEUROSCI.1721-04.2004. URL http://dx.doi.org/10.1523/JNEUROSCI.1721-04.2004. 54, 55

[161] G. E. Kirsch and J. A. Drewe. Gating-dependent mechanism of 4-aminopyridine block in two related potassium channels. *J Gen Physiol*, 102(5):797–816, Nov 1993. 55, 74

[162] Cheng-Chang Lien, Marco Martina, Jobst H Schultz, Heimo Ehmke, and Peter Jonas. Gating, modulation and subunit composition of voltage-gated k(+) channels in dendritic inhibitory interneurones of rat hippocampus. *J Physiol*, 538(Pt 2):405–419, Jan 2002. 74

[163] Michel Royeck, Marie-Therese Horstmann, Stefan Remy, Margit Reitze, Yoel Yaari, and Heinz Beck. Role of axonal nav1.6 sodium channels in action potential initiation of ca1 pyramidal neurons. *J Neurophysiol*, 100(4):2361–2380, Oct 2008. doi: 10.1152/jn.90332.2008. URL http://dx.doi.org/10.1152/jn.90332.2008. 94, 95, 96

[164] Shimon Marom and Danny Eytan. Learning in ex-vivo developing networks of cortical neurons. *Prog Brain Res*, 147:189–199, 2005. doi: 10.1016/S0079-6123(04)47014-9. URL http://dx.doi.org/10.1016/S0079-6123(04)47014-9. 109

[165] Bruce C Wheeler and Gregory J Brewer. Designing neural networks in culture: Experiments are described for controlled growth, of nerve cells taken from rats, in predesigned geometrical patterns on laboratory culture dishes. *Proc IEEE Inst Electr Electron Eng*, 98(3):398–406, Mar 2010. doi: 10.1109/JPROC.2009.2039029. URL http://dx.doi.org/10.1109/JPROC.2009.2039029. 110

[166] Jichuan Zhang, Ya Yang, Hongbin Li, Jun Cao, and Lin Xu. Amplitude/frequency of spontaneous mepsc correlates to the degree of long-term depression in the ca1 region of the hippocampal slice. *Brain Res*, 1050(1-2):110–117, Jul 2005. doi: 10.1016/j.brainres.2005.05.032. URL http://dx.doi.org/10.1016/j.brainres.2005.05.032. 111

[167] Emanuele Ostuni, Ravi Kane, Christopher S. Chen, Donald E. Ingber, and George M. Whitesides. Patterning mammalian cells using elastomeric membranes. *Langmuir*, 16(20):7811–7819, 2000. doi: 10.1021/la000382m. URL http://pubs.acs.org/doi/abs/10.1021/la000382m. 111

[168] Jens Huft, Daniel J. Da Costa, David Walker, and Carl L. Hansen. Three-dimensional large-scale microfluidic integration by laser ablation of interlayer connections. *Lab Chip*, 10(18):2358–2365, 2010. ISSN 1473-0197. URL http://dx.doi.org/10.1039/C004051G. 111

[169] J. Garra, T. Long, J. Currie, T. Schneider, R. White, and M. Paranjape. Dry etching of polydimethylsiloxane for microfluidic systems. volume 20, pages 975–982. AVS, 2002. doi: 10.1116/1.1460896. URL http://link.aip.org/link/?JVA/20/975/1. 111

[170] Kathleen W Meacham, Richard J Giuly, Liang Guo, Shawn Hochman, and Stephen P DeWeerth. A lithographically-patterned, elastic multi-electrode array for surface stimulation of the spinal cord. *Biomed Microdevices*, 10(2):259–269, Apr 2008. doi: 10.1007/s10544-007-9132-9. URL http://dx.doi.org/10.1007/s10544-007-9132-9. 111, 121

[171] N Vourdas E Gogolides M E Vlachopoulou, A Tserepi and K Misiakos. Patterning of thick polymeric substrates for the fabrication of microfluidic devices. *Journal of Physics: Conference Series*, 10(1):293–, 2005. ISSN 1742-6596. 111

[172] Jessamine Ng Lee, Cheolmin Park, and George M Whitesides. Solvent compatibility of poly(dimethylsiloxane)-based microfluidic devices. *Anal Chem*, 75(23):6544–6554, Dec 2003. doi: 10.1021/ac0346712. URL http://dx.doi.org/10.1021/ac0346712. 121

[173] Larry J Millet, Matthew E Stewart, Jonathan V Sweedler, Ralph G Nuzzo, and Martha U Gillette. Microfluidic devices for culturing primary mammalian neurons at low densities. *Lab Chip*, 7(8):987–994, Aug 2007. doi: 10.1039/b705266a. URL http://dx.doi.org/10.1039/b705266a. 122, 124